Early Neoproterozoic oxygenation dynamics along the northern margin of the West African Craton, Anti-Atlas Mountains, Morocco

Ernest Chi Fru[a*], Olabode Bankole[b], Ibtissam Chraiki[c], Nassrddine Youbi[c], Marc-Alban Millet[a], Olivier Rouxel[d], Abderrazzak El Albani[b], El Hafid Bouougri[c]

[a]School of Earth and Ocean Sciences, Centre for Geobiology and Geochemistry, Cardiff University, Cardiff CF10 3AT, Wales, UK
[b]University of Poitiers, CNRS IC2MP UMR 7285, Poitiers, France.
[c]DLGR, Department of Geology, Faculty of Sciences-Semlalia, Cadi Ayyad University, Marrakesh, Morocco.
[d]Unité de Géosciences Marines, IFREMER, Z.I. Pointe du diable, BP 70, 29280 Plouzané, France.

*ChiFruE@Cardiff.ac.uk

ABSTRACT

Emerging evidence suggests widespread ferruginous marine conditions promoted global seawater phosphate depletion and the maintenance of a low oxygen world at the start of the Neoproterozoic Era. However, the large-scale deposition of marine sedimentary Fe formations, as observed in the Paleoproterozoic, is rare in the early Neoproterozoic Era. We show that at the start of the Neoproterozoic, tidal flat and shallow marine environments along the northern passive margin of the West African Craton (WAC) were fully oxygenated and low in reactive Fe content, until an abrupt and prolong episode of deep-sea hydrothermal activity overwhelmed the WAC margin with strongly reducing Fe-rich hydrothermal fluids. This unique incident is recorded in meter-thick and kilometer-wide shallow marine siliciclastic platform rocks estimated to be ~883 Ma old and containing average bulk Fe content >22 wt.% in the Wanimzi Formation in the Moroccan Anti-Atlas Mountains. The abrupt and conformable contact of the Fe-rich succession with the Fe-poor lower and upper transition boundaries, together with geochemical data, suggest rapid initiation and termination of seawater fertilization by the hydrothermal fluids that formed the unmetamorphosed hematite-rich ironstones. Rare Earth Element (REE) and Fe-based redox reconstruction point to an aftermath coincident with a return to shallow siliciclastic marine habitats characterized by a low reactive Fe content and negligible hydrothermal intrusion, where aerobic microbial communities flourished in well-oxygenated waters. We propose that the early Neoproterozoic tectonic initiation of the breakup of the supercontinent Rodinia supplied large volumes of deep sea hydrothermal Fe, trace metals, and toxic metalloids like arsenic to shallow marine habitats along the WAC, resulting in rapid seawater deoxygenation.

Keywords: Siliciclastic iron formation; Tonian period; Ironstones; Hydrothermal activity; Rodinia supercontinent.

1. Introduction

It is widely accepted that Precambrian seawater Fe concentrations exerted a major control on early ocean chemistry, oxygenation of the atmosphere, climate, and the evolution of global biogeochemical cycles (e.g., Frei et al., 2008; Planavsky et al., 2010; Heimann et al., 2010: Halverson et al., 2011; Lyons et al., 2014; Brock et al., 2017; Hoffman et al., 2017; Reinhard et al., 2017; Song et al., 2017; Guilbaud et al., 2020; Heard and Dauphas, 2020). For instance, Fe mineral precipitation modulates the concentration of dissolved species in seawater, including macro- and micro-nutrient content (e.g., Dymek and Klein, 1988; Konhauser et al., 2002; Fischer and Knoll, 2009; Zegeye et al., 2012; Chi Fru et al., 2012, 2013, 2015a-b, 2016a-b; Large et al., 2015: Haugaard et al., 2016; Hoffman et al., 2017; Konhauser et al., 2017; Hemmingsson et al., 2018; Keyser et al., 2018; Mukherjee et al., 2019; Robbins et al., 2019; Heard and Dauphas, 2020).

As a consequence, throughout the Archean and for most of the Paleoproterozoic eon, considerable quantities of ferrous Fe oxidized out of seawater to form sizable Algoma type Fe formations containing >15 wt.% Fe in deep sea Archean volcanic centers and Superior type banded iron formations (BIF) on passive Paleoproterozoic sea margins (see Bekker et al., 2010 for a review). A systematic reduction in the deposition of Fe formations has been linked to the permanent appearance of free molecular oxygen in the atmosphere during the so called Great Oxidation Event (GOE) (Bekker et al., 2010; Lyons et al., 2014). This is thought to be the result of enhanced biotic and abiotic oxidation of soluble ferrous Fe to insoluble ferric Fe minerals using molecular oxygen as an efficient electron acceptor (Emerson et al., 2010; Chi Fru et al., 2012), accelerated precipitation of pyrite because of the intensification of microbial sulfate reduction as a result of GOE-induced rise in seawater sulfate concentrations and progressive weakening of hydrothermal activity through Earth history (e.g., Canfield, 1998; Bekker et al., 2010; Poulton and Canfield, 2011; Lyons et al., 2014).

Following the GOE, the oceanic redox structure differentiated into oxygen-rich shallow surface waters, mid-depth continental margin sulfide-rich (euxinic) waters, and deep ferruginous waters (e.g., Canfield, 1998; Rouxel et al., 2005; Poulton et al., 2011; Reinhard et al., 2013; Lyons et al., 2014; Dauphas et al.,

2016; Mukherjee et al., 2019). Pyrite precipitated in the euxinic settings, while the upwelling and the mixing of the deep ocean ferruginous waters with the oxygenated chemocline and surface waters, shuttled silica and ferric Fe to the sea floor (Canfield, 1998; Fischer and Knoll, 2009; Poulton and Canfield, 2011; Reinhard et al., 2013).

Because of the high affinity of both pyrite and ferric Fe for trace elements, these important Fe minerals controlled the mobility and availability of trace elements in seawater through co-precipitation and adsorption reactions (e.g., Reinhard et al., 2013; Large et al., 2015; Mukhkerjee et al., 2019; Robbins et al., 2019). For example, the enrichment of Mo and As in euxinic marine sediments correlate with pyrite accumulation (Reinhard et al., 2013; Chi Fru et al., 2019) while rapid trace element removal from seawater by ferric Fe is observed in oxygenated environments where biological and abiological oxidation of ferrous Fe with oxygen occurs (Konhauser et al., 2002; Chi Fru et al., 2012; Emerson et al., 2010) and in anoxic settings where phototrophic oxidation of ferrous Fe is prevalent (Thompson et al., 2019).

The ferric Fe particles can be reduced in the deep anoxic ocean and sediments by the dissimilatory Fe-reducing bacteria (DIR) using organic carbon and nitrate (Weber et al., 2006) and/or by sulfide (Poulton and Canfield, 2011) to recycle ferrous Fe and bound trace elements and nutrients back to seawater (e.g., Guilbaud et al., 2020). Consequently, Fe carbonates in ancient Fe formations are thought to record the respiratory activities of the DIR (e.g., Severmann et al., 2008; Heimann et al., 2010; Craddock and Dauphas, 2011). Because of the strong coupling between the oxidation state of Fe and seawater redox, the speciation of Fe mineral phases in primary marine chemical sediments has gained widespread application in the reconstruction of past seawater redox state from sedimentary rocks (Poulton and Canfield, 2005; Poulton et al., 2011; Sperling et al., 2015; Raiswell et al., 2018).

This study describes an early Neoproterozoic siliciclastic Fe formation deposited as part of a shallow marine environment along the northern margin of the West African Craton (WAC) in the Anti-Atlas belt of Morocco. We unravel how Fe was sourced from a deep-marine oxygen-starved, hydrothermally active ocean and mixed with oxygenated coastal shoreline waters to form the siliciclastic Wanimzi ironstones. We propose that this incident is linked to

tectonic events that initiated the breakup of the supercontinent Rodinia and that this event had severe consequences for life and the oxygenation of affected shallow seawater masses along the WAC coast.

2. Geological setting

The Proterozoic basement of the Anti-Atlas constitutes the northern margin of the WAC. It is overprinted by Pan-African-Cadomian events and bounded by two tectonic fault zones, represented by the Anti-Atlas major Fault (AAMF) and the High-Atlas South Fault (e.g. Leblanc & Lancelot, 1980; Saquaque et al., 1989; Bouougri, 2003; Ennih & Liegeois, 2008). The AAMF (e.g. Choubert, 1947; Leblanc and Lancelot, 1980; Saquaque et al., 1989) is a tectonic boundary separating the cratonic margin to the south from the ~770-700 Ma island arc-related terrane to the north that was accreted onto the margin during Pan-African collisional events ~663-640 Ma (e.g. Leblanc et Lancelot, 1980; Saquaque et al., 1989; Bouougri, 2003; El Hadi et al., 2010; Thomas et al, 2004; Inglis et al., 2005; Triantafyllou et al., 2016; Fig. 1a).

The post-Eburnean craton margin strata of the Anti-Atlas, comprising of a volcano-sedimentary succession up to 2 km thick spanning the Upper Paleoproterozoic to Early Neoproterozoic time, crops out along the AAMF (Figs 1b). Based on radiometric data, the successions unconformably overlying the Eburnean basement (~2000-1800 Ma) is subdivided according to new radiometric data into three main tectono-sedimentary sequences spanning the Columbia and Rodinia supercontinent cycles (Letsch, 2018; Bouougri et al., 2020). The complete section is well exposed in the central part of the Anti-Atlas along the AAMF, with a tripartite subdivision into a Lower sedimentary ensemble, a Middle volcanic unit and an Upper sedimentary sequence (Bouougri and Saquaque, 2004). In previous works, and considering mainly the Pan-African tectonic features and the lack of any evidence for a Mesoproterozoic Greenvillian tectono-thermal event in the Anti-Atlas and in the WAC, the whole succession was assigned to the Neoproterozoic and to the Pan-African rifted-margin of the Anti-Atlas (Leblanc et Lancelot, 1980; Saquaque et al., 1989; Leblanc and Moussine-Pouchkine, 1994), formally named the Tizi n'Taghatine Group in its stratotype area (Bouougri and Saquaque, 2004). However, revised stratigraphic framework as well as new

radiometric ages obtained from interbedded volcanic occurrences, mafic sills cross-cutting the lowermost part of the succession, and U-Pb ages from detrital zircons, provide evidence for two tectono-stratigraphic cycles of Upper Paleoproterozoic to possibly Mesoproterozoic pre-Pan-African and the Neoproterozoic Pan-African cycle (Letsch, 2018; Bouougri et al., 2020). The first cycle extends from the bottom to the Tasserda, Taghdout and Oumoula Formations. This is succeeded by the Neoproterozoic, subdivided into Tonian strata (~883 Ma) and the ~700 Ma Cryogenian Bleïda Formation, interpreted as rift-related and pre-collisional foreland basin successions, respectively (Bouougri et al., 2020).

The 883 Ma age is obtained from pyroclastic material lying directly above the Imi n-Tizi Formation (Bouougri et al, 2020; Fig. 2a). Gradual emergence of volcanic activity and transition into the deposition of the mainly volcanic rocks in the Tachdamt Formation from the underlying Wanimzi Formation is indicated by the placement of interbedded pyroclastic flow beds in the underlying platform deposits. This kind of transition as well as evidence of feeder dykes cutting through the platform deposits, collectively suggest a Tonian age close to ~883 Ma. Moreover, by considering the maximum 500 m thickness of the platform deposits, low sedimentation rates of 0.06 cm $year^{-1}$, the lack of evidence for a time gap, and a high rate of compaction, deposition of the entire succession could not have exceed a duration of ~5 million years (Bouougri et al., 2020). The platform deposits, including the Wanimzi Formation, are part of the start of a global Neoproterozoic cycle that triggered the breakup of the Rodinia supercontinent ~900 Ma (Bouougri et al., 2020).

In the studied area along the southern margin of the Siroua Inlier (Fig. 1b), the Pan-African rift-related succession of Tonian age is well exposed in the Agoummy section (Fig. 1b). The pre-rift sedimentary strata (Fig. 2a) in ascending order, include the Ifarkhs n´Tirsal, Wanimzi, Tamgarda, Agoummy and Imi n-Tizi Formations (Bouougri and Saquaque, 2004). This mixed siliciclastic-carbonate succession of shallow marine origin, is overlain by the syn-rift volcanic Tachdamt Formation. A new minimum age of ~883 Ma has been recently suggested for the pre-rift shallow marine mixed siliciclastic-carbonate deposits (Bouougri et al., 2020). Transition from the above shallow platform marine siliciclastic deposits to the overlying volcanic Tachdamt

Formation shows no evidence of an erosional unconformity or time gap. Instead, a sharp contact characterized by remnants of pyroclastic occurrences atop of the Imi n'Tizi Formation, indicate stratigraphic continuity (Bouougri et al., 2020). The age of the platform deposit is thus considered very close to ~883 Ma and not older than ~900 Ma even when low sedimentation rates are considered for the platform wedge estimated to be ~500 m thick in the studied section. These shallow near-continental margin sedimentary rocks are thought to record a stable craton margin, which underwent major rifting and magmatic events that led to the breakup of Rodinia (Bouougri et al., 2020).

The lithology of the basal Paleoproterozoic Taghdout Formation in the studied section is dominated by carbonates and mixed siliciclastic-carbonate rocks, while the early Neoproterozoic Wanimzi and Imi n'Tizi formations present fine-grained siliciclastic and heterolithic rhythmic beds, rich in sedimentary structures interpreted as reflecting a shallow shelf setting and the activities of ancient microbial mats (*e.g.*, Bouougri and Saquaque, 2004; Bouougri and Porada, 2002). The heterolithic beds contain biolaminitic thin multilayered packages that formed on sand and as cm-thick planar laminated layers frequently disturbed by shrinkage cracks. A variety of mat-related structures previously identified in these heterolithic layers, in both the Wanimzi and Imi n´Tizi Formations, tend to be associated with reticulate patterns and microbial shrinkage cracks (Bouougri and Porada, 2002).

The studied Fe oxide-bearing Wanimzi Formation is a ~120 m thick siliciclastic unit dominated by heterolithic deposits showing an overall coarsening and shallowing upward trend (Fig. 2). Sedimentary features indicate a depositional setting in a storm and wave dominated shallow marine ramp (Bouougri and Saquaque, 2004). According to sand-mud ratio and facies features, three parts can be distinguished within this formation. These consist of (i) a lower mudstone and fine grained siltstone deposited below storm wave base (SWB), (ii) a middle heterolithic deposit including beds with hummocky cross stratification (HCS) indicating deposition above SWB in an outer offshore transition zone, and (iii) an Upper sand dominated sequence with amalgamated sandstone beds containing HCS and swaley cross-stratification (SCS), indicating deposition in the inner part of the offshore transition to a lower

shoreface zone. The middle part contrasts clearly with other deposits and shows a dense red color related to Fe enrichment.

3. Methods

3.1. Sampling and sample preparation

In the Agoummy area (Fig. 2b), fresh unweathered samples were collected at two key stratigraphic units from the Wanimzi Formation, with focus on the undescribed Wanimzi ironstones (Fig. 3) and reference microbial laminated samples from the overlying Imi n'Tizi Formations (Fig. 4). The Wanimzi Formation was sampled at 5-10 cm intervals at 30°30'0.58"N, 7°41'51.47"W and 30°29'57.84"N, 7°41'48.08"W (Fig. 3a-b&d). These well-exposed outcrops (Fig. 3a-d) can be seen using satellite imagery to be laterally exposed for at least ~4 km.

Three reference carbonate samples were also collected from outcrops of the underlying older Paleoproterozoic (>1640 Ma) Eburnean basement at the Taghdout Formation and four from the well preserved stromatolite-rich siliciclastic rocks of the uppermost Imi n'Tizi Formation (Fig. 4a) described in Bouougri et al. (2002, 2007). The Taghdout carbonates and the Imi n'Tizi silicate rocks were sampled to provide Fe-poor references for comparison with the Fe-rich lithologies and to enable the interpretation of the transitional events that led to the onset and termination of the deposition of the Wanimzi ironstones. Representative stromatolitic units sampled from the Imi n'Tizi Formation consist of twisted biolaminations (S1), horizontal beds with no laminations (S2), consistent millimeter-thick bands (S3) and flat visible horizontal biolaminations (S4). Samples were collected for redox reconstruction, thin-section petrography, mineralogy, trace element (TE) and rare earth element (REE) analyses, C and Fe isotope measurements.

3.2. Petrography and mineralogy

Before analysis, samples were shaved with a saw and exposed surfaces in contact with the atmosphere discarded. Polished thin-sections were prepared using standard rock-polishing laboratory procedures in the School of Earth and Ocean Sciences, Cardiff University. Portions of identical shaved thin-sectioned rock pieces were pulverized to a fine powder for geochemical analysis using a

jaw crusher and by disc milling. Polished thin-sections for representative samples were examined for mineralogy and textural relationships under reflected and transmitted light microscopy using a Nikon ECLIPSE E600 POL microscope equipped with a Nikon Digital Sight DS-U1 camera at the University of Poitiers, France. Whole rock X-ray diffraction (XRD) mineral analyses were performed on powdered samples with a Bruker D8 ADVANCE diffractometer using CuKα radiation operating at 40 Kv and 40 mA and step size of 0.025/s between 2-65 °2θ angular ranges.

3.3. Trace and Rare Earth Element analysis

Bureau Veritas© (Vancouver, Canada) procedure code LF100-EXT was used to measure the concentration of 45 TEs and REEs in 0.2 g powdered samples. The samples were digested by lithium borate ($LiBO_2/Li_2B_4O_7$) fusion and solutions analyzed by Inductively Coupled-Mass Spectrometry (ICP-MS). Lithium borate fusion is an aggressive chemical digestion process that effectively dissolves most refractory and resistant mineral phases, ensuring complete dissolution of powdered samples. Total Fe was measured by UV-Vis spectrometry using Stokey's ferrozine test as part of the Fe speciation protocol described in Poulton and Canfield (2004) and in section 3.4. Post Archean Australian Shale (PAAS) was used for REE+Y normalization (McLennan, 1989) and REE+Y anomalies are calculated as described previously (Bau and Dulski et al., 1996; Planavsky et al., 2010).

3.4. Fe-based redox reconstruction

Redox reconstruction was obtained by application of the widely used Fe-based methodology for the reconstruction of bottom water redox conditions in modern and ancient siliciclastic and carbonate depositional environments habitats (Poulton and Canfield, 2005; Clarkson et al., 2014; Raiswell et al., 2018). This method allows the allocation of the Fe mineral phases into seven operational pools, divided into highly reactive ferric Fe and pyrite Fe phases (Fe_{HR}), poorly reactive sheet silicate Fe and Fe in unreactive silicate (Poulton and Canfield, 2005). Samples were screened to contain >0.5 wt% Fe – a minimum threshold recommended to correct for variations in sedimentary Fe concentrations and

dilution by detrital materials (Poulton and Canfield, 2005; Clarkson et al., 2014; Raiswell et al., 2018).

3.5. Carbon and oxygen isotopes

Organic carbon (C_{org}), carbonate carbon ($C_{carbonate}$) and carbonate O isotopes ($O_{carbonate}$) were co-measured on a Thermo Delta V Advantage mass spectrometer. The instrument is connected to a Thermo gasbench II for headspace sampling $C_{carbontes}$), while a Thermo Flash EA with Conflo III allows for the combustion of organic samples. The $\delta^{13}C$ and $\delta^{18}O$ are reported in the delta notation using the Vienna-Pee Dee Belemnite (VPDB) standard. The C_{org} and inorganic carbon content was estimated from a regression equation for signal intensity against the amount that was established for standard materials with known composition. Powdered samples were weighed into septum vials flushed with helium, acidified with 99 % orthoposphoric acid, and left to react for 24 hours at 60 °C to ensure complete reaction of dolomite. The long-term precision of an in-house Carrara marble standard has been estimated to 0.05 ‰ for both $\delta^{18}O$ and $\delta^{13}C$ (1sd). To eliminate inorganic carbon, prior to measuring C_{org} concentrations and $\delta^{13}C_{org}$ isotopic distribution, samples were acidified in 10 % HCl and reaction left for two days. Residual acids was removed by washing the treated samples three times with ultrapure double distilled water. Sixty to eighty mg of samples were analysed for C_{org}. The total C_{org} analysed was as low as 10 µg because of low C_{org} content. Three standards were used to calibrate the accuracy of these small sample concentrations: IAEA-CH6 [$\delta^{13}C$=-10.449 ‰], IAEA-6oo [$\delta^{13}C$=-27.771 ‰], and an in-house caffeine [$\delta^{13}C$=-33.30 ‰]) and were dissolved in de-ionised water to improve homogeneity and to allow accurate dosing of small aliquots using a micropipette. Results for IAEA-CH6 and the in-house caffeine were used to estimate a correction function for sample size and size-dependent 2-point normalisation, which was applied to IAEA-600 as the independent standard. The resultant precision is dependent on sample size. The long-term precision for $\delta^{13}C$ was 0.09 ‰ (1sd) for routine samples containing ≥100 µg C. However, the standard deviation increases with decreasing sample size, to 0.38 ‰ for aliquots with 10 - 30 µg C as measured for the present study (IAEA-600, N=15).

338 *3.6. Fe isotopes*

339 Samples were dissolved by standard acid digestion using concentrated HF,
340 HNO_3, and hotplates in acid washed Teflon beakers, and purified through
341 polypropylene pipette tips chromatographic columns containing a 500 µl AG1-
342 X4 anion exchange resin (Millet et al., 2012). Fe isotopes were measured at
343 IFREMER, France, on a Thermo Scientific Neptune MC-ICP-MS set on medium
344 or high-resolution mode as described in Rouxel et al. (2018). Analysis included
345 sample-standard bracketing and internal normalization using Ni with a known
346 isotope ratio and an internal precision of 0.04-0.09‰ (2sd) for 100 ng of
347 recovered Fe (Rouxel et al., 2018). Data are reported as $\delta^{56}Fe$ and $\delta^{57}Fe$ ratios
348 in parts per thousand deviations from the IRMM-014 standard. More than 50
349 replicates of the Hawaiian basalt internal standards BHVO-1 and BHVO-2 using
350 this method yielded average $\delta^{56}Fe$ values of 0.09 ± 0.07‰ (Rouxel, 2018).
351

352 **4. Results**

353 *4.1. Field observations and sedimentary features*

354 The Fe-rich layers in the Wanimzi Formation often occur as oxidized red to
355 purple cm-thick beds alternating with heterolithes and thin storm beds with HCS
356 (Fig. 3a-c). In the lower part of Wanimzi Formation (Fig. 2b, 3d), several isolated
357 decimeter-thick storm beds of Fe-rich sandstones were observed, some of
358 which preserve artisanal digging trenches running parallel to the mineralized
359 layers. The heterolithic beds are composed of silt, sand, and microbial
360 biolaminated layers similar to the overlying Fe-poor Imi n´Tizi Formation (Fig.
361 4), indicating deposition of both successions above a storm wave base, in a
362 shallow marine setting. Well-developed and previously described siliciclastic
363 stromatolites, marked by prominent flat to large domal shaped morphologies
364 (Bouougri and Porada, 2011), appear in the Imi n´Tizi fine-grained siliciclastic
365 Formation (Fig 4g-h).

366 Several mat-related structures dominated by Kinneyia-type wrinkled
367 structures, ripples, spindle-shaped and sinusoidal cracks, and sandstone chips
368 were recognized within the heterolithic facies in the Wanimzi and Imi n´Tizi
369 Formations (Fig. 4). The Kinneyia-type wrinkled structures in both formations
370 occur on the upper surfaces of sandstone beds, and are characterized by mm-
371 thick structures twisted into flat-top crests separated by round bottom troughs

372 and pits that are comparable in size (Fig. 4c). Ripple marks on the top of several
373 sandstone beds (Fig. 4a-b) are colonized and stabilized by thin or thick
374 microbial mat layers (Bouougri and Porada, 2002). Spindle-shaped and
375 sinusoidal cracks (Fig. 4d), equally abundant in the Wanimzi and Imi n´Tizi
376 Formations, were associated with mm-laminated argillite, sandstones and silty
377 sandstones that are sometimes formed on the upper surfaces of sandstone
378 beds free of mud trappings (Fig. 4e). These structures present a great variety
379 in size and shape, including sub-circular, crescent-shaped and sinusoidal
380 cracks observed on the upper bedding surfaces of fine-grained quartzite and
381 siltstone layers. Structures related to microbial mat colonization and upper
382 veneer stabilization of sand bedding surfaces occur as current deformation
383 features and flat microbial sand clasts (Fig. 4e-f). The association of these
384 features with large ripple slabs made up of sandstone confirms the deposition
385 of the Imi n'Tizi Formation in a shallow marine environment. Horizons with
386 sandstone chips and characterized by well-rounded to ellipsoidal flat-shaped
387 features appear abundantly in the basal units of the medium to fine-grained
388 quartzite layers.
389 Beginning with the microbial mat-rich Imi n'Tzi Formation that marks the
390 top of the studied package, the layers are composed of two distinct sediment
391 types, typified by sharp coarse and fine-sediment layers (Fig. 5a-b). The
392 siliciclastic stromatolites consist of mat-growth structures made up
393 predominantly of moderately compacted and well-sorted quartz-dominated
394 silty-sandstone layers alternating thin mud/shale laminae, consisting of micas
395 and dominated by muscovite and illite (Fig. 5a-b; Table 1; Appendix A-B). The
396 quartz coarse grains are detrital, while the fine-grained layers have been
397 suggested to be fossil remains of ancient microbial mat layers according to
398 several mat-related features preserved on bedding surfaces (Bouougri and
399 Porada, 2002). This simple repetitive architecture of coarse siliciclastic layers
400 alternating with thinner fine-grained siliciclastic beds was observed on all
401 sections investigated. Well-sorted, rounded, angular to sub-angular, silt-sand-
402 sized quartz grains cemented in an Fe-rich matrix, are a unique characteristic
403 and distinguishing hallmark of the Wanimzi Formation (Fig. 5c-f).
404
405 *4.2. Mineralogical characterization*

406 Thin section analysis of the Fe-rich lithologies in the Wanimzi Formation (Fig.
407 5) is consistent with the mainly siliciclastic composition of near continental
408 margin Neoproterozoic deposits in the Moroccan Anti-Atlas Mountains.
409 Although hematite and quartz are present in all lithologies, their predominant
410 character is restricted to the Wanimzi ironstones (Appendix C-E & H-J), while
411 quartz predominates the stromatolitic lithologies of the Imi n'Tizi Formation
412 (Appendix A-N). The Taghdout Formation consists primarily of ooid-peloid
413 grainstone cemented in a mainly quartz-carbonate matrix composed of calcite,
414 dolomite, minute hematite concentrations, feldspars, and illite/mica clays (Fig.
415 5g-i; Appendix F,G, L). The ooids are made of microcrystalline calcitic laminae
416 with radially arranged calcite crystals and dark Fe enriched thinner laminae.
417 Relics of oolites were identified showing the dissolution of the original structure
418 and its replacement by drusy calcite crystals, indicating a neomorphism
419 process (Fig. 5g-i; Appendix F,G, L).
420
421 *4.3. Trace element (TE) geochemistry*
422 Out of the 45 elements analyzed, Fe is the most enriched across all lithologies
423 (Fig. 6; Table 2). Co, V, U, As, Sb are pronounced in the ironstones which
424 record varying Cu enrichment and Mo depletion, compared to average
425 concentrations in the siliciclastic stromatolitic and carbonate-rich rocks (Table
426 2; Fig. 6a-d). Cd was below the detection limit of 0.1 ppm in both the siliciclastic
427 stromatolitic and hematite-rich rocks while averaging 0.37 ppm in the
428 underlying carbonate-rich facies. Average As concentrations in the Wanimzi
429 ironstones were 18.2, 8.8, and 19.4 times in excess of those measured in the
430 overlying siliciclastic facies, the underlying siliciclastic carbonates and average
431 upper continental crust values, respectively. These values were much lower for
432 the siliciclastic and carbonate lithologies relative to the upper continental crust
433 by a factor of 1.1 and 2.2, respectively. As and Sb expressed similar curves in
434 all samples (Fig. 6a&d). Fe concentrations of up to 61.7%, averaging 22.4%
435 (n=18) (Table 2) qualify the Wanimzi ironstones as an Fe formation based on
436 the definition of a chemical sedimentary sequence containing >15% Fe (see for
437 example Bekker et al., 2010).
438 The average Fe content in the ironstone lithologies are up to a factor of
439 34, 21, and 64 in excess of the average concentrations in the representative

samples from the reference siliciclastic stromatolite-rich Imi n'Tizi Formation, the Taghdout siliciclastic carbonate facies, and the upper continental crust average reported by McLennan (2001), respectively (Table 2). Moreover, Fe and quartz are often inversely related in the Fe-rich rocks (Fig. 6e), but Fe remained generally below 1.0 wt.% in the stromatolitic and carbonate-rich layers. Zn/Co ratios largely decreased from the carbonates through to the overlying Neoproterozoic siliciclastic stromatolitic succession (Fig. 6f). Mo/W ratios are generally low (Fig. 6g). Th/U ratios are relatively low in the Fe-rich sequences compared to the reference overlying and underlying Fe-poor samples (Fig. 6h).

4.4. Carbon content, and carbon and oxygen isotope distribution

C_{org} concentrations are generally low, ranging from 0.01 to 0.06 wt% across the sequence, with the highest values associated with the Taghdout carbonates (Fig. 6i; Table 3). The average value of C_{org} is 0.02±0.0008 wt%, 0.05±0.012 wt%, and 0.01±0.004 wt% in the ironstones, carbonates, and stromatolitic mats, respectively. The isotopic distribution of $\delta^{13}C_{org}$ range from -33.03‰ to -22.93‰, averaging -29.8±2.22‰, -27.42±0.99‰, and -29.49±1.85‰ in the Fe-rich, the carbonates, and the stromatolitic lithologies, respectively. The lowest and highest single $\delta^{13}C_{org}$ values are recorded in the Fe-rich rocks (Fig. 6j; Table 3), while the rare occurrence of carbonates in the Fe-rich rocks is consistent with XRD data, except for sample AG14 with a carbonate concentration of 0.21 wt% and associated $\delta^{13}C_{carbonate}$ and $\delta^{18}O_{carbonate}$ values of -8.72‰ and -12.79‰, respectively, (Table 3). The carbonate-rich lithologies have high carbonate concentrations between 50 and 75 wt%, with measured $\delta^{13}C_{carbonates}$ and $\delta^{18}O_{carbonate}$ values ranging from -0.77‰ to 0.11‰ (average = -0.28±0.45‰) and -14.5 to -13.28‰ (average = -14.03±0.65‰), respectively (Table 3).

4.5. Rare Earth Elements (REEs)

Post Archean Australian Shale (PAAS) normalized REE patterns are generally similar for the siliciclastic biolaminites and Taghdout carbonate lithologies, but largely different for the Wanimzi ironstones (Fig. 7a-c). The three facies types show pronounced seawater influences consistent with LREE depletion, strong

Ce depletion and sporadic Y enrichment (Table 4; Fig. 7). There is pronounced enrichment of Nd, Sm, Eu, Gd, Tb, and Dy relative to Ho and Tm depletion in some of the ironstone lithologies that distinguishes the ironstone deposits from the underlying and overlying Fe-poor rocks (Fig. 7). REE cross plots, including Zr and Th, show selective enrichment patterns that may be related to provenance (Fig. 8).

PAAS normalized Eu anomalies corrected for anomalously high sedimentary Gd concentrations, $(Eu/Eu^*)_{SN1}$, averaged (±standard deviation from the mean) 1.13±0.09, 1.24±0.08, and 1.04±0.03 for the Taghdout carbonate facies, the ironstones, and the siliciclastic stromatolitic rocks, respectively (Fig. 9a). When corrected for elevated Tb, $(Eu/Eu^*)_{SN2}$ averaged 1.14±0.08, 1.16±0.09, and 1.09±0.08 for the ironstones, the siliciclastic stromatolitic and Taghdout carbonate facies, respectively, with corresponding averaged LREE/HREE ratios of 3.37±0.59, 2.12±1.23, and 3.96±0.90, respectively. The average Y/Ho ratios for the ironstones, the siliciclastic biolaminites, and Taghdout carbonate facies are 27.45±1.14, 28.40±2.80, and 27.50±1.78, respectively (Fig. 9b), which are relatively close to a typical crustal and clastic sediment molar ratio of 28, suggesting a strong siliciclastic detrital influence on the REE composition of the sediments. The average Y/Ho ratios reflect lowered reactivity of Y by the presence of siliciclastic material, which as expected, tends to be lower compared to non-siliciclastic deposits (McLennan, 1989; Bau et al., 1997; Planavsky et al., 2010; Halverson et al., 2011).

La_{SN} anomalies $(La/Yb)_{SN}$ are typically positive with average values of 1.07±0.27, 0.85±0.62, and 0.95±0.26 for the Taghdout carbonates, the Fe-rich deposit and the siliciclastic mats, respectively (Fig. 9c), compared to Precambrian Fe formation values that are typically vary between 0.10 and 0.89 (Planavsky et al., 2010). $(Tb/Yb)_{SN}$ average values are 0.96±0.10, 1.68±0.67, and 0.79±0.09 whereas $(Pr/Yb)_{SN}$ have averages of 0.90±0.20, 0.84±0.51, and 0.91±0.24 for the Taghdout carbonates, the Fe-rich deposit and the siliciclastic mats, respectively (Fig. 9d). The $(Sm/Yb)_{SN}$ ratios averaged 0.98±0.096, 1.18±0.31, and 0.77±0.14 for the Taghdout carbonates, the Fe-rich deposits and the siliciclastic biolaminites, respectively (Fig. 9e), while the $(Eu/Sm)_{SN}$ averages for the Taghdout carbonates, the Wanimzi ironstones and the siliciclastic biolamnites are 0.96±0.096, 1.14±0.31, 1.06±0.06 respectively (Fig.

9f). Gd_{SN} anomalies [$(Gd/Gd^*)_{SN} = Gd_{SN}/(0.33Sm_{SN}+0.67Tb_{SN})$] have average values of 0.92±0.02, 1.13±0.13, and 0.91±0.06 for the Taghdout carbonates, the ironstones and the siliciclastic stromatolites, respectively (Fig. 9g). The strong positive Gd_{SN} anomalies for the Wanimzi Fe-rich deposit is consistent with those found in many Precambrian IFs.

4.6. Redox reconstruction

With the exception of two samples, the three successions (Fig. 9a) display pronounced true cerium anomalies (Ce/Ce*). However, redox reconstruction using Fe-based redox proxy points to mainly ferruginous and anoxic bottom water during the deposition of the ironstones and the carbonate lithologies, with full water column oxygenation limited to the Fe-poor stromatolitic reference rocks (Fig. 10b-c).

4.7. Fe Isotopes

Bulk $\delta^{56}Fe$ distribution in the stromatolitic and the Wanimzi Fe-rich lithologies range from 0.45‰ to 0.61‰ and -0.41‰ to 0.35‰ with means of 0.52‰ and -0.03‰, respectively (Fig. 11a-b; Table 3). With a fractionation factor of 0.55‰ (i.e., $\Delta^{56}Fe = \delta^{56}Fe_{\text{stromatolitic unit}} - \delta^{56}Fe_{\text{Fe-rich units}}$), the data show that the siliciclastic stromatolitic rocks are $\delta^{56}Fe$ enriched compared to the Fe-rich units. At <5 wt.% Fe concentration, $\delta^{56}Fe$ values become increasingly positive, and at >5 wt.% Fe concentration, they switch towards being more negative, with the exception of sample AG08 and AG12 (Fig. 11c).

5.0. Discussion

5.1. Sediment mineralogy and paragenesis

The primarily siliciclastic composition of the three studied successions, differing only in their Fe, quartz, and carbonate contents, suggests formation of these deposits in a stable shallow marine platform environment (e.g. Schofield et al., 2006; Ennih and Liegeois, 2008; Jessell et al., 2016). The heterolithic bedding planes and the abiotic and biotic structures common in both the Wanimzi and the Imi n´Tizi Formations are consistent with their previously described deposition in a shallow marine setting marked by intermittent desiccation

intervals characterized by shrinkage cracks (Bouougri and Porada, 2002). The high siliciclastic content of the studied successions characterized by well-sorted, angular, rounded grains that range in size from fine to coarse clasts, and the presence of extensive ripple marks and desiccation cracks, are typical features of peritidal environments.

The studied ironstone facies lack typical mineral assemblages associated with late stage diagenesis and metamorphism. Secondary mineral phases such as Fe carbonates, often interpreted to be products of reductive transformation of ferric Fe during burial diagenesis and lithification, could not be detected by XRD, consistent with a low Fe carbonate signal obtained by the sequential Fe extraction method. Collectively, this observation suggests that the emergence of more energetic electron donors such as nitrate in post-GOE seawater (e.g., Stüeken et al., 2016) may have subdued DIR bacteria activity relative to the Archean. For instance, Archean IFs record high Fe carbonate concentrations compared to the simpler and mainly hematite-rich mineralogy of Proterozoic and Phanerozoic IFs (Bekker et al. 2010, Chi Fru et al., 2013; Lechte et al., 2018). Negligible post-depositional transformation is further evidenced by the mainly hematite cement considered to reflect primary to early diagenetic sedimentary features in Fe formations (Chi Fru et al., 2013, 15b, 2018a; Sun et al., 2015; Halverson et al., 2011). Mineralogical and microscopic analyses, combined with Fe speciation data, suggest primary and diagenetic pyrite deposition is imperceptible across the succession and no evidence was found to support pyrite oxidation as the source of ferric Fe in the rock. Significant sulfide production is expected to inhibit ferric Fe deposition through rapid chemical reaction with ferrous Fe, combined with abiotic ferric Fe reduction by sulfide (Wensheng and Millero, 1996; Poulton et al., 2004). The floating of silty grains in the Fe-rich cement and the occurrence of hematite, together with indiscernible grain replacement and transformation of the primary hematite (Figs. 5c-d; Appendix C-D), point to minimal compaction diagenesis and to the syngenetic origin of hematite in the Fe-rich Wanimzi ironstones. Combined with trace element and REE analyses and as discussed further below, collectively the data do not support a subterranean or potential groundwater supply of Fe to the basin during the formation of the Wanimzi ironstones.

574 The $\delta^{13}C_{org}$ values, supported by the preservation of stromatolitic mats,
575 suggest all three successions were associated with photosynthetic activity. The
576 similar average $\delta^{13}C_{org}$ values for the Fe-rich and stromatolitic layers differ from
577 the underlying Taghdout carbonates by 2.4‰ and 2.0‰, respectively. We
578 propose that similar carbon cycling processes were involved in the deposition
579 of the early Neoproterozoic Waminzi Fe-rich units as in the siliciclastic
580 stromatolitic rocks. The very negative $\delta^{13}C_{carbonate}$ values of the underlying
581 Taghdout Formation suggest negligible burial of photosynthetic C_{org}, which is
582 demonstrated by the low C_{org} concentrations recorded at this time. It is also
583 possible that the extreme negative $\delta^{13}C_{carbonate}$ values reflect authigenic activity
584 of the methane oxidizing bacteria (Schrag et al., 2013). There is no evidence in
585 our dataset to suggest carbonate weathering as a mechanism that produced
586 the large negative $\delta^{13}C_{carbonate}$ excursion (Shields et al., 2017).
587
588 *5.2. Hydrothermal versus seawater contribution*
589 *5.2.1. Insights from REE Systematics*
590 REEs are reliable source tracers of sedimentary deposits. Being largely
591 immobile in aqueous solution, they tend to behave conservatively during
592 sediment formation (Taylor and McLennan, 1985). For example, La/Sm and
593 Gd/Yb ratios normalized to upper continental crust values are frequently used
594 as sediment source indicators (e.g., Wani and Mondal, 2011). Shale normalized
595 Ce (Ce_{SN}) depletion is assumed to be a seawater and redox proxy, and Eu_{SN}
596 enrichment, a hydrothermal marker as well as a weathering proxy (Bau and
597 Dulski, 1996; Singh and Rajamani, 2001; Shields et al., 2004; Bau and
598 Koschinsky, 2009). The depletion of Ce_{SN} across the studied succession thus
599 provides significant evidence for major seawater involvement in the origin of
600 the studied facies (e.g., Tostevin et al., 2016). This conclusion is corroborated
601 by independent sedimentological evidence that has long alluded to a marginal
602 sea setting for the studied facies (e.g., Hefferan et al., 2000; Bouougri and
603 Saquaque, 2000, 2004; Ennih and Liégeois, 2001; Thomas et al., 2004;
604 Bouougri and Porada, 2002, 2010; Bouougri et al., 2020).
605 The statistically supported positive correlations between Nd (usually of
606 hydrothermal or seawater origin) and Pr and Th (both often depleted in
607 hydrothermal fluids) and Ce (of either hydrothermal or seawater provenance)

608 and Pr (Bau and Dulski, 1996, 1999; Planavsky et al., 2010), suggest a
609 predominantly seawater origin for Ce. The positive correlation between Ce and
610 the non-hydrothermal Pr, combined with the pronounced seawater Ce_{SN} signal,
611 provide robust support for the latter proposition. Similarly, the lack of correlation
612 amongst the three REEs - Nd vs Ga and Nd vs Eu (Fig. 8d. h), which are
613 commonly enriched in hydrothermal fluids (German and Seyfried, 2014), again
614 suggest REE contributions from seawater, probably as adsorbates of the
615 abundant siliciclastic detritus. The latter proposal is consistent with the strong
616 positive correlations of Ce vs. La and Ce vs. Nd (Fig. 8e-f), which hint that both
617 La and Nd may be of a strong seawater origin. Typically, Eu_{SN} enrichment is
618 attributed to hydrothermal activity (e.g., Douville et al., 2002; Tivey, 2007;
619 Planavsky et al., 2010; German et al., 2014). However, the subtle positive
620 enrichment of Eu_{SN} in the samples coupled to the moderate positive correlation
621 between Eu and the non-detrital Zr (Fig. 8l), point to up to 58 % of Eu being
622 associated with the siliciclastic material.
623 Increasing depletion of HREEs relative to LREEs, typically interpreted as
624 evidence for hydrothermal influence, has been reported for Fe formations
625 across Earth history (e.g., Planavsky et al., 2010; Bau, 1996; Ganno et al.,
626 2017). For example, hydrothermal fluids emitted by modern deep-sea vents are
627 generally enriched in LREE (Mitra et al., 1994; Bau and Dulski, 1999; Craddock
628 et al., 2010), whereas enrichment of HREEs relative to LREEs is a common
629 feature of the modern oxygenated seawater (e.g., Bau et al., 1997; Bolhar et
630 al., 2007) but has also been recorded in hydrothermal fluids in a few cases
631 (e.g., Klinkhammer et al., 1994; Douville et al., 1999). Non-siliciclastic
632 Precambrian Fe formations with pronounced HREE enrichments also contain
633 positive $(Eu, La, Y \text{ and } Ga)_{SN}$ anomalies (Bau and Dulski, 1996). We propose
634 that the fluctuating LREE/HREE ratios recorded in the Wanimzi ironstones
635 reflect varying degrees of the mixing of hydrothermal fluids with seawater.
636 Because the entire sample set is characterized by detrital loading, the
637 unique trends in the ironstones cannot be related to an anomaly attributable to
638 detrital contamination relative to the reference underlying and overlying rocks,
639 which are also composed of siliciclastic detritus. We therefore interpret the
640 above observations to reflect long distance transportation and thorough mixing
641 of the Fe-rich fluids with seawater, followed by delivery and deposition on the

642 margin of the WAC (Fig. 13). The data also imply that the seawater chemical
643 conditions on the WAC margin were radically different from those at the source
644 and during transportation, to enable the quantitative precipitation of dissolved
645 Fe from seawater and transformation into ironstone.
646
647 *5.2.2. Insights from trace element systematics*
648 The Wanimzi Fe-rich lithologies are enriched in key redox sensitive elements,
649 such as As, V, Co, Sb, and Fe, that are typically concentrated in submarine
650 hydrothermal fluids by up to eight times relative to modern seawater
651 concentrations (e.g., Douville et al., 2002; Tivey, 2007; German and Seyfried,
652 2014). This would have been more significant in the Precambrian oceans that
653 experienced much higher levels of hydrothermal activity. For example, Fe
654 supplied by submarine hydrothermal fluids is suggested to be a major source
655 of Fe to Precambrian seawater (see for example Bekker et al., 2010), with
656 values in excess of 10^3 ppm reported for fluids from present-day mid-ocean
657 spreading ridges (Tivey et al., 2007).
658 Evidence shows that, despite the observed loss of reduced Fe escaping
659 from modern hydrothermal vents and during plume dispersal through rapid
660 chemical reactions with oxygenated seawater, the loss of Fe is much slower
661 than previously thought (see Gartman and Findlay, 2020, for a review). The
662 stabilization of Fe through binding with organic matter, inorganic nanoparticles,
663 organic and inorganic colloids results in Fe being transported thousands of
664 kilometers across the open modern ocean (Bennett et al., 2008; Toner et al.,
665 2009; Sander and Koschinsky, 20011; Yücel et al., 2011; Resing et al., 2015;
666 Fitzsimmons et al., 2017; Lough et al., 2019). However, the higher mobility of
667 Fe in the predominantly anoxic Precambrian seawater would have allowed for
668 more stable transportation of Fe across oceans and for thorough mixing with
669 seawater. Because shallow oxygenation of the surface ocean was prevalent at
670 this time, contact with oxic marginal seawater would have promoted the
671 precipitation and burial of hydrous ferric oxyhydroxides and their diagenetic
672 products in the affected shallow water sediments. Fe concentrations of up to
673 10^5 ppm are recorded in the continental platform sediments in the Wanimzi
674 Formation (Table 2), being about a factor of two greater than the concentrations

675 in modern submarine hydrothermal systems (Tivey, 2007; German and
676 Seyfried, 2014).
677 The variation in Fe and quartz content in the Fe-rich lithologies point to
678 related changes in the intensity of the delivery of Fe-rich fluids to seawater (see
679 for example Chi Fru et al., 2013; 2018). For instance, Zn/Co ratios with high
680 and low values associated with hydrothermal and detrital influence, respectively
681 (Toth, 1980; Halverson et al., 2011), largely decreased from the carbonates
682 through to the overlying Neoproterozoic siliciclastic stromatolitic succession
683 (Fig. 6f). Mo/W ratios, a measure of sediment formation from sulfide-rich fluids
684 due to the high reactivity of Mo towards sulfide relative to W, are generally low
685 (Fig. 6g), This observation suggests potential precipitation of particle-reactive
686 thiomolybdate with sulfide minerals near the source of the Fe-rich fluids and
687 subsequent precipitation of W enriched in the migrating plume relative to Mo
688 with primary ferric Fe minerals on the oxygenated continental margin (see for
689 example Mohajerin et al., 2016; Bauer et al., 2017; Dellwig et al., 2019).
690 The higher enrichment of W in the Fe-rich facies relative to the upper
691 continental crust, the siliciclastic stromatolitic, and Taghdout carbonate rocks,
692 support a significant supply of W to the basin by hydrothermal activity (Table
693 2). Consistent with the latter observation, the Fe-rich samples are ~2 and 4
694 times more enriched in W than the siliciclastic stromatolite-containing and
695 carbonate facies, respectively (Table 2). Similarly, the strong enrichment of As
696 and Sb in Fe-rich layers relative to the siliciclastic layer, the carbonates and
697 upper continental crust are similar to those for Fe, consistent with a suggested
698 hydrothermal original of these elements (e.g., Breuer and Pichler, 2013; Feely
699 et al., 1991; 1998, Chi Fru et al., 2013; Zeng et al., 2018; Table 2). The latter
700 proposition is supported by a clear lack of similar significant enrichment of As,
701 Sb, and Fe in the siliciclastic and carbonate layers relative to the upper
702 continental crust. (Table 2). Th/U ratios frequently used as a redox proxy
703 whereby U is enriched in deoxygenated sediments relative to Th (Kerrich et al.,
704 2013; Manikyamba, 2018), are relatively low in the Fe-rich sequences
705 compared to the reference overlying and underlying Fe-poor samples (Fig. 6h).
706 The above observations suggest intense and prolonged hydrothermal
707 activity linked to an Fe-rich source that enabled significant Fe enrichment in the
708 fluids that deposited the Wanimzi ironstones on the coast of the WAC. The Fe

concentrations were probably much higher in the pristine hydrothermal fluids emerging from the vents, given that substantial quantities of Fe would have been precipitated with hydrothermal sulfides near the vents as commonly observed at various modern hydrothermal vent fields. Combined, the Fe-rich fluids that formed the Wanimzi ironstones and the sharp absence of ironstones in the underlying and overlying successions suggest sudden initiation and termination of the of supply Fe-rich fluids to the WAC during deposition of the unique Wanimzi ironstones. Intriguingly, this proposition is consistent with the suggested age of the Wanimzi Formation being coincident with the inception of rifting and breakup of the Rodinia supercontinent dated at 920-890 Ma in many Proterozoic cratons (e.g. Evans et al., 2016; Zhou et al., 2018; Baratoux et al., 2019; Chavez et al., 2019) and in the Anti-Atlas at 883 Ma (Bouougri et al., 2020). Such widespread rifting event and supercontinent breakup would have inevitably led to the development of active submarine hydrothermal vent complexes.

In addition to Fe, prominent hydrothermal metals like Co, As, V, Sb, Pb and Cu (Tivey, 2007; Beuer and Pichler, 2013; German and Seyfried, 2014; Rouxel et al., 2018), show variable but stronger enrichments in the Wanimzi ironstones compared to the Fe-poor reference sequences (Fig. 6; Table 2). For instance, the concentration of As in the ironstones is up to 80 times greater than the 3000 times As concentrations discharged by some modern back and Island arc basin shallow submarine hydrothermal fluids compared to unadulterated seawater levels (e.g., Breuer and Pichler, 2013). Importantly, Fe-hematite sedimentary rocks deposited from these pristine high As-containing submarine As-rich hydrothermal fluids are reported to record similar anomalously high As concentrations (e.g., Chi Fru et al., 2013). Even more interestingly, the As concentrations in the Fe-rich lithologies are up to 1400 times in excess of concentrations in hydrothermal fluids from the East Pacific Rise and 4600 times over the values reported for the Mid-Atlantic Ocean Ridge (Breuer and Pichler, 2013). Further, the average As concentration in the Fe-rich lithologies is 18 and 9 times above those present in the overlying siliciclastic and underlying carbonates in the Taghdout Formation, respectively. This observation is most parsimoniously interpreted to represent the levels of As concentrations in the waters that formed the different successions based on the assumption that the

743 Fe content of the sediments did not skew the data towards the enrichment of
744 As by the ferric Fe in the Wanimzi Formation. This appears not to have been
745 the case considering that the As/Fe ratios in these sediments are generally
746 homogenous across the entire succession (Appendix O). Moreover, the
747 comparable behaviors of As and Sb (Fig. 6a-b) across the studied successions
748 have previously been related to water mass type and interaction with rocks by
749 hydrothermal fluids and migrating hydrothermal plumes emitted by active vents
750 (Wu et al., 2017; Zeng et al., 2018). Importantly, 63 % of the As in the Fe-rich
751 lithologies is explained by a positive covariance with Fe (Fig. 12a), similar to
752 observations between hydrothermal ferric Fe and As (e.g., Feely et al., 1991;
753 Chi Fru et al., 2015). Similar to the behavior of hydrothermal ferric Fe and V, a
754 positive correlations was observed between V and Fe in the ironstones (Fig.
755 12b; Feely et al., 1998). Only a weak positive correlation was observed for Fe,
756 Cu, and none for Mo. As and Mo showed a strong positive correlation (Fig.
757 12c), suggesting they likely had the same hydrothermal source considering that
758 both can be strongly enriched in hydrothermal fluids (German and Seyfried,
759 2014). However, the lack of correlation between Fe and Mo implies that
760 precipitation of Mo into the ironstones may have been independent of ferric Fe
761 precipitation.
762 The As data suggest that the microbial communities associated with the
763 water mass that formed the Fe-rich lithologies would have had to combat the
764 dramatic effects of arsenic toxicity, which include inhibiting the synthesis and
765 function of proteins by As(III) in reducing environments and cell phosphate
766 uptake and metabolism by As(V) in oxygenated habitats (Cervantes et al.,
767 1994; Smedley and Kinniburgh, 2002). Such a scenario would have impeded
768 primary production, as is common in modern oceans, compared to the
769 reference arsenic-poor settings. This would have had major implications for
770 carbon fixation, organic carbon burial, and oxygenation by the activities of the
771 marine cyanobacteria (Dyhrman and Haley, 2011; Wurl et al., 2013; Saunders
772 and Rocap, 2016; Giovannoni et al., 2019). However, a full set of arsenic
773 detoxifying genes believed to have been present by the earliest Tonian Period
774 (Chen et al., 2020), together with widespread mechanisms for controlling genes
775 that select for phosphate at the expense of As(V), would have alleviated this
776 situation to some extent. These genes have been shown to be abundant in a

modern submarine hydrothermal system exposed to hydrothermal fluids containing 3000 times more As than seawater concentrations (Chi Fru et al., 2018b). This would have partially mitigated As toxicity when the deep-sea deoxygenated hydrothermal As-rich fluids rose and mixed with the shallow seawater on the coast of the WAC, possibly supporting asentrophic microbial activity in the deoxygenated waters (Visscher et al., 2020). Similarly, key nutrients like Mo and V, critical for nitrogen fixation and thus primary production in the early oceans (Zhang et al., 2014), would have equally contributed to maintaining a good degree of primary production as reflected by the photosynthetic $\delta^{13}C_{org}$ proxy signature preserved in the ironstones.

5.2.3. Insights from Fe isotope systematics

The $\delta^{56}Fe$ values of modern sulfide-rich hydrothermal fluids at seafloor mid-ocean ridges typically range from -1.26‰ to -0.14‰ with a reported average of -0.52‰ (Sharma et al., 2001; Severmann et al., 2004; Bennett et al., 2009; Li et al., 2017; Rouxel et al., 2016). These $\delta^{56}Fe$-depleted values are balanced by enriched seawater $\delta^{56}Fe$ ratios that vary from -0.64‰ to up to 0.80‰ with an estimated average of 0.34‰ (Bennet et al., 2009; Rouxel et al., 2016; Fitzsimmons et al., 2016, 2017; Karl et al., 2016; Li et al., 2017; Lough et al., 2017). In contrast, a mean value of +0.1‰ has been suggested for sulfide-depleted hydrothermal fluids from Pele's pit in the Hawaiian Loihi submarine volcanic hotspot similar to neighboring seafloor basaltic $\delta^{56}Fe$ ratios (Rouxel et al., 2018). The $\delta^{56}Fe$ values are commonly controlled by a combination of biological and abiological processes, including chemical precipitation of Fe oxides during abiotic and biotic oxidation of Fe with oxygen, anoxic precipitation of Fe sulfide, microbial reduction of Fe, water rock interactions, and phase separation (e.g., Rouxel et al., 2008; Severmann et al., 2004; Li et al., 2017; Rouxel et al., 2018; Heard and Dauphas, 2020). However, there is a consensus that net seawater $\delta^{56}Fe$ values are generally heavier relative to submarine hydrothermal fluids (Radic et al., 2011; Conway et al., 2014, 2015). For instance, high temperature hydrothermal fluids with light $\delta^{56}Fe$ ratios of -0.23‰ from the Rainbow hydrothermal vents precipitate and deliver Fe with $\delta^{56}Fe$ values similar to those recorded in the receiving deep North Atlantic seafloor sediments (e.g., Severmann et al., 2004). Further, studies have shown that Fe

isotopes are more sensitive to local environmental conditions (e.g., precipitating authigenic sulfide and Fe oxyhydroxide minerals) than to extant biological and abiological processes (Lough et al., 2017; Rouxel et al., 2018). This implies that Fe isotopes are best applied as tracers of environmental change processes. The source and sink of Fe in the ocean and global Fe biogeochemical cycling are dependent on our knowledge of fluxes between various Fe pools and their associated isotopic signatures. Therefore, quantitative precipitation of primary Fe from seawater and hydrothermal fluids is expected to conservatively display δ^{56}Fe values reflecting sources and variable mixing with seawater. Similarly, examining the behavior of Fe isotopes during the dispersal and transportation of hydrothermal plumes through seawater can provide information on the sources and sinks of Fe to seawater as well as the influence of hydrothermal Fe in the deposition of Fe Formations on ancient continental margins.

The variability of δ^{56}Fe in the Fe-rich sedimentary units from the Wanimzi Formation are more similar to the signatures of hydrothermal fluids than for modern oxic seawater values that are often more homogenously heavy. This view is supported by the transition from light to exceptionally heavy δ^{56}Fe values in the overlying reference Fe-poor stromatolitic succession shown to have the least hydrothermal influence by their REE+Y and trace metal composition. Because Fe is insoluble in oxygenated seawater, its concentration in the modern ocean is usually in the nM to pM range, while µM to mM concentrations are documented in anoxic hydrothermal fluids and plumes (Elderfield and Schultz, 1996; Bennett et al., 2008; Fitzsimmons et al., 2014; Resing et al., 2015; Lough et al., 2017). Similar to this observation, the Fe-rich lithologies, which were deposited beneath anoxic bottom waters, are 26 times more enriched in Fe than the stromatolitic rocks, which we argue formed in full bottom water oxygenated conditions. Moreover, these Fe-rich lithologies contain δ^{56}Fe signatures that on average are light (-0.03‰) compared to the heavy values of up 0.52‰ measured in the stromatolitic Fe-poor reference rocks that are believed to have experienced the least hydrothermal influence of all the samples. Further, mid-ocean ridge plumes from the East Pacific Rise with similar δ^{56}Fe values of -0.91‰ and -0.03‰ were interpreted to have resulted from variable mixing of hydrothermal fluids with seawater, lithospheric interactions, and biogenic Fe cycling (Rouxel et al., 2016).

The lowest $\delta^{56}Fe$ value of -0.41‰ in the Wanimzi ironstones has been reported for Fe particles in endmember hydrothermal plumes following systematic stripping of light ^{56}Fe by Fe sulfide minerals (Rouxel et al., 2016). In the absence of direct evidence for the sulfide content of the original fluids that formed the ironstones, Mo/W ratios are used as proxies for Mo depletion and W enrichment during the precipitation of particulate sulfide minerals (Mohajarin et al., 2016; Bauer et al., 2017; Dellwig et al., 2019). Upon transition to conditions that support the production of ferric Fe, W is preferentially sequestered relative to Mo. The variable levels of Mo/W ratios in the Fe-rich lithologies (Fig. 6g) may therefore be linked to the influence of sulfide fluids. However, owing to the absence of correlation amongst Mo, W and Fe, it is suggested that Mo and W enrichments in the ironstones were not the direct results of Fe precipitation. The positive correlation between Mo and As in the Fe-enriched lithologies (Fig. 12c), both being strong chalcophiles possessing high affinities for sulfide, suggests low sulfide concentration in the source vent fluids. This, allowed substantial amounts of As, Mo, and Fe to escape precipitation with vent sulfides and subsequent enrichments in the ironstones. The mainly heavier $\delta^{56}Fe$ signal of up to +0.61‰ recorded in the Fe-poor siliciclastic Imi n'Tizi reference rocks and their REE+Y distribution, are comparable to values recorded in some modern seawater. In addition, these reference Fe-poor rocks lack evidence for strong hydrothermal influence, while the lighter $\delta^{56}Fe$ values in the ironstones are more consistent with a hydrothermal source.

Our $\delta^{56}Fe$ values fall within the range for published Proterozoic Fe formations believed to have been influenced by varying degrees of hydrothermal input (Planavsky et al., 2010; Yan et al., 2010; Halverson et al., 2011; Li et al., 2017; Heard and Dauphas, 2020; Fig. 11b). The simple hematite and quartz mineralogy of the Wanimzi ironstones is comparable to the reported predominance of hematite in syn-glacial Neoproterozoic Snowball Fe formations (Bekker et al., 2010; Halverson et al., 2011; Cox et al., 2013; Lechte et al., 2013). However, the narrower range of $\delta^{56}Fe$ values in the Wanimzi ironstones (-0.41‰ to 0.35‰) are more similar to modern hydrothermal $\delta^{56}Fe$ seafloor deposits (Planavsky et al., 2010; Rouxel et al., 2008; 2016; 2018), while the wider range in $\delta^{56}Fe$ values of -0.7‰ to 1.2‰ in Neoproterozoic syn-

879 glacial Fe formations compared to the narrower records in the Wanimzi Fe-rich
880 lithologies, point perhaps to varying degrees of partial Fe oxidation (e.g.,
881 Halverson et al., 2011; Table 3).
882 The data suggest that the relationship between Fe concentrations and
883 Zn/Co ratios may be a stronger indicator of the degree of hydrothermal
884 influence than the relationship between $\delta^{56}Fe$ and Zn/Co ratios in the studied
885 succession. For instance, although $\delta^{56}Fe$ lacked a significant negative
886 correlation with Fe concentrations and the Zn/Co ratios, a goodness of fit
887 positive correlation between Fe and Zn/Co points to hydrothermal activity
888 contributing to at least 64 % of bulk Fe enriched in the Fe-rich sediments
889 (Appendix P). Further, while Fe concentrations in the Wanimzi Formation are
890 much elevated relative to the underlying Paleoproterozoic Taghdout
891 carbonates and the overlying Ediacaran Imi n-Tizi siliciclastic deposits, the
892 Zn/Co ratios of the Wanimzi ironstones are lower compared to the Fe-poor
893 carbonates and higher relative to the Fe-poor Ediacaran deposit. This suggests
894 potential mixing of seawater with Fe-poor hydrothermal fluids during the
895 deposition of the Taghdout carbonates and progressively negligible
896 hydrothermal influence during the deposition of the siliciclastic rocks above the
897 Wanimzi ironstones. The positive $\delta^{56}Fe$ values of the Fe-poor, non-
898 hydrothermal siliciclastic sediments above the Wanimzi ironstones, linked to
899 low seawater Fe concentration and Zn/Co ratios, reflect expected heavier
900 $\delta^{56}Fe$ values resulting from low seawater Fe concentration and hydrothermal
901 activity in some modern seawater settings. Moreover, quantitative and partial
902 oxidation of Fe by biotic and abiotic processes, would result in quantitative or
903 partial fractionation of Fe isotopes between the precipitated Fe(III) and residual
904 dissolved hydrothermal Fe(II), decoupling the $\delta^{56}Fe$ and Zn/Co signals.
905
906 *5.3. Redox depositional conditions*
907 The pronounced Ce_{SN} depletion observed in our samples is a feature common
908 to modern oxygenated seawater (e.g., Bau and Dulski, 1996; Singh and
909 Rajamani, 2001; Shields et al., 2004; Bau and Koschinsky, 2009). Statistical
910 test for the redox state of seawater by the calculated true negative Ce/Ce*
911 anomaly, indicates extensive oxygenation of the WAC margin (Fig. 10a; Bau,
912 1996; Planavsky et al., 2010). However, redox reconstruction using the Fe-

based redox proxy (Poulton and Canfield, 2005; Poulton and Canfield, 2011; Clarkson et al., 2014) suggests deposition of both the reference siliciclastic carbonates from the Taghdout Formation and the Wanimzi ironstone lithologies occurred beneath a deoxygenated water column, while full water column oxygenation coincides with the reference Fe-poor siliciclastic Imi n'Tizi rocks. Persistent ferruginous conditions were widespread at this time while euxinia is not supported by the data.

The siliciclastic detritus derived from continental weathering likely influenced the REE+Y distribution patterns, as supported by the corresponding average Y/Ho clastic values. Importantly, because the entire sequence is siliciclastic, the divergent redox conditions indicated by the Ce/Ce* and the Fe-based redox proxies, are interpreted to reflect the unique ability of the Fe-based redox proxy to record the emergent anoxic bottom water depositional conditions induced by the fluids that delivered Fe to the continental margin. Further, as the chemocline deepens, the Y/Ho ratios are expected to decrease as the Ce/Ce* anomaly increases because of effective dissolution of Fe(III)(oxyhydr)oxide particles that tend to be relatively enriched in Ho and Ce (Bau et al., 1997; Planavsky et al., 2010; Halverson et al., 2011). Instead the lack of an inverse correlation between Y/Ho and Ce/Ce*, together with static average Y/Ho ratios across the sampled section, are consistent with a stable shallow marine platform experiencing little or no change in the depth of the chemocline.

We propose that the shallow margins of the WAC were fully oxygenated prior to the process that introduced Fe-rich fluids to the platform waters. This suggestion implies that the process that conveyed the ferruginous fluids to the WAC margin to promote kinetic deoxygenation of the shallow seawater mass was too rapid to allow equilibration with the atmosphere and the establishment of a stable chemocline with fluctuating depth. Moreover, the Y/Ho ratios being more similar to composite shale and clastic sediment values, imply that the REE+Y values are influenced by contribution of clast weathered from the upper continental crust, relative to hydrothermal input. This is consistent with the lack of meaningful correlation between the inferred hydrothermal Fe and corresponding Y/Ho ratios, a strong seawater Ce_{SN} and subtle Eu_{SN} anomalies, the latter being undetectable in some cases. The negative $\delta^{57}Fe$ correlation to Y/Ho ratios recorded in syn-glacial Neoproterozoic Fe formations isolated from

947 continental contamination by detrital material, and marked by the scavenging
948 of REE+Y by Fe oxides precipitated from a deepening chemocline (Halverson
949 et al., 2011), is not observed in our samples.
950 Instead, the Fe-based redox proxy points to a sudden deoxygenation
951 event of what was likely a fully oxygenated shallow water mass by anoxic
952 submarine hydrothermal plumes released from a distal anoxic deep-sea
953 source. Attenuation of the REE+Y hydrothermal signal is interpreted to be the
954 product of long distance plume transportation to the continental margin. As a
955 result, vigorous mixing of the migrating plume with seawater and particle
956 precipitation, systematically weakened the hydrothermal REE+Y signal (Fig.
957 13). This observation is supported by the attenuated hydrothermal Eu
958 signature, reported for various Precambrian IFs to be related to high
959 temperature hydrothermal provenance of Fe (Michard, 1989; Klein and Beukes,
960 1993; Halverson et al., 2011).
961 The Fe-based redox trends are supported by variations in associated
962 redox sensitive trace metals such as elevated levels of U and V in the Fe-rich
963 lithologies (Fig. 6-c; Table 2). For example, U concentrations average 1.6±0.6
964 ppm in the ironstones compared to 1.0±0.5 ppm and ~0.4±0.0 ppm in the
965 reference Fe-poor siliciclastic rocks above and beneath the Fe-rich sequence,
966 respectively. Similarly, V concentrations averaged 70.8±50.6 relative to
967 36.3±6.6 ppm and ~8.5 for the Fe-poor rocks above and below the Fe-rich layer,
968 respectively. These average values are below continental crust concentrations
969 of 2.8 ppm and 107 ppm for U and V, respectively (McLennan (2001).
970 Nonetheless, the higher co-enrichment of U and V in the Fe-rich lithologies
971 relative to the Fe-poor lithologies, is consistent with the strong anoxic, non-
972 euxinic, ferruginous depositional conditions established by our Fe speciation
973 analysis in Figure 10b-c (e.g., Tribovillard et al., 2006; Scott et al., 2008; Scott
974 & Lyons, 2012). Equally, the lack of any meaningful Mo enrichment is consistent
975 with the absence of euxinic conditions suggested by our Fe speciation data
976 across the studied section (Fig. 6a).
977
978 **6. Conclusions**
979 We present a siliciclastic ironstone deposit estimated to be of Early
980 Neoproterozoic age in the Anti Atlas Mountains of Morocco, marked by a unique

hematite enrichment style different from that reported for most Precambrian Fe Formations. The data indicate a predominantly anoxic deep ocean that enabled the transportation and delivery of strongly reducing submarine hydrothermal plumes to an oxygenated early Neoproterozoic shallow marine wave-influenced platform. Here, reduced Fe was mixed with and oxidized by oxygenated seawater and deposited in association with siliciclastic material weathered from the continent. Based on the combined Ce/Ce* anomaly and Fe-based bottom water redox reconstruction, we propose that the marginal shallow seawaters were fully oxygenated until the anoxic hydrothermal fluids upwelled from the deep-sea and rapidly deoxygenated the shallow waters for an extended period of time. This resulted in the oxidation of upwelling reduced hydrothermal ferrous Fe and the deposition of primary ferric Fe that was preserved as hematite in the Wanimzi ironstones. The data further suggest that, in addition to the open oceans being redox stratified to enable large-scale migration of reduced hydrothermal plumes to the WAC margin, the breakup of Rodinia supercontinent may have initiated widespread early Neoproterozoic redox processes that orchestrated extended episodes of widespread shallow seawater anoxia in affected basins. This observation is consistent with the proposition that increased deposition of ferric Fe during the Early Neoproterozoic may have suppressed extensive seawater-atmosphere oxygenation through the scavenging and burial of dissolved phosphate by ferric Fe particles precipitating from seawater (Guilbard et al., 2020).

Acknowledgements

This work was funded by the European Research Council (Grant No. 336092 to ECF). We acknowledge funding support from Hassan II Academy of Science and Technology (HIIAST/SDU/2016.02 El Albani et al.) and the funding fellowship awarded to I. Chraiki).

References

Baratoux, L., Söderlund, U., Ernst, R.E., de Roever, E., Jessell, M.W., Kamo, S., Naba, S., Perrouty, S., Metelka, V., Yatte, D., Grenholm, M., Diallo, D.P., Ndiaye, P.M., Dioh, E., Cournède, C., Benoit, M., Baratoux, D., Youbi, N., Rousse, S., Bendaoud, A., 2019. New U–Pb Baddeleyite ages

of mafic dyke swarms of the West African and Amazonian Cratons: implication for their configuration in supercontinents through time. In: Srivastava, R.J., Ernst, R.E., Peng, P (Eds.), Dyke Swarms of the World: A Modern Perspective, Springer, Singapore, pp. 263–314.

Bau, M., Dulski, P. (1996). Distribution of yttrium and rare-earth elements in the Penge and Kuruman iron-formations, Transvaal Supergroup, South Africa. Pre. Res. 79:37–55. https://doi.org/10.1016/0301-9268(95)00087-9.

Bau, M., Mdler, P., Dulski, P., 1997. Yttrium and lanthanides in eastern Mediterranean seawater and their fractionation during redox-cycling. Mar. Chem. 56:123–131. https://doi.org/10.1016/S0304-4203(96)00091-6.

Bau, M., Dulski, P., 1999. Comparing yttrium and rare earths in hydrothermal fluids from the Mid-Atlantic Ridge: implications for Y and REE behaviour during near-vent mixing and for the Y/Ho ratio of Proterozoic seawater. Chem. Geol. 155:77–90. https://doi.org/10.1016/S0009-2541(98)00142-9.

Bau, M., Koschinsky, A., 2009. Oxidative scavenging of cerium on hydrous Fe oxide: Evidence from the distribution of rare earth elements and yttrium between Fe oxides and Mn oxides in hydrogenetic ferromanganese crusts. Geochem. J. 43:37–47. https://doi.org/10.2343/geochemj.1.0005.

Bauer, S., Blomqvist, S., Ingri, J., 2017. Distribution of dissolved and suspended particulate molybdenum, vanadium, and tungsten in the Baltic Sea. Mar. Chem. 196:135–147. https://doi.org/10.1016/j.marchem.2017.08.010.

Bekker, A., Slack, J.F., Planavsky, N., Krapež, B., Hofmann, A., Konhauser, K.O., Rouxel, O.J., 2010. Iron Formation: The Sedimentary Product of a Complex Interplay among Mantle, Tectonic, Oceanic, and Biospheric Processes. Econ. Geol. 105:467–508. https://doi.org/10.2113/econgeo.107.2.379.

Bennett, S.A., Achterberg E.P., Connelly, D.P., Statham, P.J., Fones, G.R., German, I.C.R., 2008. The distribution and stabilisation of dissolved Fe in deep-sea hydrothermal plumes. Earth Planet. Sci. Letts. 270:157–167. https://doi.org/10.1016/j.epsl.2008.01.048.

Bennett, S.A., Rouxel, O., Schmidt, K., Garbe-Schönberg, D., Statham, P.J., German, C.R., 2009. Iron isotope fractionation in a buoyant hydrothermal plume, 5ºS Mid-Atlantic Ridge. Geochim. Cosmochim. Acta 73:5619–

5634. https://doi.org/10.1016/j.gca.2009.06.027.

Bouougri, E. H., Ait Lahna, A., Tassinari, C. C. G., Basei, M. A. S., Youbi, N., Admou, H., Saquaque, A., Boumehdi, A., Maacha, L., 2020. Time constraints on Early Tonian Rifting and Cryogenian Arc terrane-continent convergence along the northern margin of the West African craton: Insights from SHRIMP and LA-ICP-MS zircon geochronology in the Pan-African Anti-Atlas belt (Morocco). Gond. Res. 85:169–188. https://doi.org/10.1016/j.gr.2020.03.011.

Bouougri, E. H. and Porada, H., 2011. Biolaminated siliciclastic deposits. In: Advances in Stromatolite Geobiology, Lecture Notes in Earth Sciences, Springer Switzerland, pp. 507–524.

Bouougri, E. H. and Saquaque, A., 2004. Lithostratigraphic framework and correlation of the Neoproterozoic northern West African Craton passive margin sequence (Siroua-Zenaga-Bouazzer Elgraara Inliers, Central Anti-Atlas, Morocco): An integrated approach. J. Afri. Earth Sci. 39:227–238. https://doi.org/10.1016/j.jafrearsci.2004.07.045.

Bouougri, E., 2003. The Moroccan Anti-Atlas: the West African craton passive margin with limited Pan-African activity. Implications for the northern limit of the craton – discussion. Pre. Res. 120:179–183. https://doi.org/10.1016/S0301-9268(02)00169-9.

Bouougri, E. and Porada, H., 2002. Mat-related sedimentary structures in Neoproterozoic peritidal passive margin deposits of the West African Craton (Anti-Atlas, Morocco). Sed. Geol. 153:85–106. https://doi.org/10.1016/S0037-0738(02)00103-3.

Bouougri, E. H. and Saquaque, A., 2000. Organisation stratigraphique et structure de la marge Anti-Atlasique du craton Ouest-Africain au sud du Siroua (Néoprotérozoïque, Anti-Atlas central, Maroc). Comptes Rendus de l'Académie Des Sciences - Series IIA - Earth Planet. Sci. 330:753–759. https://doi.org/10.1016/S1251-8050(00)00232-9.

Breuer, C., Pichler T., 2013. Arsenic in marine hydrothermal fluids. Chem. Geol. 348:2–14. https://doi.org/10.1016/j.chemgeo.2012.10.044.

Brocks, J. J., Jarett, A.J.M., Sirantoine, E., Hallmann, C., Hoshino, Y, and Liyanage T., 2017. The rise of algae in Cryogenian oceans and the emergence of animals. Nature 548:578–581. DOI:10.1038/nature23457.

1083 Canfield, D. E., 1998. A new model for Proterozoic ocean chemistry. Nature
1084 396:450–453. DOI:10.1038/24839.
1085 Cervantes, C., Ji, Guangyong, Ramirez, J.L., Silver, S., 1994. Resistance to
1086 arsenic compounds in microorganisms. FEMS Microbiol. Rev. 15:355–
1087 367. https://doi.org/10.1016/0168-6445(94)90069-8.
1088 Chavez, A.D.O., Ernst, R.E., Söderlund, U., Wang, X., Naeraa, T., 2019. The
1089 920–900 Ma Bahia-Gangila lip of the São Francisco and Congo cratons
1090 and link with Dashigou-Chulan lip of North China craton: new insights from
1091 U-Pb geochronology and geochemistry. Pre. Res. 329, 124–137.
1092 https://doi.org/10.1016/j.precamres.2018.08.023.
1093 Chen, S.-C., Suna, G.-X., Yan, Y., Konstantinidis, K.T., Zhange, S-Y., Deng,
1094 Y., Lia, X-M., Cuia, H-L., Musat, F., Popp, D., Rosenh, B.P., Y.-G., Zhu.,
1095 2020. The Great Oxidation Event expanded the genetic repertoire of
1096 arsenic metabolism and cycling. Proc. Natl. Sci. U.S.A. 117:10414-10421.
1097 https://doi.org/10.1073/pnas.2001063117.
1098 Chi Fru, E., Piccinelli, P, Fortin, D., 2012. Insights into the global microbial
1099 community structure associated with iron oxyhydroxide minerals deposited
1100 in the aerobic biogeosphere. Geomicrobiol. J. 29:587–610.
1101 https://doi.org/10.1080/01490451.2011.599474.
1102 Chi Fru, E., Ivarsson, M., Kilias, S.P., Bengtson, S., Belivanova, V., Marone, F.,
1103 Fortin, D., Broman, C., Stampanoni, M., 2013. Fossilized iron bacteria
1104 reveal a pathway to the biological origin of banded iron formation. Nature
1105 Comms 4:2050. DOI: 10.1038/ncomms3050.
1106 Chi Fru, E., Arvestål, E., Callac, N., El Albani, A., Kilias, S., Argyraki, A., and
1107 Jakobsson, M., 2015a. Arsenic stress after the Proterozoic glaciations. Sci.
1108 Rep. 5:17789. DOI: 10.1038/srep17789.
1109 Chi Fru, E., Ivarsson., M, Kilias. S.P, Frings, P.J., Hemmingsson, C., Broman,
1110 C., Bengtson, S., Chatzitheodoridis, E., 2015b. Biogenicity of an Early
1111 Quaternary iron formation, Milos Island, Greece. Geobiology 13:225-244.
1112 https://doi.org/10.1111/gbi.12128.
1113 Chi Fru, E., Rodríguez, N.P., Partin, C.A., Lalonde, S.V., Andersson, P., Weiss,
1114 D.J., El Albani, A., Rodushkin, I., and Konhauser, K.O., 2016a. Cu isotopes
1115 in marine black shales record the Great Oxidation Event. Proc. Natl. Acad.
1116 Sci. U.S.A. 113:4941–4946. https://doi.org/10.1073/pnas.1523544113.

1117 Chi Fru, E., Hemmingsson, C., Holm, M., Chiu, B., Iñiguez E., 2016b. Arsenic-
1118 induced phosphate limitation under experimental Early Proterozoic
1119 oceanic conditions. Earth Planet. Sci. Letts. 434:52–63.
1120 https://doi.org/10.1016/j.epsl.2015.11.009.
1121 Chi Fru, E., Kilias, S., Ivarsson, M., Rattray, J.E., Gkika, K., McDonald, I., He,
1122 Q., Broman, C., 2018a. Sedimentary mechanisms of a modern banded
1123 iron formation on Milos Island, Greece. Solid Earth 9:573–598.
1124 https://doi.org/10.5194/se-9-573-2018.
1125 Chi Fru, F., Callac, N., Posth, N.R., Argyraki, A., Ling, Y.-C., Ivarsson, M.,
1126 Broman, C., Kilias, S.P., 2018b. Arsenic and high affinity phosphate
1127 uptake gene distribution in shallow submarine hydrothermal sediments.
1128 Biogeochemistry 141:41–62. https://doi.org/10.1007/s10533-018-0500-8.
1129 Chi Fru, E., Somogyi, A., El Albani, A., Medjoubi, K., Aubineau, J., Robbins,
1130 L.J., Lalonde, S.V., and Konhauser, K.O., 2019. The rise of oxygen-driven
1131 arsenic cycling at ca. 2.48 Ga. Geology 47:243–246.
1132 https://doi.org/10.1130/G45676.1.
1133 Choubert, G., 1947. L'accident majeur de l'Anti-Atlas, C.R. Acad. Sci. Paris,
1134 224:1172–1173.
1135 Clarkson, M.O., Poulton, S.W., Guilbaud, R., Wood, R.A., 2014. Assessing the
1136 utility of the Fe/Al and Fe-speciation to record water column redox
1137 conditions in carbonate-rich sediments. Chem. Geol. 382:111–122.
1138 https://doi.org/10.1016/j.chemgeo.2014.05.031.
1139 Conway, T.M., John, S.G., 2014. Quantification of dissolved iron sources to the
1140 North Atlantic ocean. Nature 511:212–215. DOI:10.1038/nature12382.
1141 Conway, T.M., John, S.G., 2015. The cycling of iron, zinc and cadmium in the
1142 North East Pacific Ocean-Insights from stable isotopes. Geochim. Cosmo.
1143 Acta 164:262–283. https://doi.org/10.1016/j.gca.2015.05.023.
1144 Cox, G.M., Halverson, G.P., Minarik, W.G., Le Heron, D.P., Macdonald, F.A.
1145 Bellefroid, E.J. Strauss, J.V., 2013. Neoproterozoic iron formation: An
1146 evaluation of its temporal, environmental and tectonic significance. Chem.
1147 Geol. 362:232–249. https://doi.org/10.1016/j.chemgeo.2013.08.002.
1148 Craddock, P.R., Bach, W., Seewald, J.S., Rouxel, O.J. Reeves, E, Tivey, M.K.,
1149 2010. Rare earth element abundances in hydrothermal fluids from the
1150 Manus Basin, Papua New: Indicators of sub-seafloor hydrothermal

1151 processes in backarc basins. Geochim. Cosmochim. Acta 74:675–683.
1152 https://doi.org/10.1016/j.gca.2010.07.003.
1153 Craddock, P.R., Dauphas, N., 2011. Iron and carbon isotope evidence for
1154 microbial iron respiration throughout the Archean. Earth Planet. Sci. Letts.
1155 303:121–132. https://doi.org/10.1016/j.epsl.2010.12.045.
1156 Dauphas, N., John, S.G., Rouxel, O., 2016. Iron isotope systematics. Rev. Min.
1157 Geochem. 82:415–510. http://dx.doi.org/10.2138/rmg.2017.82.11.
1158 Dellwig, O., Wegwerth, W., Schnetger, B., Schulz, H., Arz H.W., 2019.
1159 Dissimilar behaviors of the geochemical twins W and Mo in hypoxic-euxinic
1160 marine basins. Earth-Sci. Rev. 193:1–23.
1161 https://doi.org/10.1016/j.earscirev.2019.03.017.
1162 Douville E., Bienvenu P., Charlou J. L., Donval J. P., Fouquet Y., Appriou P.
1163 and Gamo T., 1999. Yttrium and rare earth elements in fluids from various
1164 deep-sea hydrothermal systems. Geochim. Cosmochim. Acta 63:627–
1165 643. https://doi.org/10.1016/S0016-7037(99)00024-1.
1166 Douvile, E., Charlou, J.L., Oelkers, E.H., Bienvenu, P., C.F. Colon, J., Donval,
1167 J.P., Fouquet, Y., Prieur, D., Appriou, P., 2002. The rainbow vent fluids
1168 (3614VN, MAR): the influence of ultramafic rocks and phase separation on
1169 trace metal content in Mid-Atlantic Ridge hydrothermal fluids. Chem. Geol.
1170 184:37–48. https://doi.org/10.1016/S0009-2541(01)00351-5.
1171 Dyhrman, S.T., Haley, S.T., 2011. Arsenate resistance in the unicellular marine
1172 Di https://doi.org/10.3389/fmicb.2011.00214.
1173 Dymek, R.F., Klein, C., 1988. Chemistry, petrology and origin of banded iron-
1174 formation lithologies from the 3800 MA isua supracrustal belt, West
1175 Greenland. Pre. Res. 39:247–302. https://doi.org/10.1016/S0009-
1176 2541(01)00351-5.
1177 Elderfield H. and Schultz A., 1996. Mid-ocean ridge hydrothermal fluxes and
1178 the chemical composition of the ocean. Annu. Rev. Earth Planet. Sci.
1179 24:191–224. https://doi.org/10.1146/annurev.earth.24.1.191.
1180 El Hadi, H., Simancas, J.F., Martinez-Poyatos, D., Azor, A., Tahiri, A., Montero,
1181 P., Fanning, C.M., Bea, F., Gonzalez-Lodeiro, F., 2010. Structural and
1182 geochronological constraints on the evolution of the Bou Azzer
1183 Neoproterozoic ophiolite (Anti-Atlas, Morocco). Pre. Res. 182:1–14.
1184 https://doi.org/10.1016/j.precamres.2010.06.011.

1185 Ennih, N., Liégeois, J.-P., 2001. The Moroccan Anti-Atlas: the West African
1186 craton passive margin with limited Pan-African activity. Implications for the
1187 northern limit of the craton. Pre. Res. 112:289–302.
1188 https://doi.org/10.1016/S0301-9268(01)00195-4.
1189 Ennih, N., Liégeois, J.P., 2008. The boundaries of the West African craton, with
1190 special reference to the basement of the Moroccan metacratonic Anti-Atlas
1191 belt. Geological Society London, Special Publication 297:1–17.
1192 https://doi.org/10.1144/SP297.1.
1193 Evans, D.A.D., Trindade, R.I.F., Catelani, E.L., D'Agrella-Filho, M.S., Heaman,
1194 L.M., Oliveira, E.P., Söderlund, U., Ernst, R.E., Smirnov, A.V., Salminen,
1195 J.M., 2016. Return to Rodinia? Moderate to high palaeolatitude of the São
1196 Francisco/Congo craton at 920 Ma. Geological Society London, Special
1197 Publication 424:167–190. https://doi.org/10.1144/SP424.1.
1198 Feely, R. A., Trefry, J. H., Lebon, G. T., German C. R., 1998. The relationship
1199 between P/Fe and V/Fe ratios in hydrothermal precipitates and dissolved
1200 phosphate in seawater. Geophy. Res. Lett. 15:2253–2256.
1201 https://doi.org/10.1029/98GL01546.
1202 Feely, R. A., Trefry, J. H., Massoth, G. J., Metz, S. A., 1991. Comparison of the
1203 scavenging of phosphorus and arsenic from seawater by hydrothermal iron
1204 oxyhydroxides in the Atlantic and Pacific Oceans. Deep-Sea Res. 38:617–
1205 623. https://doi.org/10.1016/0198-0149(91)90001-V.
1206 Fischer, W.W., Knoll, H.A., 2009. An iron shuttle for deepwater silica in Late
1207 Archean and early Paleoproterozoic iron formation. GSA Bulletin:
1208 121:222–235. https://doi.org/10.1130/B26328.1.
1209 Fitzsimmons J N., Boyle E.A., Jenkins W.J., 2014. Distal transport of dissolved
1210 hydrothermal iron in the deep South Pacific Ocean. Proc. Natl. Acad. Sci.
1211 U.S.A. 111:16654–16661. https://doi.org/10.1073/pnas.1418778111.
1212 Fitzsimmons J.N., Conway T.M., Lee J. M., Kayser R., Thyng K.M., John S. G.,
1213 Boyle E.A., 2016, Dissolved iron and iron isotopes in the southeastern
1214 Pacific Ocean. Glob. Biogeochem. Cycl. 30:1372–1395.
1215 https://doi.org/10.1002/2015GB005357.
1216 Fitzsimmons J.N., John S.G., Marsay C.M., Hoffman C.L., Nicholas S.L., Toner
1217 B.M., German C.R. and Sherrell R.M., 2017. Iron persistence in a distal
1218 hydrothermal plume sup- ported by dissolved-particulate exchange. Nat.

Geosci. 10:U195–U150. https://doi.org/10.1038/ngeo2900.
Frei, R., Dahl., P.S., Duke, E.F., Frei, K.M., Rintza, H., Frandsson, M.M., Jensen, L.A., 2008. Trace element and isotopic characterization of Neoarchean and Paleoproterozoic iron formations in the Black Hills (South Dakota, USA): Assessment of chemical change during 2.9-1.9 Ga deposition bracketing the 2.4-2.2 Ga first rise of atmospheric oxygen. Pre. Res. 162:441–474. https://doi.org/10.1016/j.precamres.2007.10.005.
Gartman, A., Findlay, A.J., 2020. Impacts of hydrothermal plume processes on oceanic metal cycles and transport. Nat. Geosci. 13:396–402.
German, C.R., and Seyfried, W.E., Jr., 2014. Hydrothermal processes. In Treatise on Geochemistry, 2nd edn. Oxford, Elsevier, Vol. 8, pp. 191–233.
Giovannoni, S.J., Halsey, K.H., Saw, J., Muslin, O., Suffridge, C.P., Sun, J., Lee, C.-P., Moore, E.R., Temperton, B., Noell, S.E., 2019. A parasitic arsenic cycle that shuttles energy from phytoplankton to heterotrophic bacterioplankton. mBio 10:e00246-19. doi:10.1128/mBio.00246-19.
Guilbaud, R., Poulton, S.W., Thompson, J., Husband, K.F., Zhu, M., Zhou, Y., Shields, G.A., Lenton, T.M., 2020. Phosphorus-limited conditions in the early Neoproterozoic ocean maintained low levels of atmospheric oxygen. Nat. Geosci. 13:296–30. https://doi.org/10.1038/s41561-020-0548-7.
Halverson, G.P., Poitrasson, F., Hoffman, P.F., Nédélec, A., Montel, J.-M., Kirby, J., 2011. Fe isotope and trace elements geohemistry of the Neoproterozoic syn-glacial Rapitan iron formation. Earth Planet. Sci. Letts. 309:100–112. https://doi.org/10.1016/j.epsl.2011.06.021.
Haugaard, R., Pecoits, E., Lalonde, S., Rouxel, O., Konhauser, K., 2016. The Joffre banded iron formation, Hammersley Group, Western Australia: Assessing the palaeoenvironment through detailed petrology and chemostratigraphy. Pre. Res. 273:12–37. https://doi.org/10.1016/j.precamres.2015.10.024.
Heard, A.W., Dauphas, N., 2020. Constraints on the coevolution of oxic and sulfidic ocean iron sinks from Archean–Paleoproterozoic iron isotope records. Geology 48:58–362. https://doi.org/10.1130/G46951.1.
Heimann, A., Johnson, C.M., Beard, B.L., Valley, J.W., Roden, E.E., Spicuzza, M.J., Beukes, N.J., 2010. Fe, C, and O isotope compositions of banded iron formation carbonates demonstrate a major role for dissimilatory iron

1253 reduction in ~2.5 Ga marine environments. Earth Planet. Sci. Letts. 294:8–
1254 18. https://doi.org/10.1016/j.epsl.2010.02.015.
1255 Hemmingsson, C., Pitcairn, I.K., Chi Fru, C., 2018. Evaluation of phosphate-
1256 uptake mechanisms by Fe (III)(oxyhydr) oxides in Early Proterozoic
1257 oceanic conditions. Environ. Chem. 15:18–28.
1258 https://doi.org/10.1071/EN17124.
1259 Hoffman, P.F., Abbot, D.S., Ashkenazy, Y., Benn, D.I., Brocks, J., Coheren,
1260 P.A., Cox, G.M., Creveling, J.R., Erwin, D.H., Fairchild, I.J., Ferreira, D.,
1261 Goodman, J.C., Haverson, G.P., Jansen, M.F., Fe Hir, G., Love, G.D.,
1262 Macdonald, F.A., Maloof, A.C., Partin, A.C., Ramstein, G., Rose, B.E.J.,
1263 Rose, C.V., Sadler, P.M., Tziperman, E., Voigt, A., Warren, S.G., 2017.
1264 Snowball Earth climate dynamics and Cryogenian geology-geobiology.
1265 Sci. Adv. 3:e1600983. DOI:10.1126/sciadv.1600983.
1266 Hefferan, K.P., Admou H., Karson, J.A., Saquaque, A., 2000. Anti-Atlas
1267 (Morocco) role in Neoproterozoic Western Gondwana reconstruction. Pre.
1268 Res. 103:89–96. https://doi.org/10.1016/S0301-9268(00)00078-4.
1269 Inglis, J.D., D'Lemos, R.S., Samson, S.D., Admou, H., 2005. Geochronological
1270 constraints on Late Precambrian intrusion, metamorphism, and tectonism
1271 in the Anti-Atlas mountains. The J. Geol. 113:439–450.
1272 https://doi.org/10.1086/430242.
1273 Jessell, M.W., Begg, G.C., Miller, M.S., 2016. The geophysical signatures of
1274 the West African craton. Prec. Res. 274:3–24.
1275 https://doi.org/10.1016/j.precamres.2015.08.010.
1276 Kerrich, R., Said, N., Manikyamba, C., Wyman, D., 2013. Sampling oxygenated
1277 Archean hydrosphere: Implications from fractionations of Th/U and Ce/Ce*
1278 in hydrothermally altered volcanic sequences. Gond. Res. 23:506–525.
1279 https://doi.org/10.1016/j.gr.2012.02.007.
1280 Keyser, W., Ciobanu, C.L., Cook, N.J., Johnson, G., Feltus, H., Johnson, S.,
1281 Dmitrijeva, M., Ehrig, K., Nguyen, P.T., 2018. Petrography and trace
1282 element signatures of iron-oxides in deposits from the middleback Ranges,
1283 South Australia: From banded iron formation to ore. Ore Geol. Rev.
1284 93:337–360. https://doi.org/10.1016/j.oregeorev.2018.01.006.
1285 Klein, C., Beukes, N.J.,1993. Sedimentology and geochemistry of the
1286 glaciogenic late Proterozoic Rapitan Iron-Formation in Canada. Econ.

1287 Geol. 88:542–565. https://doi.org/10.2113/gsecongeo.88.3.542.
1288 Klinkhammer, G.P., Elderfield, H., Edmind, J.M., Mitra, A., 1994. Geochemical
1289 implications of rare earth element patterns in hydrothermal fluids from mid-
1290 ocean ridges. Geochim. Cosmochim. Acta 58:5105–5113.
1291 https://doi.org/10.1016/0016-7037(94)90297-6.
1292 Konhauser, K.O., Hamade, T., Raiswell, R., Morris, R.C., Ferris, F.G.,
1293 Southam, G., Canfield, D.E., 2002. Could bacteria have formed the
1294 Precambrian banded iron formations? Geology 30:1079–1082.
1295 https://doi.org/10.1130/0091-7613(2002)030<1079:CBHFTP>2.0.CO;2.
1296 Konhauser, K.O., Planavsky, N.J., Hardisty, D.S., Robbins, L.J., Warchola,
1297 T.J., Haugaard, R., Lalonde, S.V., Partin, C.A., Oonk, P.B.H., Tsikos, H.,
1298 Lyons, T.W., Bekker, A., Johnson, C.M., 2017. Iron formations: A global
1299 record of Neoarchaean to Palaeoproterozoic environmental history. Earth-
1300 Sci. Rev. 172:140–177. https://doi.org/10.1016/j.earscirev.2017.06.012.
1301 Large, R.R., Halpin, J.A., Lounejeva, E., Danyushevsky, L.V., Maslennikov,
1302 V.V., Gregory, D., Sack, P.J., Haines, P.W., Long, J.A., Makoundi, C.,
1303 Stepanov, S., 2015. Cycles of nutrient trace elements in the Phanerozoic
1304 ocean. Gond. Res. 28:1282–1293.
1305 https://doi.org/10.1016/j.gr.2015.06.004.
1306 Leblanc, M., Lancelot, J., 1980. Interprétation géodynamique du domaine Pan-
1307 Africain de l'Anti-Atlas (Maroc) à partir de données géologiques et
1308 géochronologiques. Can. J. Earth Sci. 17:142–155.
1309 https://doi.org/10.1139/e80-012.
1310 Lechte, M. A., Wallace, M., van Smeerdijk Hood, A., Planavsky, N. 2018.
1311 Cryogenian iron formations in the glaciogenic Kingston Peak Formation,
1312 California. Pre. Res. 310:443-462.
1313 https://doi.org/10.1016/j.precamres.2018.04.003.
1314 Lough, A. J. M., Klar, J. K., Homoky, W. B., Comer-Warner, S. A., Milton, J. A.,
1315 Connelly, D.P., James, R.H., Mills, R.A., 2017. Opposing authigenic
1316 controls on the isotopic signature of dissolved iron in hydrothermal plumes.
1317 Geochim. Cosmochim. Acta 202:1–20.
1318 https://doi.org/10.1016/j.gca.2016.12.022.
1319 Lough, A.J.M. Homoky, W.B., Connelly, D.P., Comer-Warner, S.A., Nakamura,
1320 K., Abyaneh, M.K., Kaulich, B., Mills, R.A., 2019. Soluble iron conservation

and colloidal iron dynamics in a hydrothermal plume. Chem. Geol. 511:225–237. https://doi.org/10.1016/j.chemgeo.2019.01.001.

Lyons, T. W., Reinhard, C. T., and Planavsky, N. J., 2014. The rise of oxygen in Earth's early ocean and atmosphere. Nature 506:307–315. DOI:10.1038/nature13068.

Manikyamba, C., Said, N., Santosh, M., Saha, A., Ganguly, S., Subramanyam, K.S.V., 2018. U enrichment and Th/U fractionation in Archean boninites: Implications for paleo-ocean oxygenation and U cycling at juvenile subduction zones. J. Asian Earth Sci. 157:187–197. https://doi.org/10.1016/j.jseaes.2017.10.009.

McLennan, S.M., 1989. Rare Earth elements in sedimentary rocks: Influence of provenance and sedimentary processes. In: Lipin, B., McKay, G. (Eds.), Geochemistry and mineralogy of the Rare Earth Elements: Mineralogical Society of America, pp. 169–200.

McLennan, S.M., 2001. Relationships between the trace element composition of sedimentary rocks and upper continental crust. Geochem. Geophy. Geosyt. 2: https://doi.org/10.1029/2000GC000109.

Millet, M.-A., Baker, J.A., Payne, C.E., 2012. Ultra-precise stable Fe isotope measurements by high resolution multiple-collector inductively coupled plasma mass spectrometry with a ^{57}Fe–^{58}Fe double spike. Chem. Geol. 304-305:18–25. https://doi.org/10.1016/j.chemgeo.2012.01.021

Mitra A., Elderfield H. and Greaves M. J., 1994. Rare earth elements in submarine hydrothermal fluids and plumes from the Mid-Atlantic Ridge. Marine Chem. 46:217–235. https://doi.org/10.1016/0304-4203(94)90079-5.

Mohajerin, T.J., Helz, G.R., Johannesson, K.H., 2016. Tungsten–molybdenum fractionation in estuarine environments. Geochim. Cosmo. Acta 117:105–119. https://doi.org/10.1016/j.gca.2015.12.030.

Mondillo, N., Balassone G., Boni, M.,Chelle-Michou C., Cretella S., Mormone, A., Putzolu F., Santoro, F., Scognamiglio, G., Tarallo, M., 2019. Rare Earth Elements (REE) in Al- and Fe-(oxy)-hydroxides in bauxites of provence and Languedoc (Southern France): Implications for the potential recovery of REEs as by-products of bauxite mining. Minerals 9:504. https://doi.org/10.3390/min9090504.

1355 Mukherjee, I., Large, R.R., Bull, S., Gregory, D.G., Stepanov, A.S., Ávila, J.,
1356 Ireland, T.R., Corkrey, R., 2019. Pyrite trace-element and sulfur isotope
1357 geochemistry of paleo-mesoproterozoic McArthur Basin: Proxy for
1358 oxidative weathering. Am. Min. 104:1256–1272.
1359 https://doi.org/10.2138/am-2019-6873.
1360 Ganno, S., Laure, N.T.E., Djibril, K.N.G., Arlette, D.S., Cyriel, M., Timoléon, N.,
1361 Paul, N.J., 2017. A mixed seawater and hydrothermal origin of superior-
1362 type banded iron formations (BIF)-hosted Kouambo iron deposit,
1363 Paleoproterozoic Nyong Series Southwestern Cameroon: Constraints
1364 petrography and geochemistry. Ore Geol. 80:860–875.
1365 https://doi.org/10.1016/j.oregeorev.2016.08.021.
1366 Gartman, A., Findlay, A.J., 2020. Impacts of hydrothermal plume processes on
1367 oceanic metal cycles and transport. Nat. Geosci. 13:396–402.
1368 DOI:10.1038/s41561-020-0579-0.
1369 Percoits, E., Gingras, M.K., Barley, M.E., Kappler, A., Posth, N.R., Konhauser,
1370 K.O., 2009. Petrography and geochemistry of the Dales Gorge banded iron
1371 formation: Paragenetic sequence, source and implications for palaeo-
1372 ocean chemistry. Pre. Res. 72:163–187.
1373 https://doi.org/10.1016/j.precamres.2009.03.014.
1374 Planavsky, N., Bekker, A., Rouxel, O.J., Kamber, B., Hofmann, A., Knudsen,
1375 A., Lyons, T.W., 2010. Rare Earth Element and Yttrium compositions of
1376 Archean and Paleoproterozoic Fe formations revisited: new perspectives
1377 on the significance and mechanisms of deposition. Geochim. Cosmochim.
1378 Acta 74:6387–6405. https://doi.org/10.1016/j.gca.2010.07.021.
1379 Planavsky, N., Rouxel, O., Bekker, A., Hofmann, A., Little, C.T.S., Lyons., 2012.
1380 Iron isotope composition of some Archean and Proterozoic iron formations.
1381 Geochim. Cosmo. Acta 80:158–169.
1382 http://dx.doi.org/10.1016/j.gca.2011.12.001.
1383 Poulton, S.W., Krom, M.D., Raiswell, R., 2004. A revised scheme for the
1384 reactivity of iron (oxyhydr)oxide minerals towards dissolved sulfide.
1385 Geochim. Cosmochim. Acta 68:3703–3715.
1386 https://doi.org/10.1016/j.gca.2004.03.012.
1387 Poulton, S.W., Canfield, D.E., 2005. Development of a sequential extraction
1388 procedure for iron: Implications for iron partitioning in continentally derived

particulates. Chem. Geol. 214:209–221. https://doi.org/10.1016/j.chemgeo.2004.09.003.

Poulton, S.W., Canfield, D.E., 2011. Ferruginous Conditions: A dominant feature of the ocean through Earth's history. Elements 7:107–112. https://doi.org/10.2113/gselements.7.2.107.

Radic A., Lacan, F., Murray, J.W., 2011. Iron isotopes in the seawater of the equatorial Pacific Ocean: New constraints for the oceanic iron cycle. Earth and Planet. Sci. Letts. 306:1–10. https://doi.org/10.1016/j.epsl.2011.03.015.

Raiswell, R., Hardisty, D.S., Lyons, T.W., Canfield, D.E., Owens, J.D., Planavsky, N.J., Poulton, S.W., Reinhard, C.T., 2018. The iron paleoredox proxies: A guide to the pitfalls, problems and proper practice. Am. J. Sci. 318:491–526. DOI: https://doi.org/10.2475/05.2018.03.

Reinhard, C.T., Planavsky, N.J., Robbins, L.J., Partin, C.A., Gill, B.C., Lalonde, S.V., Bekker, A., Konhauser, K.O., Lyong, T.W., 2013. Proterozoic ocean redox and biogeochemical stasis. Proc. Natl. Acad. Sci. U.S.A. 110:5357–5362. https://doi.org/10.1073/pnas.1208622110.

Reinhard, C.T., Planavsky, N.J., Gill, B.C., Ozaki, K., Robbins, L.J., Lyons, T.W., Fischer, W.W., Wang, C., Cole, D.B., Konhauser, K.O., 2017. Evolution of the global phosphate cycle. Nature 541:386–389. DOI:10.1038/nature20772.

Resing J. A., Sedwick P. N., German C. R., Jenkins W. J., Moffett J. W., Sohst B. M. and Tagliabue A., 2015. Basin-scale transport of hydrothermal dissolved metals across the South Pacific Ocean. Nature 523:U140–U200.

Robbins, L.J., Konhauser, K.O., Warchola, T.J., Homann, M., Thoby, M., Foster, I., Mloszewska, A.M., Alessi, D.S., Lalonde, S.V., 2019. A comparison of bulk versus laser ablation trace element analysis in banded iron formations: Insights into the mechanisms leading to compositional variability. Chem. Geol. 506:197–224. https://doi.org/10.1016/j.chemgeo.2018.12.036.

Rouxel, O., Dobbek, N., Ludden, J., Fouquet, Y., 2003. Iron isotope fractionation during oceanic crust alteration. Chem. Geol. 202:155–182. https://doi.org/10.1016/j.chemgeo.2003.08.011.

Rouxel, O.J., Bekker, A., Edwards, K.J., 2005. Iron isotope constraints on the

Archean and Paleoproterozoic ocean redox state. Science 307:1088–1091. http://dx.doi.org/10.1126/science.1105692.

Rouxel, O., Shanks Iii, W.C., Bach, W., Edwards, K.J., 2008. Integrated Fe- and S-isotope study of seafloor hydrothermal vents at East Pacific rise 9-10°N. Chem. Geol. 252:214–227. https://doi.org/10.1016/j.chemgeo.2008.03.009.

Rouxel, O., Toner, B.M., Manganini, S.J., German, C.R., 2016. Geochemistry and iron isotope systematics of hydrothermal plume fall-out at East Pacific Rise 9°50′N. Chem. Geol. 441:212–234. https://doi.org/10.1016/j.chemgeo.2016.08.027.

Rouxel, O., Toner, B., Germain, Y., Glazer, B., 2018. Geochemical and iron isotopic insights into hydrothermal iron oxyhydroxide deposit formation at Loihi Seamount. Geochim. Cosmo. Acta 220:449-482. https://doi.org/10.1016/j.gca.2017.09.050.

Sander, S. G. & Koschinsky, A., 2011. Metal flux from hydrothermal vents increased by organic complexation. Nat. Geosci. 4:145–150.

Saunders, J.K., Rocap, G., 2016. Genomic potential for arsenic efflux and methylation varies among global *Prochlorococcus* populations. The ISME J. 10:197–209.

Saquaque, A., Admou, H., Karson, J.A., Hefferan, K.P., Reuber, I., 1989. Precambrian accretionary tectonics in the Bou-Azzer El Graara region, Anti-Atlas. Geology 17:1107–1110. http://dx.doi.org/10.1130/0091-7613(1989)017<1107:PATITB>2.3.CO;2.

Schofield, D.I., Horstwood, M.S.A., Pitfield, P.E.J., Crowley, Q.G., Wilkinson, A.F., Sidaty, H.C.O., 2006. Timing and kinematics of Eburnean tectonics in the central Reguibat shield, Mauritania. J. Geol. Soc. 163:549–560. https://doi.org/10.1144/0016-764905-097.

Schrag, D.P., Higgins, J.A., Macdonald, F.A., Johnston, D.T., 2013. Authigenic carbonate and the history of the global carbon cycle. Science 339:540–543. DOI: 10.1126/science.1229578.

Scott C, Lyons TW, Bekker A, Shen Y, Poulton SW, Chu X, Anbar AD., 2008. Tracing the stepwise oxygenation of the Proterozoic ocean. Nature 452:456–459. DOI:10.1038/nature06811.

Scott, C., Lyons, T.W., 2012. Contrasting molybdenum cycling and isotopic

properties in euxinic versus non-euxinic sediments and sedimentary rocks: Refining the paleoproxies. Chem. Geol. 324–325:19–27. https://doi.org/10.1016/j.chemgeo.2012.05.012.

Severmann, M., Johnson, C.M., Beard, B.L., 2004. The effect of plume processes on the Fe isotope composition of hydrothermally derived Fe in the deep ocean as inferred from the Rainbow vent site, Mid-Atlantic Ridge, 36º14/N. Earth Planet. Sci. Letts. 225:63–76. http://dx.doi.org/10.1016/j.epsl.2004.06.001.

Severmann, S., Lyons, T.W., Anbar, A., McManus, J., Gordon, G., 2008. Modern iron isotope perspective on the benthic iron shuttle and the redox evolution of ancient oceans. Geology 36:487–490. https://doi.org/10.1130/G24670A.1.

Sharma, M., Polizzotto, M., Anbar, A.D., 2001. Iron isotope in hot spring along the Juan de Fuca Rudge. Earth Planet. Sci. Letts. 194:39–51. https://doi.org/10.1016/S0012-821X(01)00538-6.

Shields, G.A., Webb, G.E., 2004. Has the REE composition of seawater changed over geological time? Chem. Geol. 204:103–107. https://doi.org/10.1016/j.chemgeo.2003.09.010.

Shields, G.A., Mills, B.J., 2017. Tectonic controls on the long-term carbon isotope mass balance. Proc. Natl. Acad. Sci. U.S.A. 114:4318–4323. https://doi.org/10.1073/pnas.1614506114.

Singh, P., Rajamani, V., 2001. REE geochemistry of recent clastic sediments from the Kaveri floodplains, southern India: Implication to source area weathering and sedimentary processes. Geochim. Cosmochim. Acta 65:3093–3108. https://doi.org/10.1016/S0016-7037(01)00636-6.

Smedley P.L., Kinniburgh, D.G., 2002. A review of the source, behaviour and distribution of arsenic in natural waters. Appl. Geochem. 17:517–568. https://doi.org/10.1016/S0883-2927(02)00018-5.

Song, H., Jiang, G., Poulton, S. W., Wignall, P. B., Tong, J., Song, H., An, Z., Chu, D., Tian, L., She, Z., Wang, C., 2017. The onset of widespread marine red beds and the evolution of ferruginous oceans. Nat. Comms. 8:399. |DOI: 10.1038/s41467-017-00502-x.

Sperling, E.A., Wolock, C.J., Morgan, A.S., Gill, B.C., Kunzmann, M., Halverson, G.P., Macdonald, F.A., Knoll1, A.H., Johnston, D.T., 2015.

Statistical analysis of iron geochemical data suggests limited late Proterozoic oxygenation. Nature 523:451–454. DOI:10.1038/nature14589.

Stokey, L., 1970. Ferrozine–a new spectrophotometric reagent for iron. Anal. Chem. 42:779–781. https://doi.org/10.1021/ac60289a016.

Stüeken, E. E. Kipp, M., Koehler, M. C., Buick, R. 2016. The evolution of Earth's biogeochemical nitrogen cycle. Earth-Sci. Rev. 160:220–239. https://doi.org/10.1016/j.earscirev.2016.07.007.

Sun, Si., Konhauser, K.O., Kappler, A., Li, Y.-L., 2015. Primary hematite in Neoarchean to Paleoproterozoic oceans. GSA Bulletin 127:850–861.

Thomas, R. J., Fekkak, A., Ennih, N., Errami, E., Loughlin, S.C., 2004. A new lithostratigraphic framework for the Anti-Atlas Orogen , Morocco. *39*, 217–226. https://doi.org/10.1016/j.jafrearsci.2004.07.046.

Thompson, K.J., Kenward, P.A., Bauer, K.W., Warchola, T., Gauger, T., Martinez, R., Simister, R.L., Michiels, C.C., Llrós, M., Reinhard, C.T., Kappler, A., Konhauser, K.O., Crowe, S.A., 2019. Photoferrotrophy, deposition of banded iron formations, and methane production in Archean oceans. Science Advances 5: eaav2869. DOI: 10.1126/sciadv.aav2869.

Tivey, M.K., 2007. Generation of seafloor hydrothermal fluids and associated mineral deposits. Oceanography 20:50–65. https://doi.org/10.5670/oceanog.2007.80.

Toner, B. M. Fakra, S.C., Manganini, S.J., Santelli, C.M., Marcus, M.A., Moffett, J.W., Rouxel, O., German, C.R., Edwards, K.J., 2009. Preservation of iron(II) by carbon-rich matrices in a hydrothermal plume. Nat. Geosci. 2:197–201. DOI:10.1038/ngeo433.

Tostevin, R., Shields, G.A., Tarbuck, G.M., He, T., Clarkson, M.O., Wood, R.A., 2016. Effective use of cerium anomalies as a redox proxy in carbonate-dominated marine settings. Chemical Geology, 438, 146-162. https://doi.org/10.1016/j.chemgeo.2016.06.027.

Toth, J.R., 1980. Deposition of submarine crusts rich in manganese and iron. Geol. Soc. Amer. Bull. 91:52–60. https://doi.org/10.1130/0016-7606(1980)91<44:DOSCRI>2.0.CO;2.

Triantafyllou, A., Berger, J., Baele, J.-M., Diot, H., Ennih, N., Plissart, G., Monnier, C., Watlet, A., Bruguier, O., Spagna, P., Vandycke, S., 2016. The Tachakoucht-Iriri-Tourtit arc complex (Moroccan Anti-Atlas):

1525 Neoproterozoic records of polyphased subduction accretion dynamics
1526 during the Pan-African orogeny. J. Geody. 96:81–103.
1527 https://doi.org/10.1016/j.jog.2015.07.004.
1528 Tribovillard, N., Algeo, T.J., Lyons, T., Riboulleau, A., 2006. Trace metals as
1529 paleoredox and paleoproductivity proxies: An update. Chem. Geol.
1530 232:12–32. https://doi.org/10.1016/j.chemgeo.2006.02.012.
1531 Visscher, P.T., Gallagher, K.L., Bouton, A., Farias, M.E., Kurth, D., Sancho-
1532 Tomás, M., Philippot, P., Somogyi, A., Medjoubi, K., Vennin, E., Bourillot,
1533 R., 2020. Modern arsenotrophic microbial mats provide an analogue for life
1534 in the anoxic Archean. Comm. Earth Environ. 1:24.
1535 https://doi.org/10.1038/s43247-020-00025-2.
1536 Wani, H., Mondal, M.E.A., 2011. Evaluation of provenance, tectonic setting and
1537 paleoredox conditions of the Meso-Neoproterozoic basins of the Bastar
1538 craton, Central Indian Shield: Using petrography of sandstones and
1539 geochemistry of shales. Lithosphere 3:143-154.
1540 https://doi.org/10.1130/L74.1.
1541 Weber, K.A., Achenbach, L.A., Coates, J.D., 2006. Microorganisms pumping
1542 iron: Anaerobic microbial iron oxidation and reduction. Nature Rev.
1543 Microbiol. 4:752–764. http://dx.doi.org/10.1038/nrmicro1490.
1544 Wu, D., Purnomo, B.J., Sun, S., 2017. As and Sb speciation in relation with
1545 physico-chemical characteristics of hydrothermal waters in Java and Bali.
1546 J. Geochem. Exp. 173:85–91.
1547 https://doi.org/10.1016/j.gexplo.2016.12.003.
1548 Wurl, O., Zimmer, L., Cutter, G.A., 2013. Arsenic and phosphorus
1549 biogeochemistry in the ocean: Arsenic species as proxies for P-limitation.
1550 Limnol. Oceanogr. 58: 729–740.
1551 https://doi.org/10.4319/lo.2013.58.2.0729.
1552 Yan, B., Zhu, Z.-K., Tang, S.-H., Zhu, M.-Y., 2010. Fe isotope characteristics of
1553 Neoproterozoic BIF in Guangxi Province and its implications. Acta Geol.
1554 Sin. 84:1080–1086.
1555 Yücel, M., Gartman, A., Chan, C. S., Luther, G. W., 2011. Hydrothermal vents
1556 as a kinetically stable source of iron-sulphide-bearing nanoparticles to the
1557 ocean. Nat. Geosci. 4:367–371. DOI:10.1038/ngeo1148.
1558 Zhang, X., Sigman, D.M., Morel, F.M.M., Kraepiel, A.M.L., 2014. Nitrogen

isotope fractionation by alternative nitrogenases and past ocean anoxia. Proc. Natl. Acad. Sci. U.S.A. 111:4782–4787. https://doi.org/10.1073/pnas.1402976111.

Zegeye, A., Bonneville, S., Benning, L.G., Sturm, A., Fowle, D.A., Jones, C., Canfield, D.E., Ruby, C., MacLean, L.C., Nomosatryo, S., Crowe, S.A., Poulton, S.W., 2012. Green-rust formation controls nutrient availability in a ferruginous water column. Geology 40:599–602. https://doi.org/10.1130/G32959.1.

Zeng, Z., Wang, X., Qi, H., Zhu, B., 2018. Arsenic and Antimony in Hydrothermal plumes from the Eastern Manus Basin, Papua New Guinea. Geofluids 6079586. https://doi.org/10.1155/2018/6079586.

Zhou, J.L., Li, X.H., Tang, G.Q., Gao, B.Y., Bao, Z.A., Ling, X.X., Wu, L.G., Lu, K., Zhu, Y.S., Liao, X., 2018. Ca. 890 Ma magmatism in the northwest Yangtze block, South China: SIMS U-Pb dating, in-situ Hf-O isotopes, and tectonic implications. J. Asian Earth Sci. 151, 101–111. https://doi.org/10.1016/j.jseaes.2017.10.029.

Figure Legend

Fig. 1: Geological setting and structural units of the Proterozoic basement of the Anti-Atlas and location of the studied area. (a) Geological sketch map of the Proterozoic basement of the Anti-Atlas showing the three lithostructural domains and the studied area. SAFZ: South Atlas Fault Zone, AAFZ: Anti-Atlas Fault Zone; inset showing the location of the Anti-Atlas domain, (b) simplified map of the Pan-African craton margin strata in the central Anti-Atlas showing location of the studied section (Ag). Tl: Taliwine, Tz: Tazenakht. (Modified from Bouougri et al, 2020).

Fig. 2. (a) Stratigraphic framework of the craton margin successions in the central part of the Anti-Atlas subdivided into Pre-Pan-African and Pan-African megacycles (Bouougri et al., 2016, modified from Bouougri and Saquaque, 2004). Key radiometric ages in blue and red from Bouougri et al. (2020). (b) Simplified measured section showing the sampled horizons including Fe-rich deposits of Wanimzi Fm. and clastic stromatolites of Imi n'Tizi Fm.

Fig. 3. Field features of Fe-bearing rocks of Wanimzi Formation: (a) General view within the upper part of Wanimzi Formation showing the transition from Fe-bearing interval with purple-red color and the overlying white interval without Fe. Dashed blue line indicates the sampled section. (b) Location of the sampled layers, numbered within the studied section shown in (a). (c) Detail within the sampled section showing several Fe-rich thin layers and interbeds consisting of storm deposits with Hummocky cross-stratification (HCS); scale 14.5 cm. (d) Thick Fe-rich and isolated storm bed occurring within heterolithic deposits. Hammer scale is 33 cm.

Fig. 4. Examples of sedimentary and microbial mat-related features of the siliciclastic Wanimzi and Imi n'Tizi Formations (e.g., Bouougri and Porada, 2002, Porada and Bouougri, 2007; Bouougri and Porada, 2011). (a-b) Sandstones with bedding planes showing symmetrical and asymmetrical ripples. (c) Kinneyia-type wrinkles occurring as patches on bedding surfaces of storm deposits. (d) Sand-filled spindle-shaped and randomly oriented cracks. (e) Mat-deformation structures occurring as curved and often bifurcating ridges. (f) Bedding surface preserving subrounded and flat sand clasts. (g-h) Siliciclastic biolamintes (stromatolites) showing domal features on bedding surface (h) and in cross section (g). Scale: (a-e-g) hammer is 33 cm long, (d-f) and (h) coin is 2.4 cm and 2 cm in diameter, respectively.

Fig. 5. Examples of thin section photomicrographs of sampled facies viewed in cross polarized light. (a) Siliciclastic microbial mats at the Imi n'Tizi shallow water stromatolite-rich Formation, showing fine-grained and coarse-grained alternating layers. (b) magnification of the red box in panel (a) showing the

1627 characteristic siliciclastic coarse-grained laminae composed mainly of quartz
1628 grains alternating with a thinner fine-grained clay-rich layer represented by the
1629 red arrow. c-f, Siliciclastic iron-rich deposits showing various well-sorted
1630 rounded and sub-angular quartz grains floating in a black iron-rich matrix in the
1631 Fe-rich lithologies of the Wanimzi Formation. g-i, Examples of thin section
1632 photomicrographs for the siliciclastic carbonate-rich facies from the Taghdout
1633 Formation, characterized by ooids, quartz, carbonates and iron oxides. Ooid-
1634 peloid grainstone, the iron ooids (**1**) are made of microcrystalline calcitic
1635 laminae with radially arranged crystals (light rings) and iron enriched thinner
1636 laminae (dark). (**2**) peloids. (**3**) Oolites relicts showing the dissolution of the
1637 original structure and its replacement by drusy calcite crystals, indicating a
1638 neomorphism process (advanced diagenesis). (**4**) quartz. (**5**) calcite. The
1639 presence of intraclasts (red dashed line) indicate a shallow marine
1640 environment.
1641
1642 Fig. 6. Redox sensitive trace element, organic carbon (C_{org}) and $d^{13}C_{org}$
1643 distribution up the studied stratigraphic section. (a-d), Trace element
1644 distribution for Zn, Cu, Mo, Co, As, V, U, Sb. e, Bulk iron enrichment averaging
1645 22 wt.%, 0.73 wt.% and 1.1 wt.% in the Wanimzi Formation, the overlying
1646 siliciclastic stromatolitic succession and in the underlying siliciclastic
1647 carbonates from the Taghdout Formation, respectively. f, Zn/Co ratios. g, Mo/W
1648 ratio. h, Th/U ratio. i, C_{org} concentration. j, Carbon isotope distribution in C_{org}.
1649 Sil Car= Siliciclastic carbonates.
1650
1651 Fig. 7. PAAS-normalized REE+Y distribution across the succession. a, REE+Y
1652 patterns in the overlying Imi n'Tizi stromatolitic formation. b, REE+Y distribution
1653 in the siliciclastic iron-rich Wanimzi Formation. c, REE+Y distribution in the
1654 underlying Taghdout Formation carbonates.
1655
1656 Fig. 8. Relationship between hydrothermally enriched REES (Nd, La, Ga, Eu
1657 and Ce) and non-hydrothermally enriched REE (Pr), and Zr and Th typically
1658 enriched in siliciclastic deposits.
1659

Fig. 9. (a) Eu anomalies calculated as $(Eu/Eu^*)_{SN1}=Eu_{SN}/(0.67Sm_{SN}+0.33Tb_{SN})$ and as $(Eu/Eu^*)_{SN2}=2\times Eu_{SN}/(Sm_{SN}+Gd_{SN})-(Eu/Eu^*)_{SN1}$ and $(Eu/Eu^*)_{SN2}$ to correct for anomalously high Gd and Tb concentrations, respectively. (b) Light REE (LREE) to high REE (HREE) ratios. (c) Y/Ho ratios. (d), $(La/Y)b_{SN}$ ratio. (e) $(Tb/Yb)_{SN}$ ratio. (f) $(Pr/Yb)_{SN}$ ratio. (g), $(Sm/Yb)_{SN}$ ratio. (h) $(Eu/Sm)_{SN}$ ratio. (i) $(Gd/Gd^*)_{SN}$ ratio. SN=Shale normalized.

Fig. 10. Water column redox conditions determined by REE and Fe-based redox reconstruction. a, Cerium anomaly calculated as $(Ce/Ce^*)_{SN}= Ce_{SN}/(0.5Pr_{SN}+0.5La_{SN})$ and $(Pr/Pr^*)_{SN}= Pr_{SN}/(0.5Ce_{SN}+0.5Nd_{SN})$. Black rings, blue diamonds and purpled filled rings represent the Imi n'Tizi stromatolitic deposit, Wanimzi Formation and the Taghdout carbonates, respectively. With the exception (ironstone) of sample AG12 and CAB (Taghdout carbonate) all data points record true negative Ce Anomalies. b-c, Iron-based bottom water redox reconstruction. S1-S4= Imi n'Tizi stromatolitic deposit. AG01-AG17=Wanimzi Formation. CA1, CA2, CAB= Taghdout carbonates.

Fig. 11. Distribution of iron concentrations and isotopic distribution. a, $\delta^{56}Fe$ and $\delta^{57}Fe$ distribution in the iron-rich and siliciclastic stromatolitic rocks. b, Bulk iron dynamics showing that at less than 5 wt.% Fe concentration (vertical line), $\delta^{56}Fe$ values are more positive and increasingly positive above this value. Above this line strong fractionation of iron produces more negative $\delta^{56}Fe$ values. The asterisks depict two samples (AG08 and AG12) that deviate from the latter observations and are linked to the enrichment of LREE levels, as depicted by LREE/HREE ratios and $(La/Yb)_{SN}$ (See Figure 9b and 9d). c, $\delta^{56}Fe$ distribution in sedimentary marine iron formations deposited at key intervals across Earth history adapted from Planavsky et al. (2012) and Halverson et al. (2011) relative to the black-ringed values obtained in this study. SS=siliciclastic stromatolites.

Fig. 12. Relationship between iron and As (a), iron and V (b) and Mo and As (c) in the Wanimzi ironstones.

1693 Fig. 13. Conceptual model for the formation of the Wanimzi iron-rich shallow
1694 marine ironstone deposit on the Tonian passive continental margin of the WAC.
1695

Table 1. XRD mineralogical data (+=Detected; -=Not detected; ?=Uncertain)

	Lithology	Hematite	Magnetite	Goethite	Ankarite	Siderite	Albite	Kaolinite	Quartz	Chlorite	Dolomite	Calcite	Illite	K-feldspar
S1	Stromatolitic	+	-	-	?	-	+	+	+	-	?	+	+	+
S2	Stromatolitic	+	-	-	?	-	+	+	+	-	?	+	+	+
S3	Stromatolitic	+	-	-	-	-	+	-	+	-	-	-	+	+
S4	Stromatolitic	+	-	-	-	-	+	-	+	-	-	-	+	+
AG17	Iron-Quartz	+	-	-	-	-	+	-	+	-	-	-	+	+
AG16	Iron-Quartz	+	-	-	-	-	-	-	+	-	-	-	+	+
AG15	Iron-Quartz	+	-	-	-	-	-	-	+	-	-	-	+	+
AG14	Iron-Quartz	+	-	-	-	-	-	-	+	-	?	?	+	+
AG13	Iron-Quartz	+	-	-	-	-	-	-	+	-	-	?	+	+
AG12	Iron-Quartz	+	-	-	-	-	-	-	+	-	?	-	+	-
AG11	Iron-Quartz	+	-	-	-	-	-	-	+	-	-	-	-	+
AG10	Iron-Quartz	+	-	-	-	-	-	-	+	-	-	-	+	-
AG09	Iron-Quartz	+	-	-	-	-	-	-	+	-	-	-	-	-
AG08	Iron-Quartz	+	-	-	-	-	-	-	+	-	-	-	+	+
AG07	Iron-Quartz	+	-	-	?	-	-	-	+	-	?	?	+	+
AG06	Iron-Quartz	+	-	-	?	-	-	-	+	-	-	?	+	+
AG05	Iron-Quartz	+	-	-	-	-	-	-	+	-	-	-	?	-
AG04	Iron-Quartz	+	-	-	-	-	-	-	+	-	-	-	+	-
AG03	Iron-Quartz	+	-	-	-	-	-		+	+	?	-	-	-
AG02	Iron-Quartz	+	-	-	-	?	-	+	+	-	-	-	-	-
AG01	Iron-Quartz	+	-	-	-	-	-	-	+	-	-	-	-	-
AG0	Iron-Quartz	+	-	-	-	-	-	-	+	-	-	-	+	-
CA1	Carbonates	+	-	-	-	-	-	-	+	-	+	+	+	-
CA2	Carbonates	+	-	-	-	-	-	-	+	-	+	+	+	+
CAB	Carbonates	+	-	-	-	-	-	-	+	-	+	+	+	+

Table 2. Trace metal(loid) distribution. With the exception of Au measured in ppb concentrations are in ppm. Total Fe was measured by the ferrozine method (Stokey, 1970). Av. UCC (Average Upper Continental Crust concentrations (McLennan, 2001)). All UCC units are in ppm with the exception of Au, Bi, and Pd that are in ppb. AG/SS (Average concentration in iron-rich facies relative to average siliciclastic stromatolitic facies). AG/CAB (Average concentration in iron-rich facies relative to average siliciclastic carbonate lithologies). AG/UCC (Average iron-rich concentrations relative to average upper continental crust concentrations). SS/UCC (Average siliciclastic stromatolitic facies concentration relative to average upper continental crust). CAB/UCC (Average siliciclastic carbonate concentration relative to upper continental crust concentrations).

	As	Au	Ba	Co	Cu	Fe	Hf	Ga	Mo	Nb	Ni
Av. UCC	1.5	1.8	550	17	25	3500	5.8	17	1.5	12	44
S1	3.4	1.6	421	72.4	13.3	4741	13.6	7.7	0.2	6.8	1.6
S2	0.8	1.8	337	68.8	13.7	7298	17.3	8.6	0.2	7.9	2
S3	0.6	0.8	459	65.2	13.2	7292	7.4	11.3	0.2	8.2	2.1
S4	1.6	<0.5	568	39.7	12.1	7292	10.5	12.8	0.2	9.3	1.5
AG17	3.4	<0.5	362	80.2	59.4	34044	6.9	11.5	0.3	6.5	22.8
AG16	33.7	1.3	130	50.8	40.6	384333	5.3	2.6	1.5	2.4	10.1
AG15	6.9	<0.5	156	129.6	12.9	56597	4.6	2.8	0.6	2.8	3.7
AG14	1.9	0.7	319	194.1	13.9	13359	11.6	7.3	0.4	4.6	4.3
AG13	40.1	1	218	114	20.4	157849	8.4	9.3	2.6	5.2	17.2
AG12	4.1	<0.5	381	61.6	8.5	19857	5.6	10.2	1	7.5	3.9
AG11	86.9	1.6	37	29.7	2.8	520283	0.8	2.8	8.9	1.6	12.9
AG10	26.8	2.3	242	64.2	5.7	101151	4.9	6.6	2	5.4	5
AG09	111.3	3.4	57	9.9	4.2	583798	0.8	3.5	6.9	4	9.9
AG08	48.4	1.7	46	80.8	4.3	228895	0.9	5.2	4.8	2.9	6.7
AG07	66.1	0.9	350	86.6	2.4	24710	5.7	8.7	0.3	5.5	10.1
AG06	3.3	<0.5	289	148.7	35.7	18935	4.4	4.5	0.4	2.8	18.1
AG05	2.2	<0.5	539	64.5	7.2	60397	7.2	22.1	0.3	13.4	18.9

AG04	10.6	1.1	184	110.5	23.3	71295	4.7	6.1	1.1	3.2	28.6
AG03	10.6	1.1	336	43	23.3	617303	0.5	5.7	1.1	2.8	28.6
AG02	43.2	2.8	215	37.3	20.1	559723	1.2	3.8	3.4	2.1	31.1
AG01	22	2.6	423	39	120.7	535025	0.6	5.1	2.2	1.4	38.6
AG0	3.5	1.5	491	42.4	29.4	44948	8.2	17	0.3	10.3	12.5
CA1	3.4	9.9	1606	21.1	2.3	13348	1	1.6	0.1	1.4	1.5
CA2	0.1	1.2	383	22.3	10	6458	2.5	2.9	2.2	1.5	3.3
CAB	6.4	1.4	215	38.9	4.6	11872	2.9	2.3	0.1	1.8	2.2
AG/SS	18.2	1.2	0.6	1.3	1.8	33.7	0.4	0.7	10.6	0.6	8.7
AG/CAB	8.8	0.4	0.4	2.8	4.3	21.2	2.1	3.3	2.6	3	6.7
AG/UCC	19.4	0.9	0.5	4.5	1	64	0.8	0.4	1.4	0.4	0.4
SS/UCC	1.1	0.8	0.8	3.6	0.5	1.9	2.1	0.6	0.1	0.7	0.04
CAB/UCC	2.2	2.3	1.3	1.6	0.2	3	0.4	0.1	0.5	0.1	0.05

	Pb	Rb	Sb	Sr	Ta	Th	U	V	W	Zn	Zr
UCC	0.5	112	0.2	350	1	10.7	2.8	107	2	71	190
S1	0.9	94.8	0	17.6	1.4	8.2	1.7	28	448.1	1	18.6
S2	1	95.5	0	16.9	1.3	9.5	0.9	34	491.1	0	21.6
S3	1.2	126.6	0	29.7	1.1	9.1	0.5	41	44.8	2	14.9
S4	1.2	151.1	0.2	21.9	1.1	10.6	1	42	242.6	1	20.3
AG17	1	104.7	0.1	13.3	1.2	9	1.8	56	517.7	8	23.4
AG16	2	22.3	0.9	12.1	0.7	3.7	1.1	17	332.8	10	31.7
AG15	1.8	29.6	0.2	11.3	1.8	3.5	1.3	11	936.5	3	8.9
AG14	0.8	71.4	0.1	17	2.7	6.7	0.9	30	1332.5	1	13.2
AG13	4.9	87.9	2.4	13.1	1.6	6.6	2.1	37	749.9	4	14.2
AG12	0.7	117.4	0.3	16	1.3	8.4	2.2	54	461.3	1	15
AG11	3.4	15.8	5.3	5	0.4	2.8	1.2	74	172.9	2	7.5
AG10	2.9	69.8	2	13	1.2	5.8	0.4	31	486.2	2	12.7

AG09	11.3	25.3	7.8	6.8	0.2	2.2	2.3	81	36.3	2	13.9
AG08	4.3	37.3	3.6	4.5	1	4.5	1	74	580.5	1	21.1
AG07	1.2	84.8	0.1	13.6	1.6	6.4	2.2	44	663.9	4	13.4
AG06	0.8	47.4	0	14.1	2.2	3	1.9	24	1250.8	7	7.2
AG05	1.5	186.7	0.3	20.8	1.8	16	2.3	110	484.3	7	17.2
AG04	1.7	36.6	0.3	8.6	1.9	4.3	1	47	941.9	10	12.9
AG03	1.7	5.5	2.5	9.8	0.2	2	2.2	178	75.2	10	14.4
AG02	5.1	3	2.8	8.8	0.3	2.5	1.9	172	180.8	11	27.6
AG01	3.3	3.5	1.4	11	0.2	1.6	1	139	135.1	15	15.4
AG0	1.6	143.3	0.3	20.8	1.7	12.5	2.5	95	516.2	4	30.9
CA1	14.6	21.5	0.1	1074.4	0.3	10.7	0.4	8	128.3	8	25
CA2	10	44	0	790.8	0.3	7.7	0.4	9	111.9	3.3	18.4
CAB	11	29.1	0	1033.9	0.4	11.7	0.4	<8	227.8	9	20.8
AG/SS	2.6	0.5	33.8	0.6	1	0.6	1.6	2	1.8	5.7	0.9
AG/CAB	0.2	1.9	50.7	0.01	3.7	0.6	4.1	8.3	3.5	0.8	0.8
AG/UCC	5.6	0.5	8.4	0.03	1.2	0.5	0.6	41.6	273.7	0.1	0.1
SS/UCC	2.2	1	0.3	0.1	1.2	0.9	0.4	21.3	153.3	0.01	0.1
CAB/UCC	23.7	0.3	0.2	2.8	0.3	0.9	0.1	5	78	0.1	0.1

Table 3. Carbon, iron, and oxygen isotopic data

	Lithology	$\delta^{13}C_{carbonate}$ (‰ VPDB)	1sd	$\delta^{18}O_{carbonate}$ (‰ VPDB)	1sd	Carbonate (%wt)	$\delta^{13}C_{org}$ (‰ VPDB)	1sd	C_{org} (wt%)	$\delta^{56}Fe$ (‰ IRMM)	2sd	$\delta^{57}Fe$ (‰ IRMM)	2sd
S1	Stromatolitic	-1.84	0.10	-13.13		0.02	-31.80	0.49	0.01	0.61	0.05	0.86	0.14
S2	Stromatolitic	ND*	-	ND*	-	0.01	-30.16	0.49	0.01	0.45	0.05	0.70	0.15
S3	Stromatolitic	-0.33	0.22	-4.00	0.17	0.02	-28.13	0.49	0.02	0.57	0.05	0.88	0.15
S4	Stromatolitic	-4.50	0.18	-9.29	0.16	0.01	-27.87	0.49	0.01	0.45	0.05	0.66	0.14
AG17	Iron-Quartz	ND*	-	ND*	-	ND*	-29.97	0.49	0.03	-0.14	0.05	-0.21	0.14
AG16	Iron-Quartz	ND*	-	ND*	-	ND*	-27.44	0.49	0.01	-0.04	0.05	-0.09	0.14
AG15	Iron-Quartz	ND*	-	ND*	-	ND*	-31.53	0.49	0.03	-0.07	0.05	-0.15	0.14
AG14	Iron-Quartz	-8.72	-	-12.788	-	0.02	-29.82	0.49	0.04	0.03	0.05	0.02	0.14
AG13	Iron-Quartz	ND*	-	ND*	-	ND*	-27.81	0.49	0.03	-0.41	0.05	-0.65	0.14
AG12	Iron-Quartz	ND*	-	ND*	-	ND*	-30.64	0.49	0.02	0.26	0.05	0.52	0.14
AG11	Iron-Quartz	ND*	-	ND*	-	ND*	-28.38	0.49	0.01	-0.19	0.05	-0.31	0.14
AG10	Iron-Quartz	ND*	-	ND*	-	ND*	-29.15	0.49	0.02	0.03	0.05	0.08	0.14
AG09	Iron-Quartz	ND*	-	ND*	-	ND*	-26.12	0.49	0.02	0.06	0.05	0.03	0.14
AG08	Iron-Quartz	ND*	-	ND*	-	ND*	-30.27	0.49	0.02	0.35	0.05	0.54	0.14
AG07	Iron-Quartz	ND*	-	ND*	-	ND*	-30.74	0.49	0.02	0.06	0.05	0.14	0.14
AG06	Iron-Quartz	ND*	-	ND*	-	ND*	-33.03	0.49	0.02	-0.37	0.05	-0.46	0.14
AG05	Iron-Quartz	ND*	-	ND*	-	ND*	-29.33	0.49	0.03	0.11	0.05	0.27	0.14

AG04	Iron-Quartz	-8.72	0.21	-12.788	0.21	ND*	-28.56	0.49	0.02	-0.15	0.05	-0.31	0.14
AG03	Iron-Quartz	ND*	-	ND*	-	ND*	-28.82	0.49	0.02	0.07	0.05	0.30	0.14
AG02	Iron-Quartz	ND*	-	ND*	-	ND*	-27.50	0.49	0.01	-0.22	0.05	-0.28	0.14
AG01	Iron-Quartz	ND*	-	ND*	-	ND*	-22.93	0.49	0.01	-0.09	0.05	-0.08	0.14
AG0	Iron-Quartz	ND*	-	ND*	-	ND*	-29.62	0.49	0.04	0.15	0.05	0.21	0.14
CA1	Carbonates	-0.77	0.13	-14.50	0.10	75	-26.44	0.49	0.04	ND	0.05	ND	0.14
CA2	Carbonates	0.11	0.07	-13.28	0.06	50	-27.41	0.49	0.04	ND	0.05	ND	0.14
CAB	Carbonates	-0.18	0.05	-14.30	0.05	75	-28.41	0.49	0.06	ND	0.05	ND	0.14

ND=Not determined
ND*=Not determined because of extremely low carbonate content

Table 4. Rare Earth Element +Yttrium. S1-S2=Siliciclastic stromatolitic mats. AG17-AG0=Wanimzi Formation. CA1,2,B=Taghdout carbonates.

	Lithology	La	Ce	Pr	Nd	Sm	Eu	Gd	Tb	Dy	Y	Ho	Er	Tm	Yb	Lu	ΣREE+Y	ΣREE
S1	Stromatolite	26.6	52.2	5.46	19.8	3.15	0.59	2.57	0.47	3.1	18.6	0.68	2.1	0.31	2.11	0.35	138.1	119.5
S2	Stromatolite	26.5	56.9	6.11	22.8	3.76	0.75	3.24	0.55	3.49	21.6	0.73	2.53	0.37	2.56	0.42	152.3	130.7
S3	Stromatolite	35.4	67.1	7.12	25.2	3.73	0.65	2.77	0.42	2.71	14.9	0.59	1.8	0.27	1.84	0.31	164.8	149.9
S4	Stromatolite	32.6	66.6	7.46	28.5	4.71	0.88	4.16	0.63	3.63	20.3	0.73	2.39	0.36	2.29	0.37	175.6	155.3
AG17	Iron-Quartz	17.6	35.9	4.45	19.3	6.2	1.46	8.38	1	4.51	23.4	0.79	2.09	0.29	1.84	0.27	127.5	104.1
AG16	Iron-Quartz	12.8	27.6	3.1	12.8	3.84	1.22	8.93	1.26	5.81	31.7	0.94	2.36	0.25	1.64	0.23	114.5	82.8
AG15	Iron-Quartz	10.7	23.7	2.75	10.8	2.56	0.57	2.53	0.32	1.67	8.9	0.29	0.84	0.12	0.84	11	77.6	68.7
AG14	Iron-Quartz	13.5	28	2.79	10	1.72	0.4	1.89	0.35	2.24	13.2	0.47	1.59	0.24	1.58	0.24	78.2	65.0
AG13	Iron-Quartz	23.2	54.4	5.3	19.3	3.28	0.8	3.11	0.48	2.87	14.2	0.52	1.58	0.23	1.56	0.25	131.1	116.9
AG12	Iron-Quartz	41.6	79.7	7.42	26.1	4.08	0.78	3.14	0.43	2.65	15	0.54	1.64	0.24	1.54	0.25	185.1	170.1
AG11	Iron-Quartz	3.8	10.5	1.15	5.3	2.15	0.58	2.54	0.38	1.81	7.5	0.31	0.76	0.11	0.68	0.1	37.7	30.2
AG10	Iron-Quartz	14.7	35.7	3.64	14.7	3.27	0.75	3.05	0.46	2.56	12.7	0.48	1.47	0.19	1.31	0.2	95.2	82.5
AG09	Iron-Quartz	15.3	39.6	4.05	17.6	4.78	1.09	4.67	0.68	3.34	13.9	0.55	1.32	0.16	1.11	0.14	108.3	94.4
AG08	Iron-Quartz	55.6	237.8	28.51	157.2	57.78	9.09	35.91	2.45	6.97	21.1	0.6	1.22	0.19	1.32	0.16	615.9	594.8
AG07	Iron-Quartz	18.7	36.4	4.2	15.9	2.98	0.59	2.52	0.38	2.22	13.4	0.44	1.36	0.21	1.31	0.22	100.83	87.4
AG06	Iron-Quartz	9.3	18.1	5.8	8	1.76	0.4	1.79	0.25	1.4	7.2	0.26	0.79	0.11	0.7	0.12	55.6	48.8
AG05	Iron-Quartz	25.1	51.4	5.8	22.2	4.79	0.93	3.79	0.54	3.12	17.2	0.64	1.94	0.29	1.97	0.28	140	122.8
AG04	Iron-Quartz	6.9	13.2	1.62	7.2	2.61	0.72	4	0.56	2.73	12.9	0.48	1.28	0.17	1.05	0.15	55.6	42.7
AG03	Iron-Quartz	5.5	12	1.42	6.1	2.54	0.81	4.39	0.66	3.08	14.4	0.55	1.26	0.15	0.87	0.12	53.9	39.5
AG02	Iron-Quartz	5.2	10.6	1.4	6.7	2.99	1.04	6.39	1.04	5.28	27.6	0.93	2.28	0.24	1.43	0.19	73.3	45.7
AG01	Iron-Quartz	3.1	6.2	0.91	4.6	2.42	0.84	5.43	0.78	3.38	15.4	0.58	1.33	0.14	0.89	0.11	46.1	30.7
AG0	Iron-Quartz	30.9	61.8	7.18	30	9.15	2.25	12.32	1.46	6.18	30.9	1.11	2.73	0.37	2.41	0.36	199.1	168.2
CA1	Carbonate	35.1	71.1	6.55	24.6	4.82	1.11	4.82	0.77	4.78	25	0.94	2.93	0.41	2.93	0.4	186.3	161.2
CA2	Carbonate	28.1	61.6	5.77	21.3	4.03	0.81	3.45	0.52	3.25	18.4	0.64	1.94	0.26	1.83	0.28	152.2	133.8
CAB	Carbonate	42.7	86	8.14	30.2	5.29	0.96	4.42	0.68	3.95	20.8	0.77	2.21	0.33	2.13	0.33	208.9	188.1

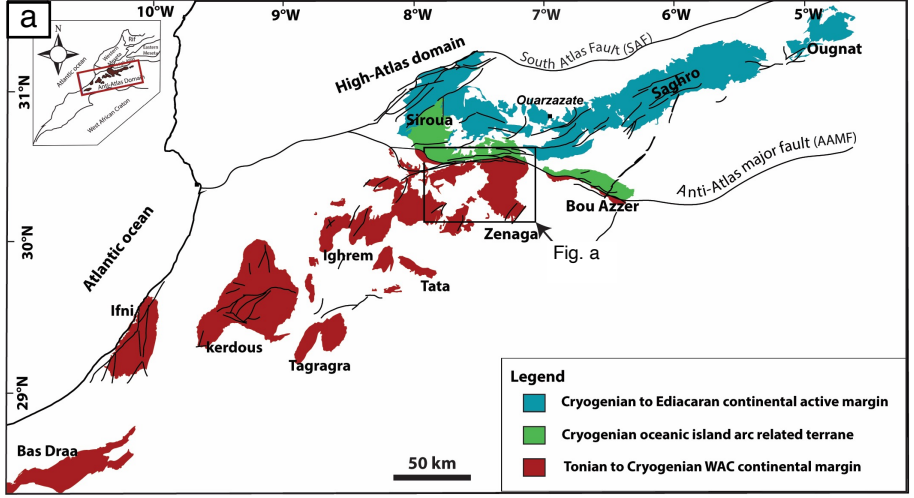
a
10°W
9°W
8°W
7°W
6°W
5°W
31°N
30°N
29°N
High-Atlas domain
South Atlas Fault (SAF)
Ougnat
Saghro
Ouarzazate
Siroua
Anti-Atlas major fault (AAMF)
Bou Azzer
Zenaga
Fig. a
Atlantic ocean
Ighrem
Tata
Ifni
kerdous
Tagragra
Bas Draa
50 km
Legend
Cryogenian to Ediacaran continental active margin
Cryogenian oceanic island arc related terrane
Tonian to Cryogenian WAC continental margin

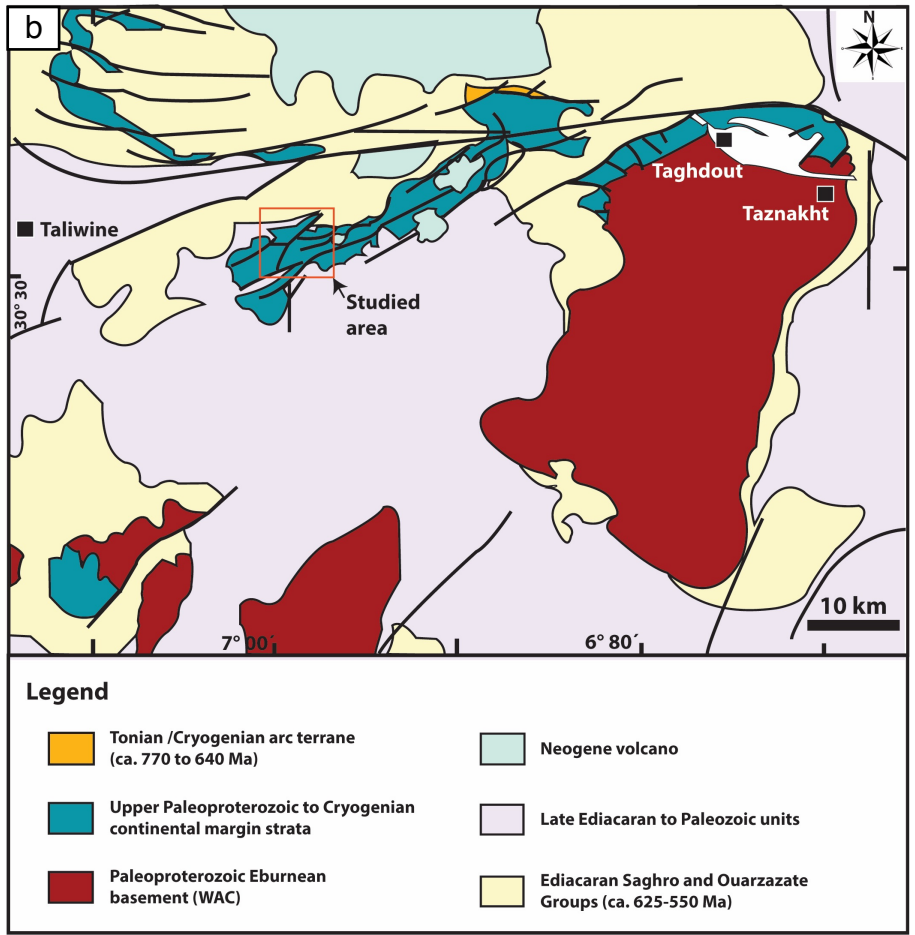
b
N
Taghdout
Taznakht
Taliwine
Studied
area
30° 30
7° 00´
6° 80´
10 km
Legend
Tonian /Cryogenian arc terrane
(ca. 770 to 640 Ma)
Upper Paleoproterozoic to Cryogenian
continental margin strata
Paleoproterozoic Eburnean
basement (WAC)
Neogene volcano
Late Ediacaran to Paleozoic units
Ediacaran Saghro and Ouarzazate
Groups (ca. 625-550 Ma)

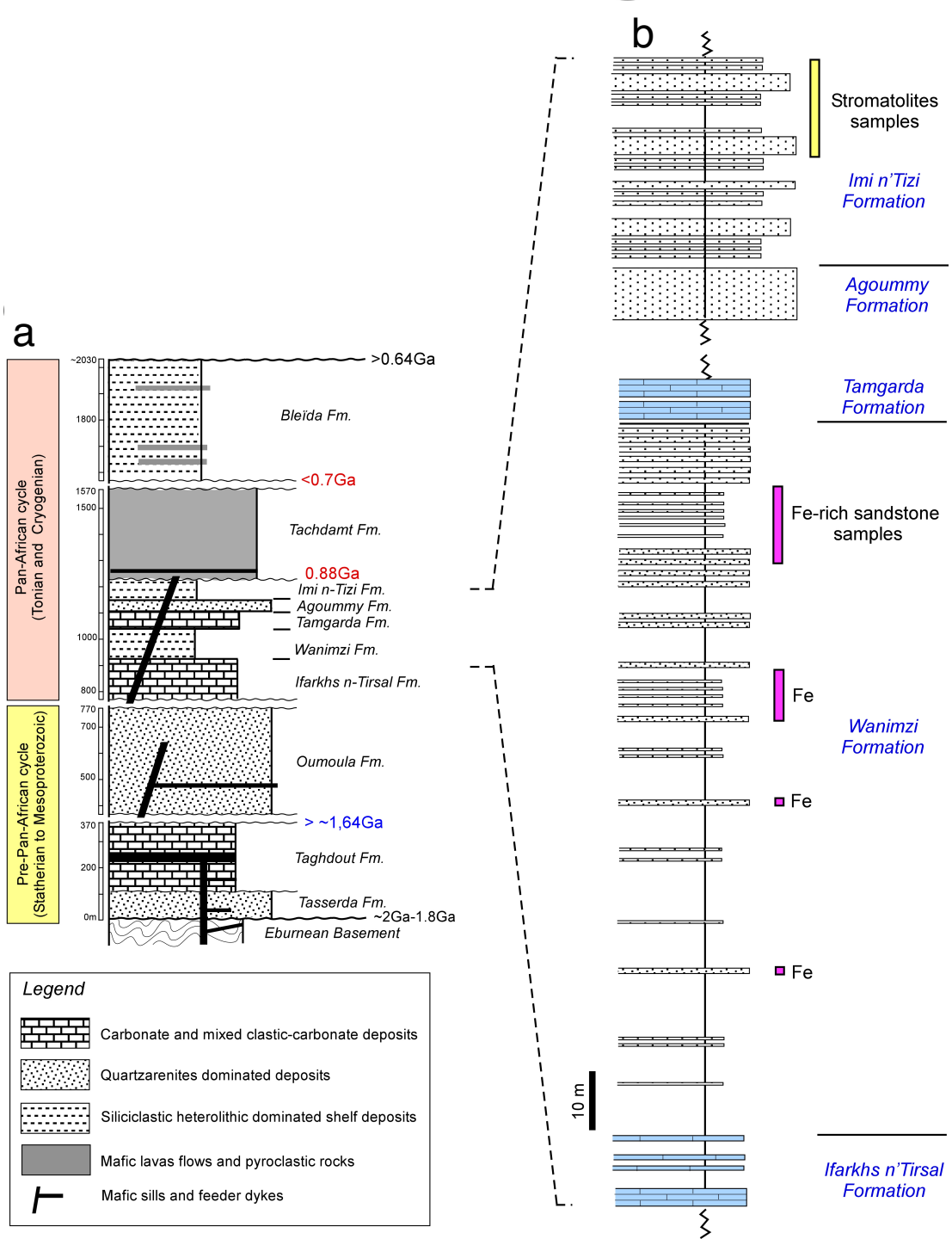
a
b
Pan-African cycle
(Tonian and Cryogenian)
Pre-Pan-African cycle
(Statherian to Mesoproterozoic)
~2030
1800
1570
1500
1000
800
770
700
500
370
200
0m
>0.64Ga
Bleïda Fm.
<0.7Ga
Tachdamt Fm.
0.88Ga
Imi n-Tizi Fm.
Agoummy Fm.
Tamgarda Fm.
Wanimzi Fm.
Ifarkhs n-Tirsal Fm.
Oumoula Fm.
> ~1,64Ga
Taghdout Fm.
Tasserda Fm.
~2Ga-1.8Ga
Eburnean Basement
Legend
Carbonate and mixed clastic-carbonate deposits
Quartzarenites dominated deposits
Siliciclastic heterolithic dominated shelf deposits
Mafic lavas flows and pyroclastic rocks
Mafic sills and feeder dykes
Stromatolites samples
Imi n'Tizi Formation
Agoummy Formation
Tamgarda Formation
Fe-rich sandstone samples
Fe
Wanimzi Formation
Fe
Fe
10 m
Ifarkhs n'Tirsal Formation

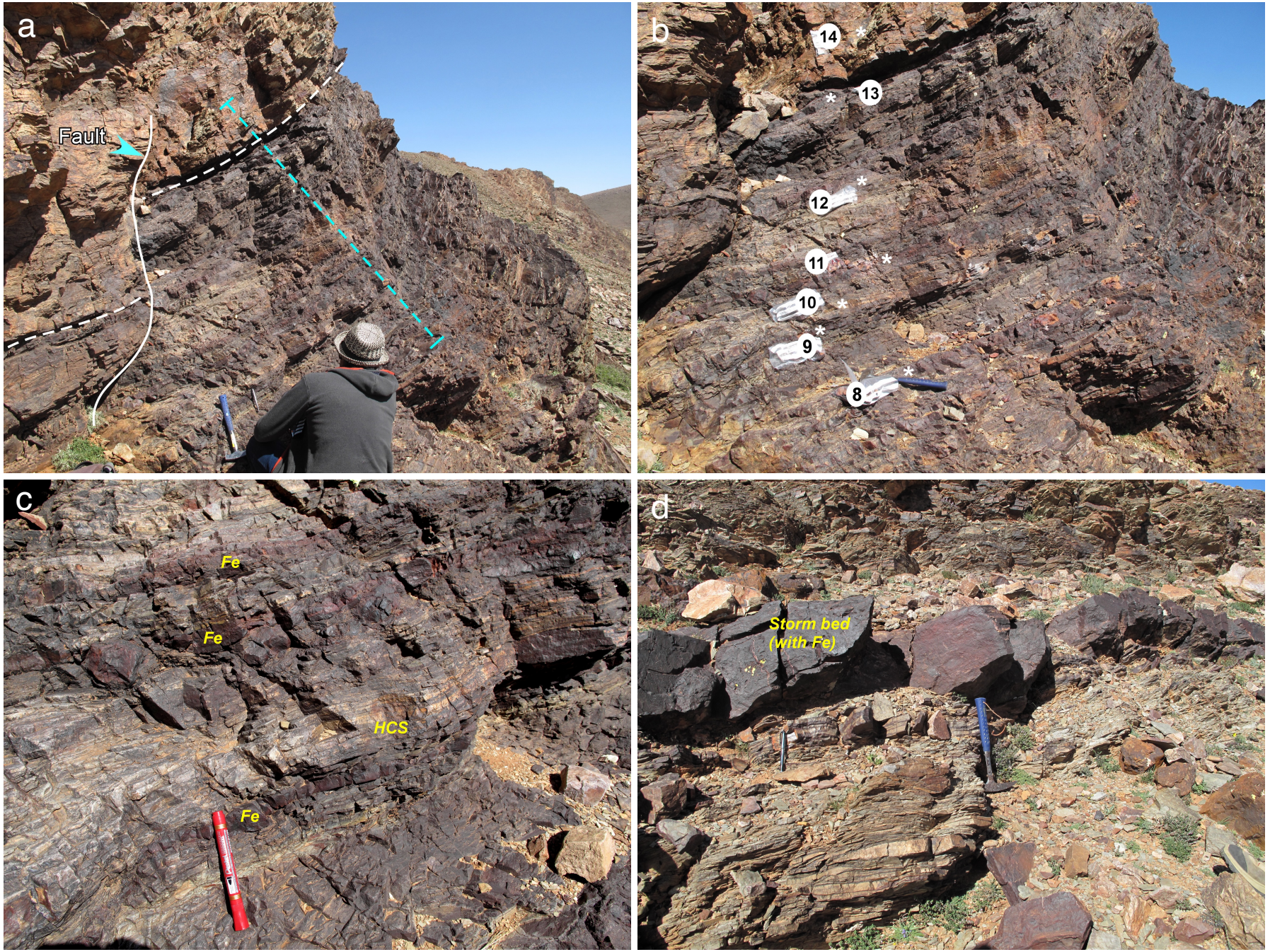
a
Fault
b
14
13
12
11
10
9
8
c
Fe
Fe
HCS
Fe
d
Storm bed
(with Fe)

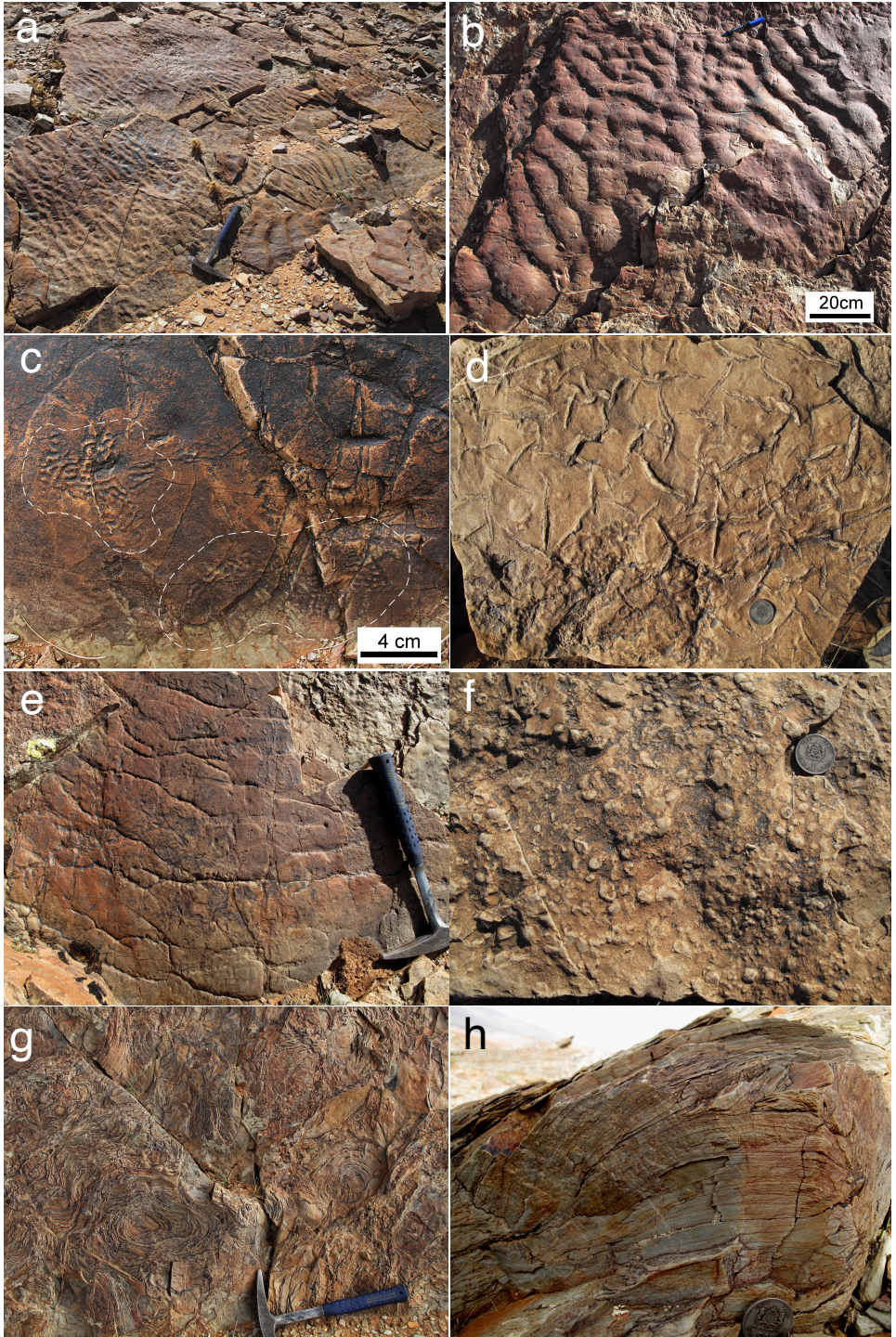
a
b
20cm
c
4 cm
d
e
f
g
h

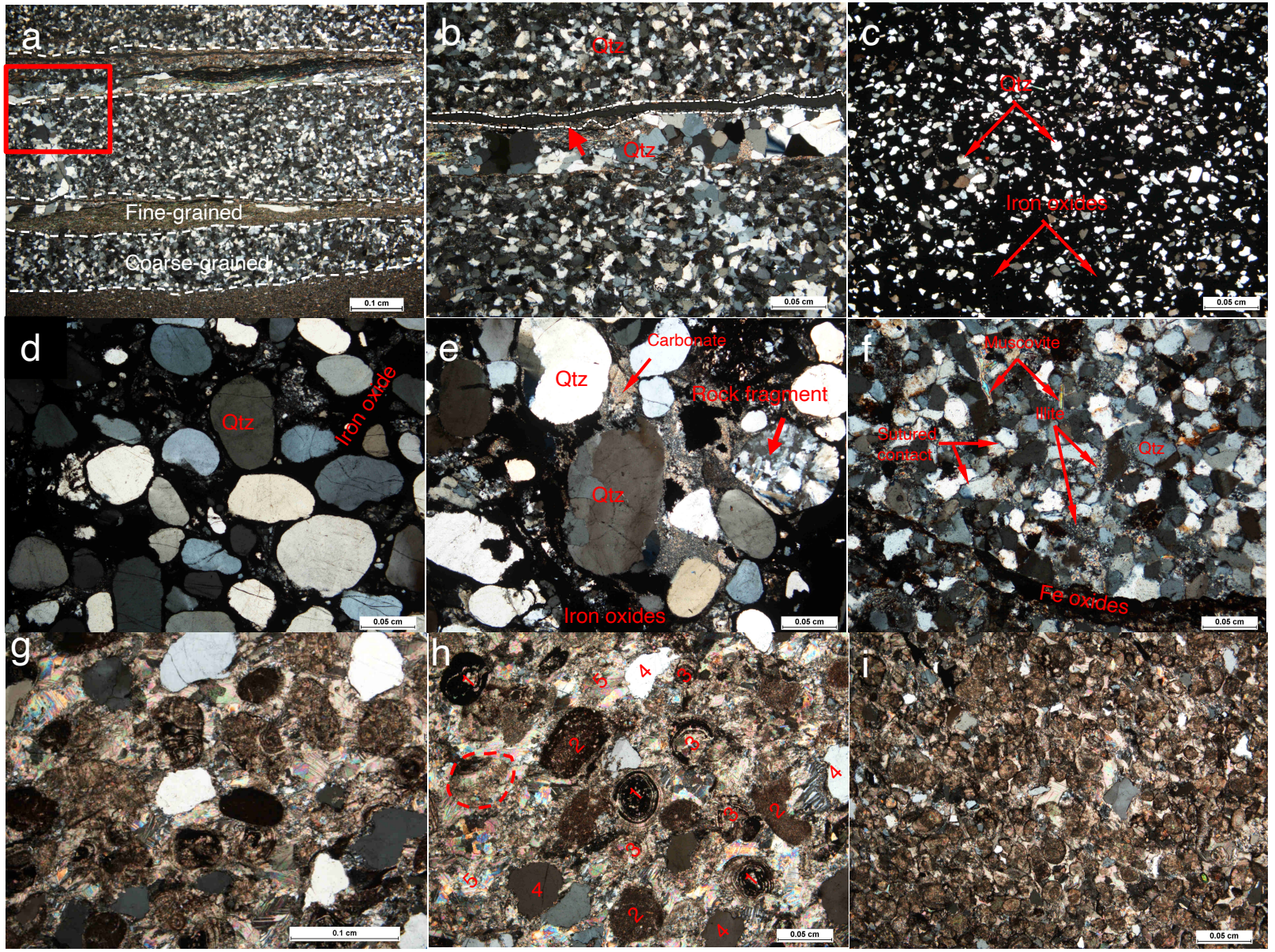
a
Fine-grained
Coarse-grained
0.1 cm
b
Qtz
Qtz
0.05 cm
c
Qtz
Iron oxides
0.05 cm
d
Qtz
Iron oxide
0.05 cm
e
Carbonate
Qtz
Rock fragment
Qtz
Iron oxides
0.05 cm
f
Muscovite
Illite
Sutured contact
Qtz
Fe oxides
0.05 cm
g
0.1 cm
h
0.05 cm
i
0.05 cm

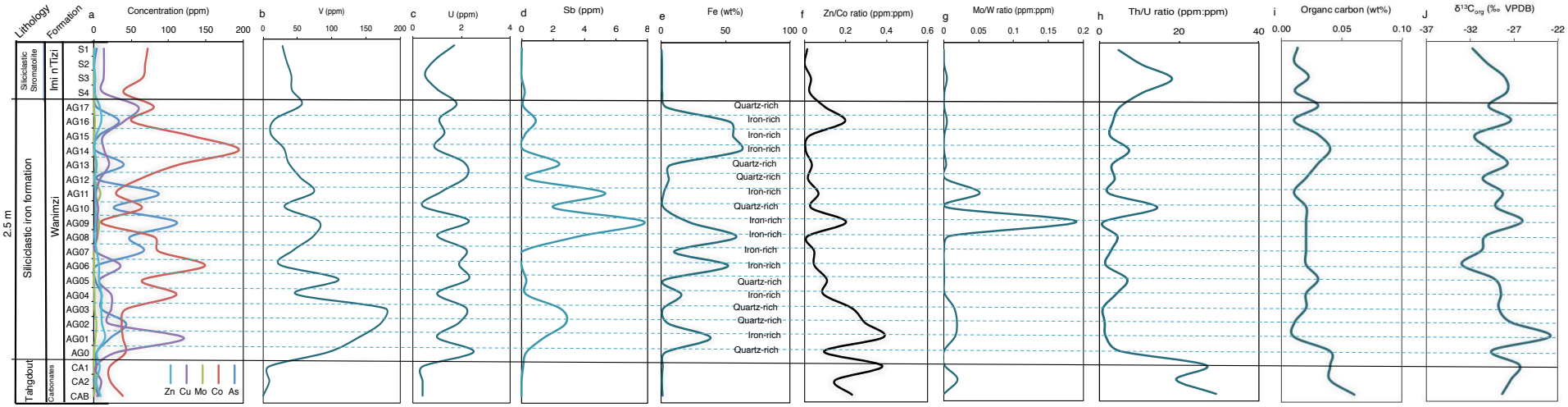
Lithology
Formation
a
Concentration (ppm)
0
50
100
150
200
b
V (ppm)
c
U (ppm)
2
4
d
Sb (ppm)
6
8
e
Fe (wt%)
f
Zn/Co ratio (ppm:ppm)
0.2
0.4
0.6
g
Mo/W ratio (ppm:ppm)
0.05
0.1
0.15
h
Th/U ratio (ppm:ppm)
20
40
i
Organc carbon (wt%)
0.00
0.05
0.10
J
δ13Corg (‰ VPDB)
-37
-32
-27
-22
Siliciclastic Stromatolite
Imi n'Tizi
S1
S2
S3
S4
2.5 m
Siliciclastic iron formation
Wanimzi
AG17
AG16
AG15
AG14
AG13
AG12
AG11
AG10
AG09
AG08
AG07
AG06
AG05
AG04
AG03
AG02
AG01
AG0
Quartz-rich
Iron-rich
Iron-rich
Iron-rich
Quartz-rich
Quartz-rich
Iron-rich
Quartz-rich
Iron-rich
Iron-rich
Iron-rich
Iron-rich
Quartz-rich
Iron-rich
Quartz-rich
Quartz-rich
Iron-rich
Quartz-rich
Tahgdout
Carbonates
CA1
CA2
CAB
Zn
Cu
Mo
Co
As

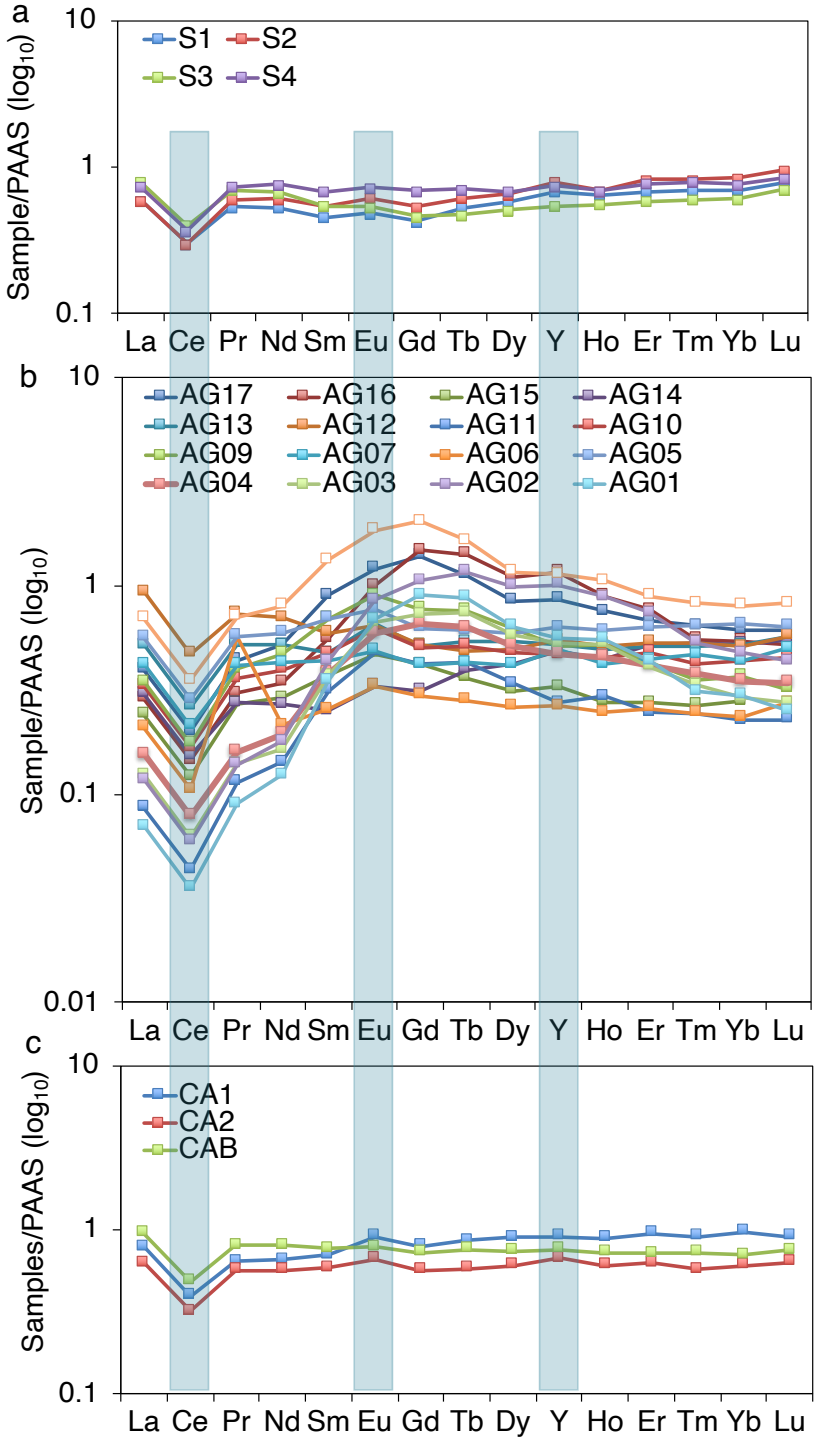
a
Sample/PAAS (log10)
10
1
0.1
S1
S2
S3
S4
La Ce Pr Nd Sm Eu Gd Tb Dy Y Ho Er Tm Yb Lu
b
Sample/PAAS (log10)
10
1
0.1
0.01
AG17
AG16
AG15
AG14
AG13
AG12
AG11
AG10
AG09
AG07
AG06
AG05
AG04
AG03
AG02
AG01
La Ce Pr Nd Sm Eu Gd Tb Dy Y Ho Er Tm Yb Lu
c
Samples/PAAS (log10)
10
1
0.1
CA1
CA2
CAB
La Ce Pr Nd Sm Eu Gd Tb Dy Y Ho Er Tm Yb Lu

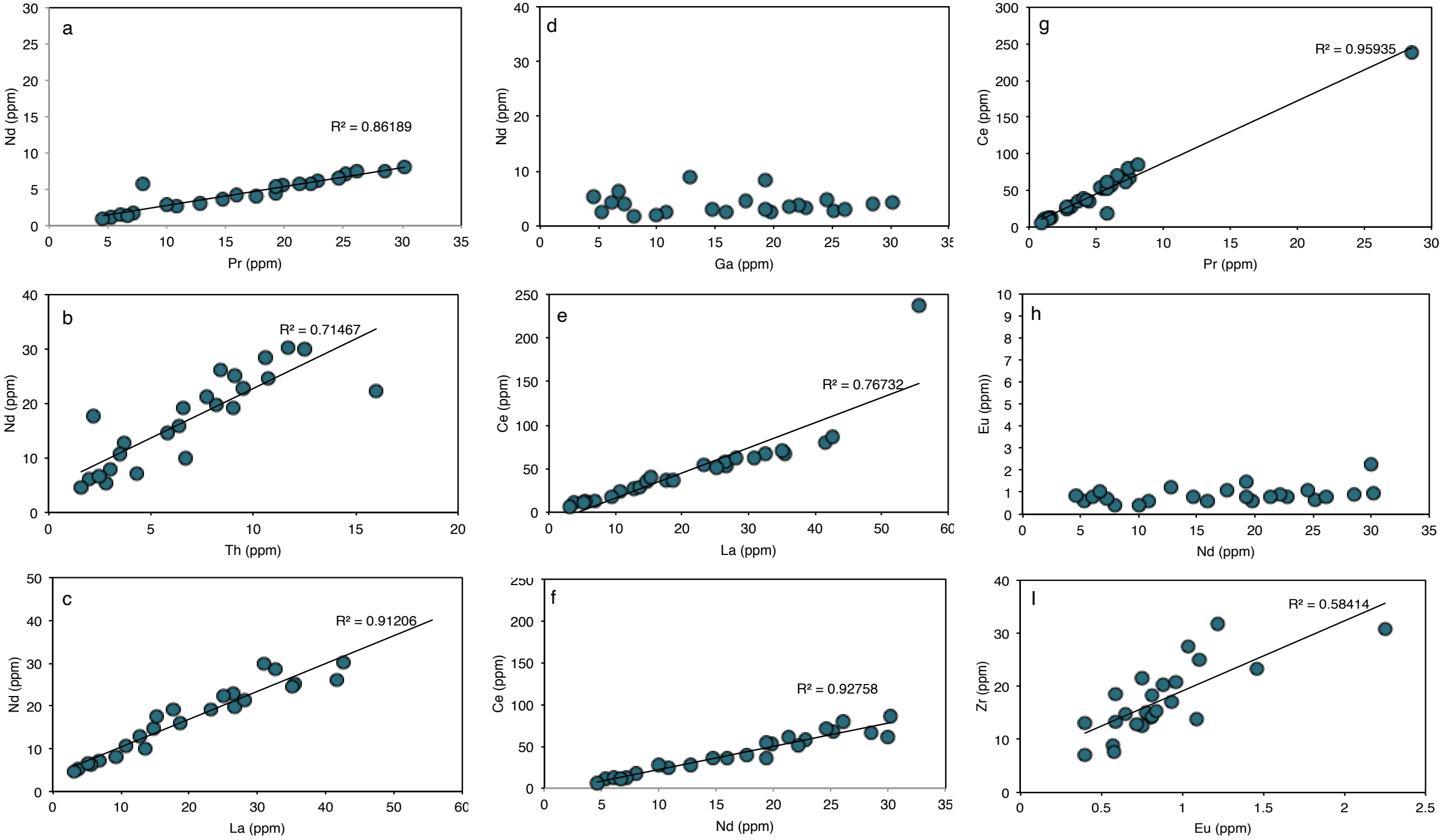
a
Nd (ppm)
Pr (ppm)
R² = 0.86189
b
Nd (ppm)
Th (ppm)
R² = 0.71467
c
Nd (ppm)
La (ppm)
R² = 0.91206
d
Nd (ppm)
Ga (ppm)
e
Ce (ppm)
La (ppm)
R² = 0.76732
f
Ce (ppm)
Nd (ppm)
R² = 0.92758
g
Ce (ppm)
Pr (ppm)
R² = 0.95935
h
Eu (ppm))
Nd (ppm)
l
Zr (ppm)
Eu (ppm)
R² = 0.58414

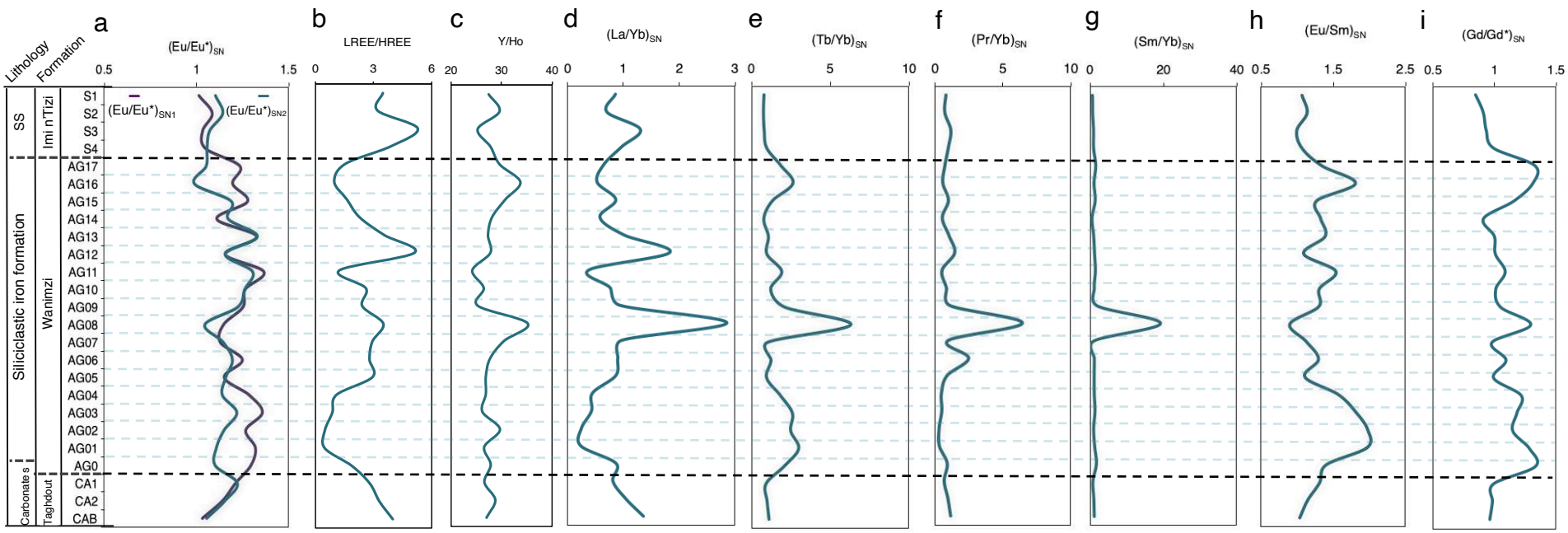
Lithology
Formation
a
(Eu/Eu*)SN
0.5
1
1.5
b
LREE/HREE
0
3
6
c
Y/Ho
20
30
40
d
(La/Yb)SN
0
1
2
3
e
(Tb/Yb)SN
0
5
10
f
(Pr/Yb)SN
0
5
10
g
(Sm/Yb)SN
0
20
40
h
(Eu/Sm)SN
0.5
1.5
2.5
i
(Gd/Gd*)SN
0.5
1
1.5
SS
Siliciclastic iron formation
Carbonate s
Imi n'Tizi
Wanimzi
Taghdout
S1
S2
S3
S4
AG17
AG16
AG15
AG14
AG13
AG12
AG11
AG10
AG09
AG08
AG07
AG06
AG05
AG04
AG03
AG02
AG01
AG0
CA1
CA2
CAB
(Eu/Eu*)SN1
(Eu/Eu*)SN2

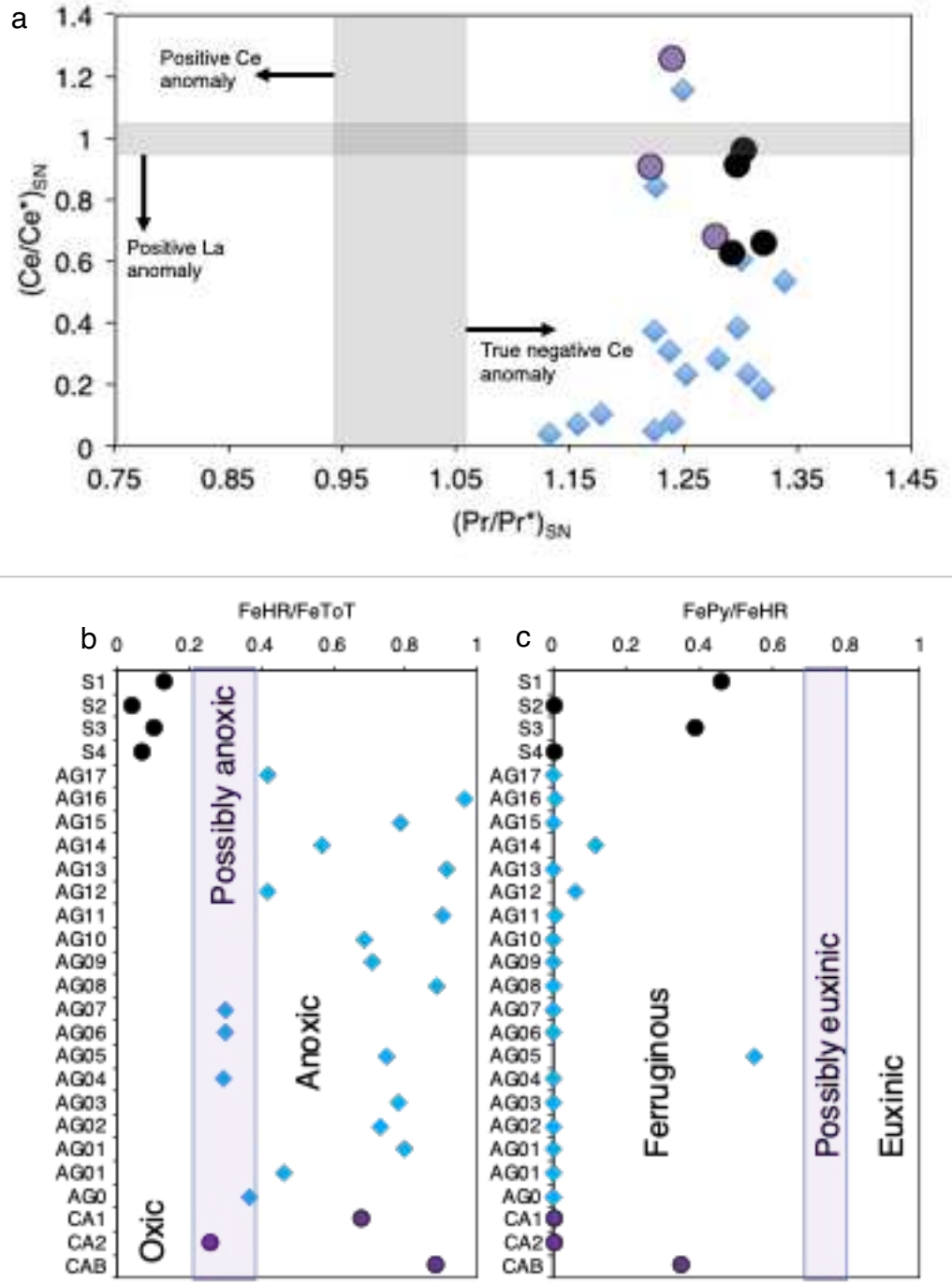
a
Positive Ce anomaly
Positive La anomaly
True negative Ce anomaly
(Ce/Ce*)SN
(Pr/Pr*)SN
1.4
1.2
1
0.8
0.6
0.4
0.2
0
0.75
0.85
0.95
1.05
1.15
1.25
1.35
1.45
b
FeHR/FeToT
0
0.2
0.4
0.6
0.8
1
Oxic
Possibly anoxic
Anoxic
c
FePy/FeHR
Ferruginous
Possibly euxinic
Euxinic
S1
S2
S3
S4
AG17
AG16
AG15
AG14
AG13
AG12
AG11
AG10
AG09
AG08
AG07
AG06
AG05
AG04
AG03
AG02
AG01
AG01
AG0
CA1
CA2
CAB

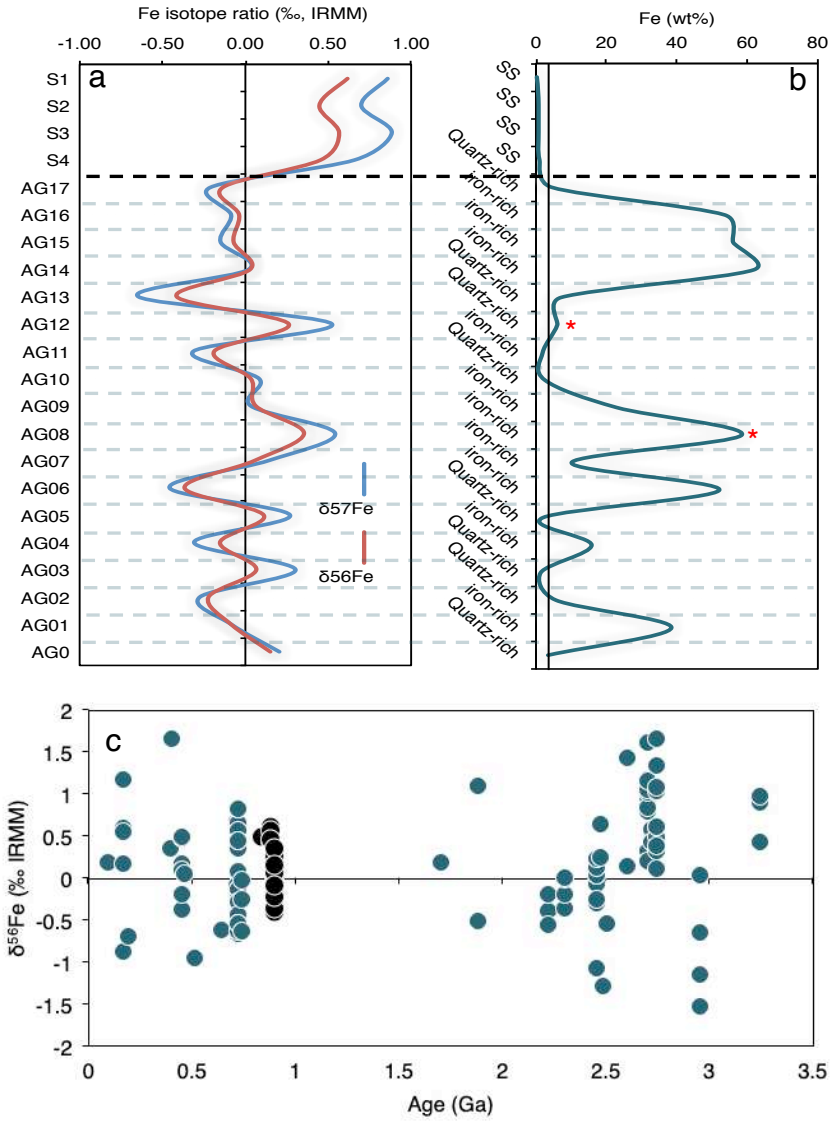
Fe isotope ratio (‰, IRMM)
-1.00
-0.50
0.00
0.50
1.00
a
S1
S2
S3
S4
AG17
AG16
AG15
AG14
AG13
AG12
AG11
AG10
AG09
AG08
AG07
AG06
AG05
AG04
AG03
AG02
AG01
AG0
δ57Fe
δ56Fe
Fe (wt%)
0
20
40
60
80
b
SS
SS
SS
SS
Quartz-rich
Iron-rich
Iron-rich
Iron-rich
Quartz-rich
Quartz-rich
Iron-rich
Quartz-rich
Iron-rich
Iron-rich
Iron-rich
Iron-rich
Quartz-rich
Iron-rich
Quartz-rich
Quartz-rich
Iron-rich
Quartz-rich
c
δ56Fe (‰ IRMM)
2
1.5
1
0.5
0
-0.5
-1
-1.5
-2
0
0.5
1
1.5
2
2.5
3
3.5
Age (Ga)

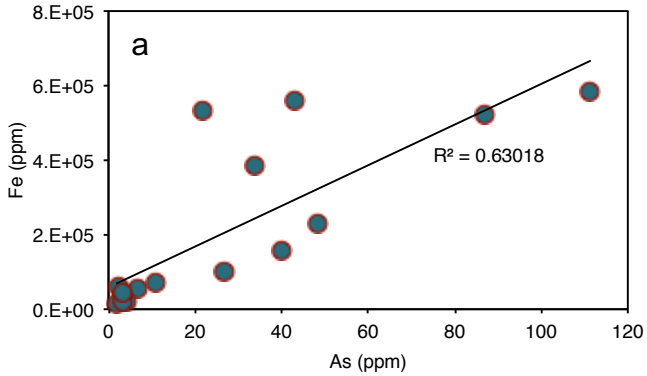
a
8.E+05
6.E+05
4.E+05
2.E+05
0.E+00
Fe (ppm)
R² = 0.63018
0
20
40
60
80
100
120
As (ppm)

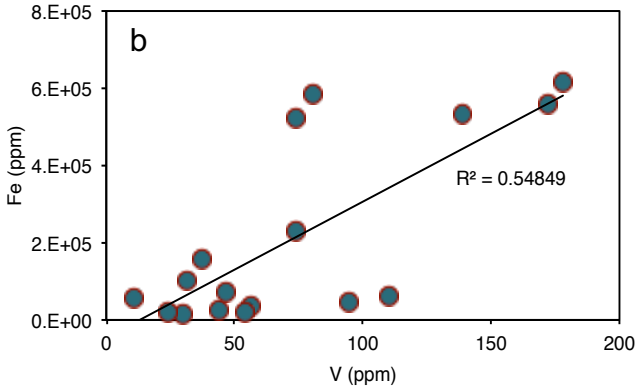
b
8.E+05
6.E+05
4.E+05
2.E+05
0.E+00
Fe (ppm)
R² = 0.54849
0
50
100
150
200
V (ppm)

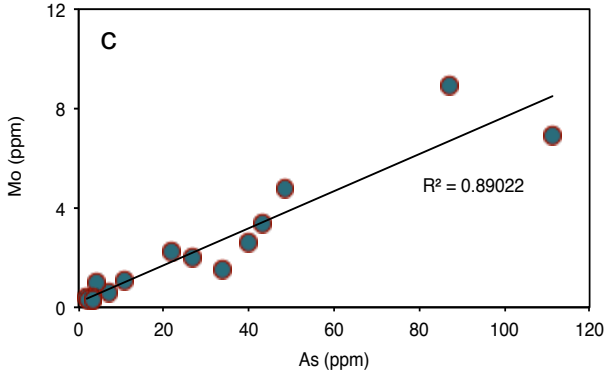
c
12
8
4
0
Mo (ppm)
R² = 0.89022
0
20
40
60
80
100
120
As (ppm)

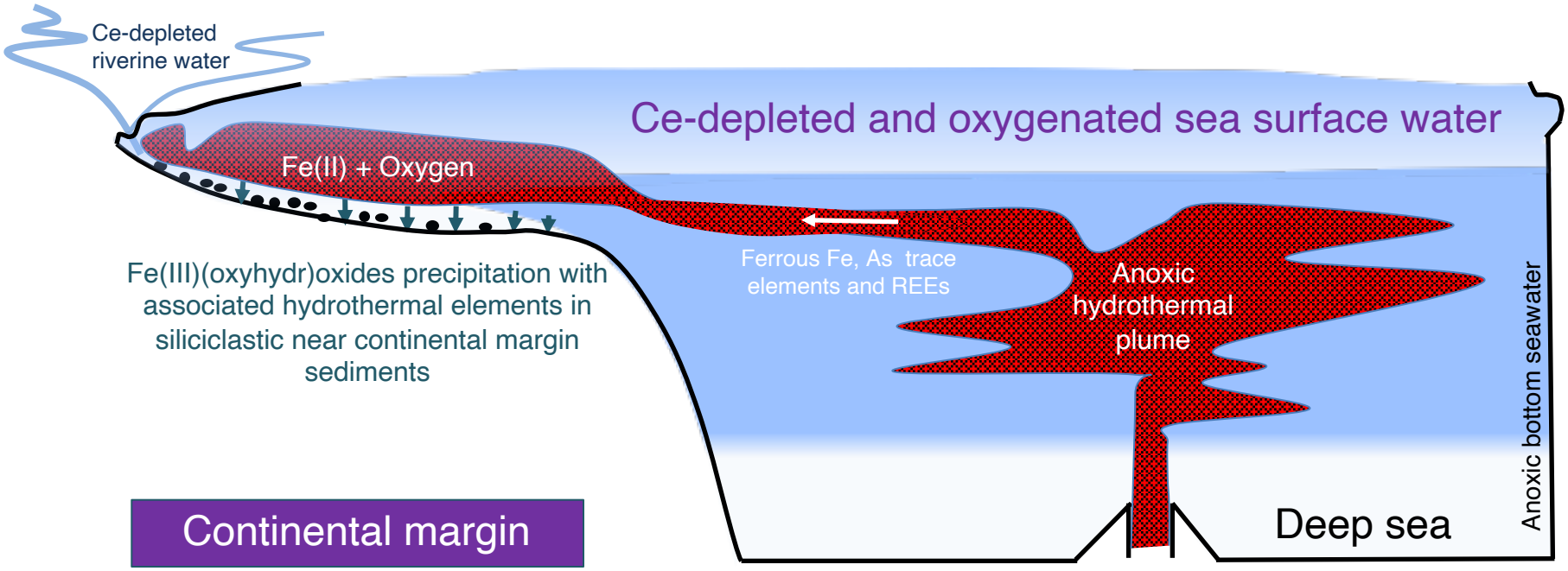
Ce-depleted
riverine water
Ce-depleted and oxygenated sea surface water
Fe(II) + Oxygen
Fe(III)(oxyhydr)oxides precipitation with associated hydrothermal elements in siliciclastic near continental margin sediments
Ferrous Fe, As trace elements and REEs
Anoxic hydrothermal plume
Anoxic bottom seawater
Deep sea
Continental margin

Appendix

Early Neoproterozoic oxygenation dynamics along the northern margin of the West African Craton, Anti-Atlas Mountains, Morocco

Ernest Chi Fru[a*], Olabode Bankole[b], Ibtissam Chraiki[c], Nassrddine Youbi[c], Marc-Alban Millet[a], Olivier Rouxel[d], Abderrazzak El Albani[b], El Hafid Bouougri [c]

[a]School of Earth and Ocean Sciences, Centre for Geobiology and Geochemistry, Cardiff University, Cardiff CF10 3AT, Wales, UK

[b]University of Poitiers, CNRS IC2MP UMR 7285, Poitiers, France.

[c]DLGR, Department of Geology, Faculty of Sciences-Semlalia, Cadi Ayyad University, Marrakesh, Morocco.

[d]Unité de Géosciences Marines, IFREMER, Z.I. Pointe du diable, BP 70, 29280 Plouzané, France.

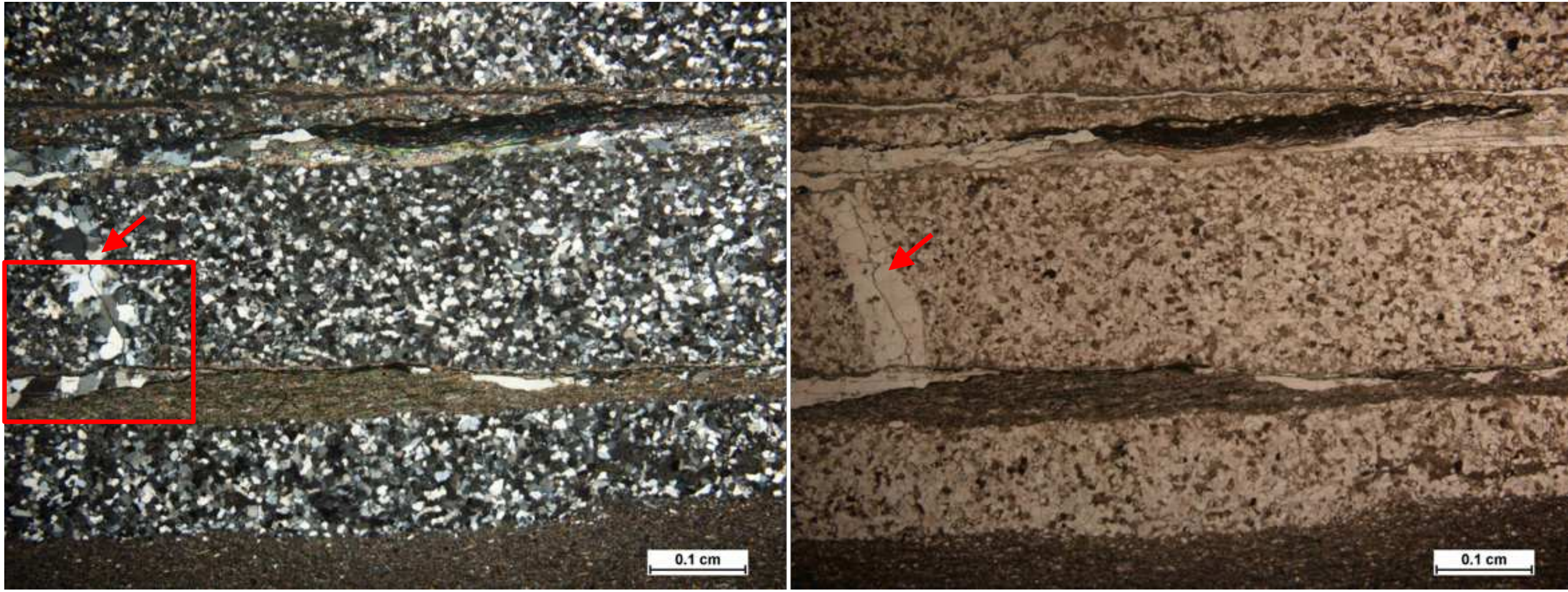

Appendix A. Microbially induced sedimentary structures of moderately compacted and well-sorted quartz-dominated silty-sandstone with alternating thin mud/shale laminae, consisting of micas (muscovite and illite). Thin sectioned cross polarized (a) and plain light (b) photographs showing the compositional layering of the flat top stromatolitic mats. The fluid nature of the fine-grained layer is suggested by leakages through cracks in the coarse-grained bed as indicated by the red arrows in panels a and b. The read box is enlarged in appendix B.

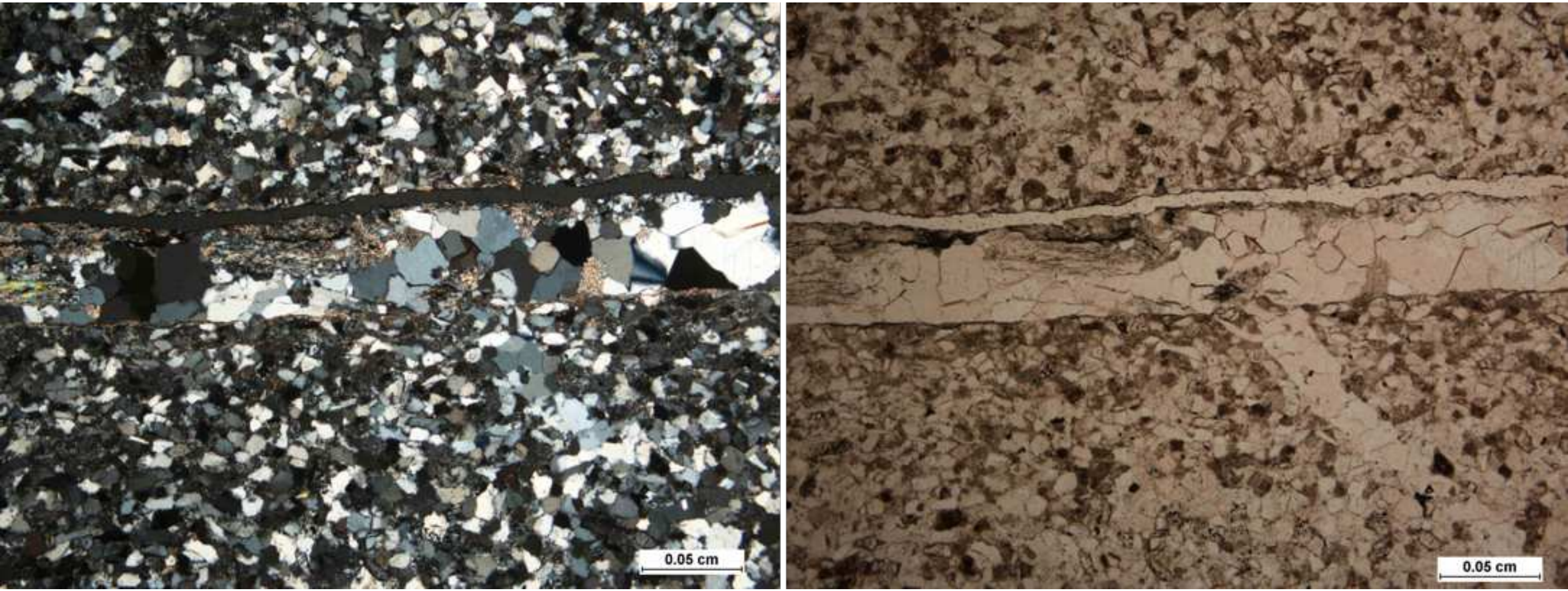

Appendix B. Enlarged red square in Appendix a, for thin sectioned cross polarized (a) and plain light (b) photographs showing the compositional layering of the flat top stromatolitic mats.

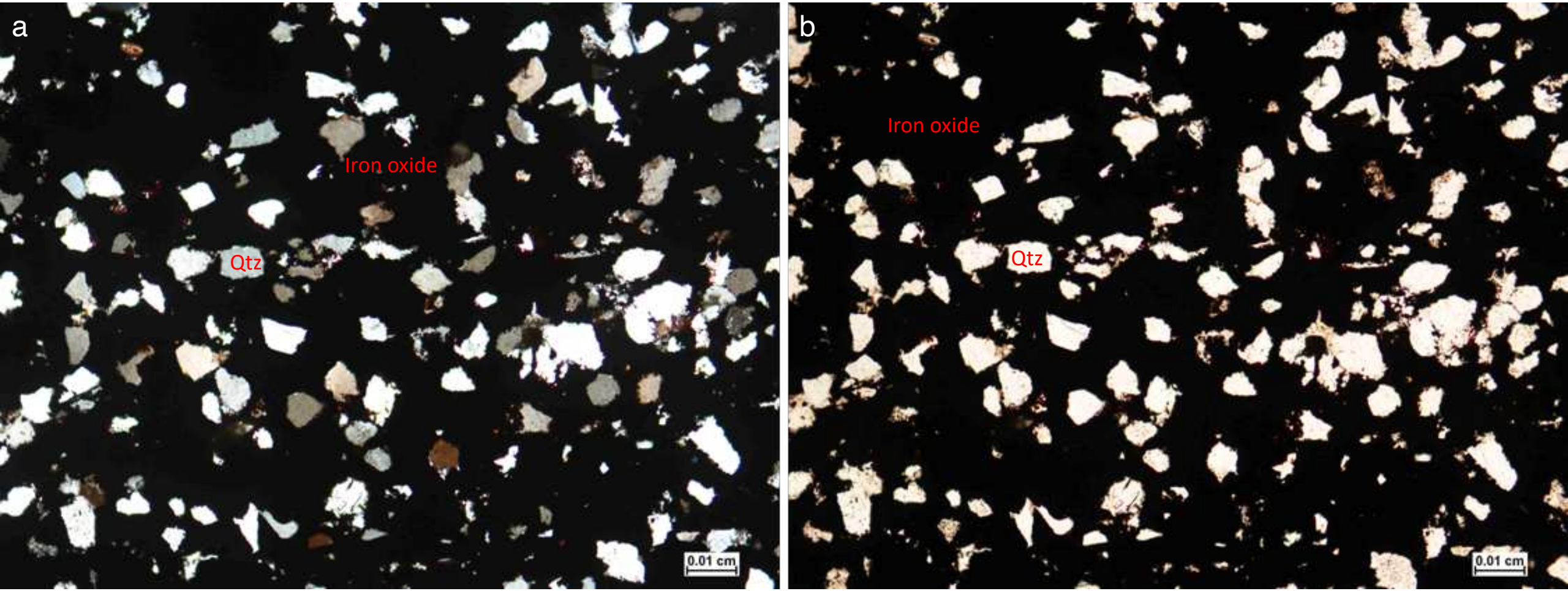

Appendix C. Thin sectioned cross polarized (a) and plain light (b) photographs for sample AG16 from the Wanimzi ironstone, showing well-sorted siltstones dominantly composed of sub-angular quartz clasts floating in an iron-oxide rich matrix (syn-depositional) in the Wanimzi Fe-rich deposit.

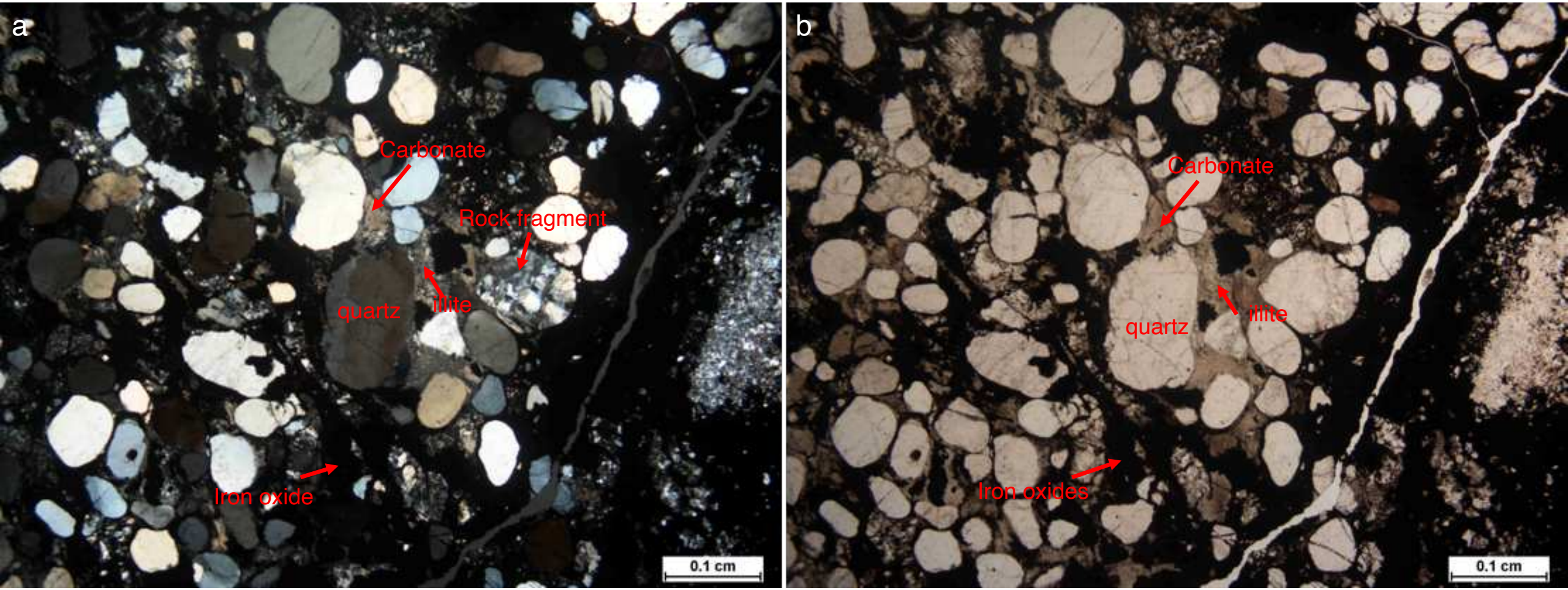

Appendix D. Thin sectioned cross polarized (a) and plain light (b) photographs for sample AG08 from the Wanimzi ironstone, showing poorly sorted coarse-grained sandstone consisting of rounded quartz grains surrounded by iron-oxide, illite, and carbonate cements

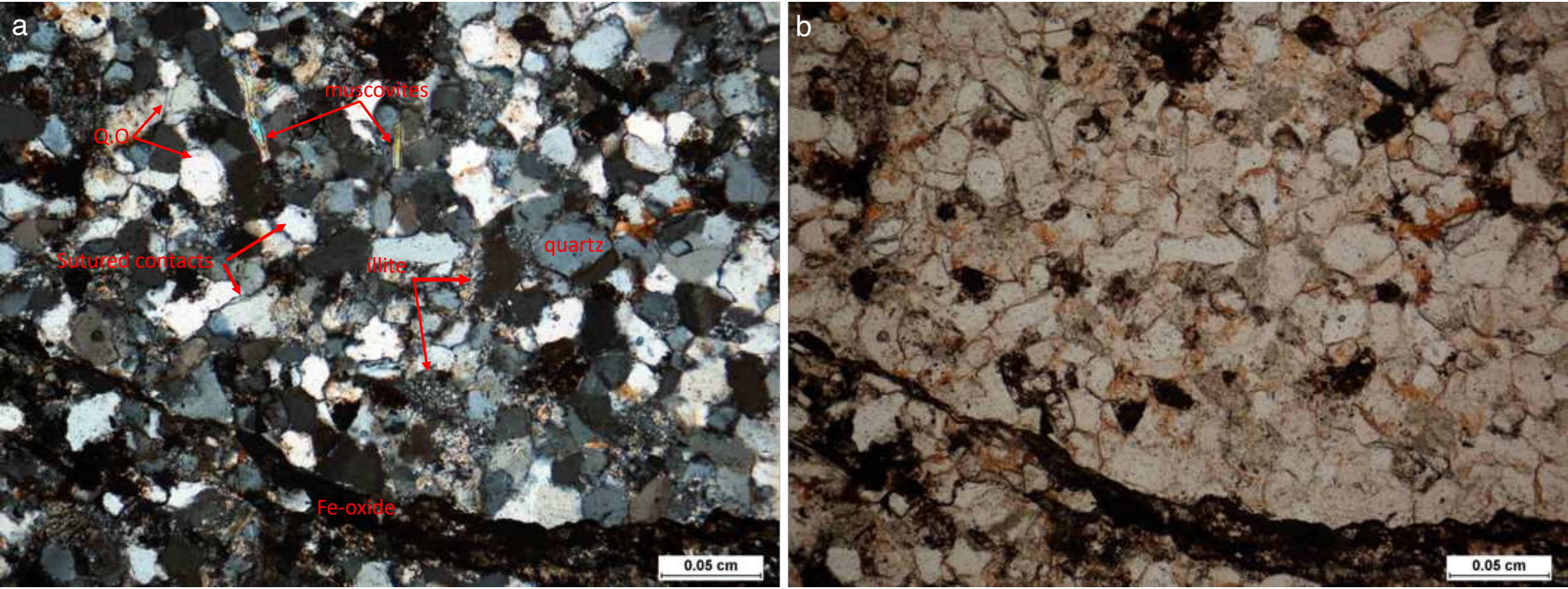

Appendix E. Moderately compacted silty sandstones dominated by moderately sorted angular to sub-angular detrital quartz grains (with sutured contacts) and mica flakes (mainly muscovites) in illite and iron-oxide cements for sample AG06 from the Wanimzi ironstone. Quartz overgrowths are observed in few instances . Thin sectioned cross polarized (a) and plain light (b) photographs, showing sutured clastic debris suggestive of Fe-rich cement . QO = quartz overgrowths

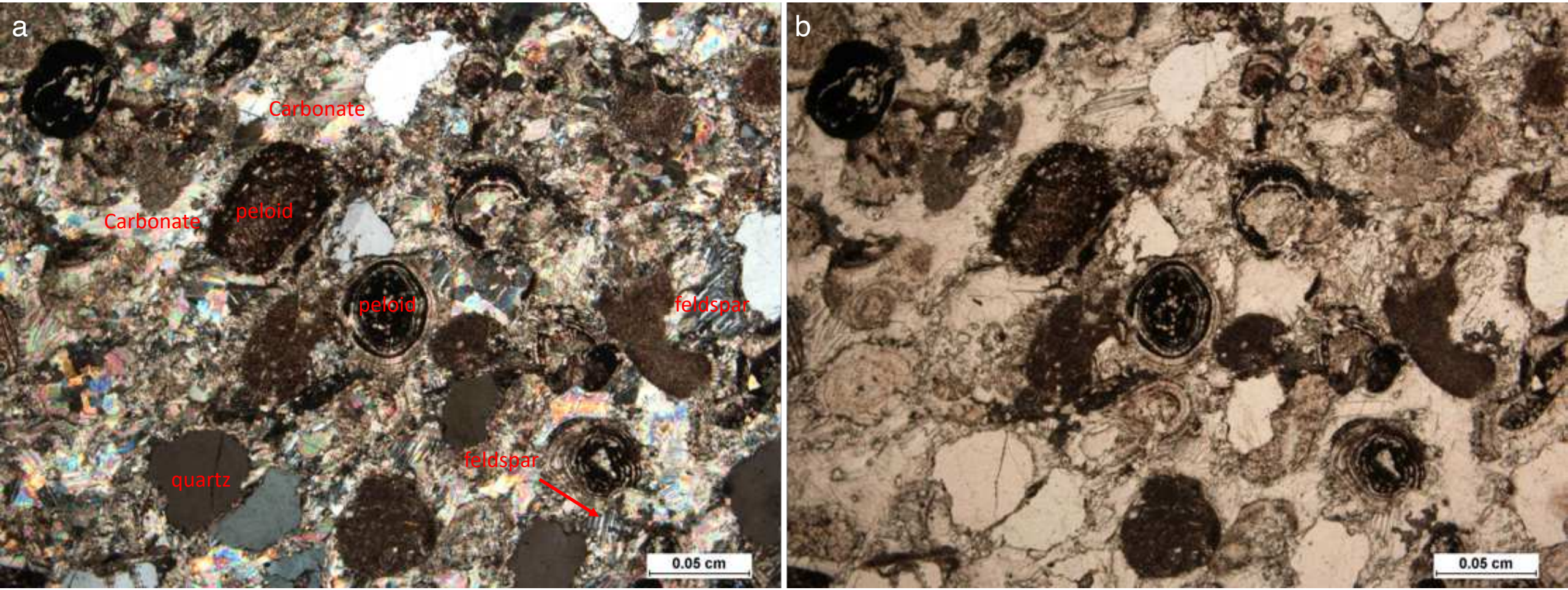

Appendix F. Thin sectioned cross polarized (a) and plain light (b) photographs for siliciclastic sample CA1 from the Tagdout Formation, showing rounded and ooidal clastic debris cemented in a carbonate-rich matrix. Peloids and microbially induced spherulite cemented in a calcite-rich matrix. Few quartz grains and altered feldspars are dispersed within the carbonate cement.

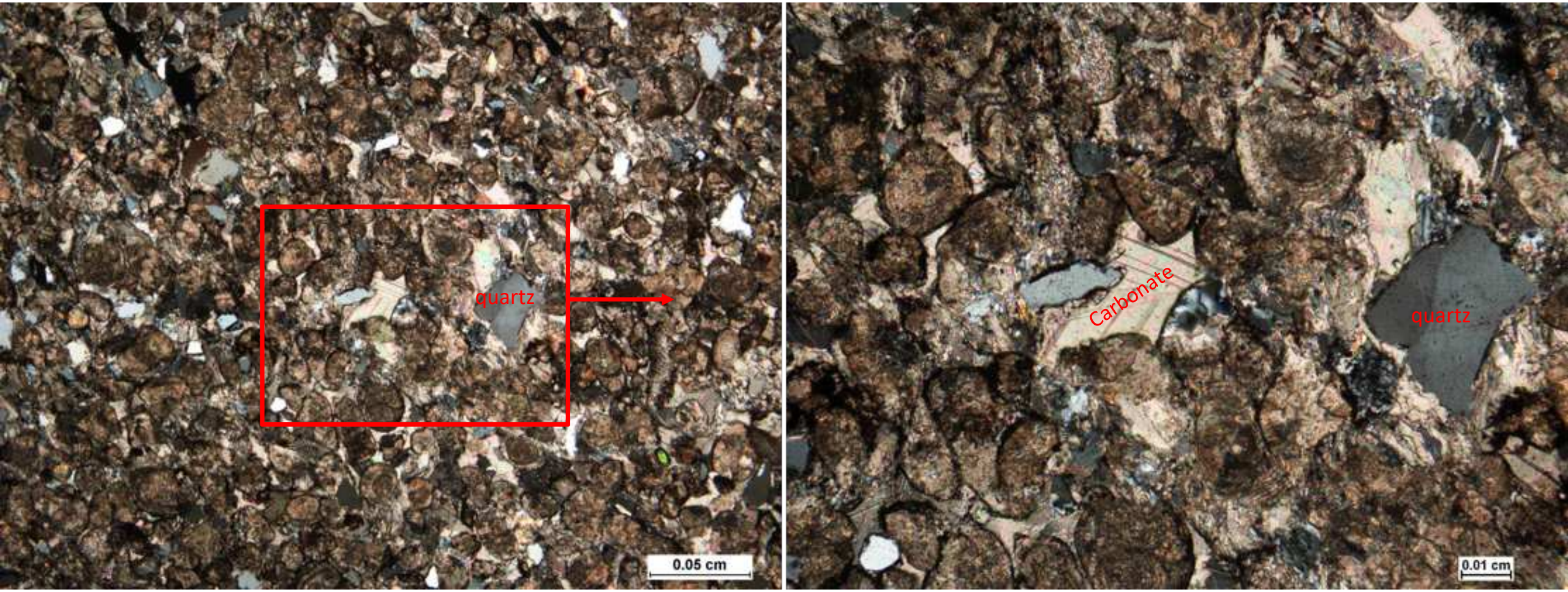

Appendix G. Thin sectioned cross polarized light (a) and plain light (b) photographs for siliciclastic carbonate sample CAB2 from the Taghdout Formation, showing peloidal clastic debris cemented in a carbonate-rich matrix

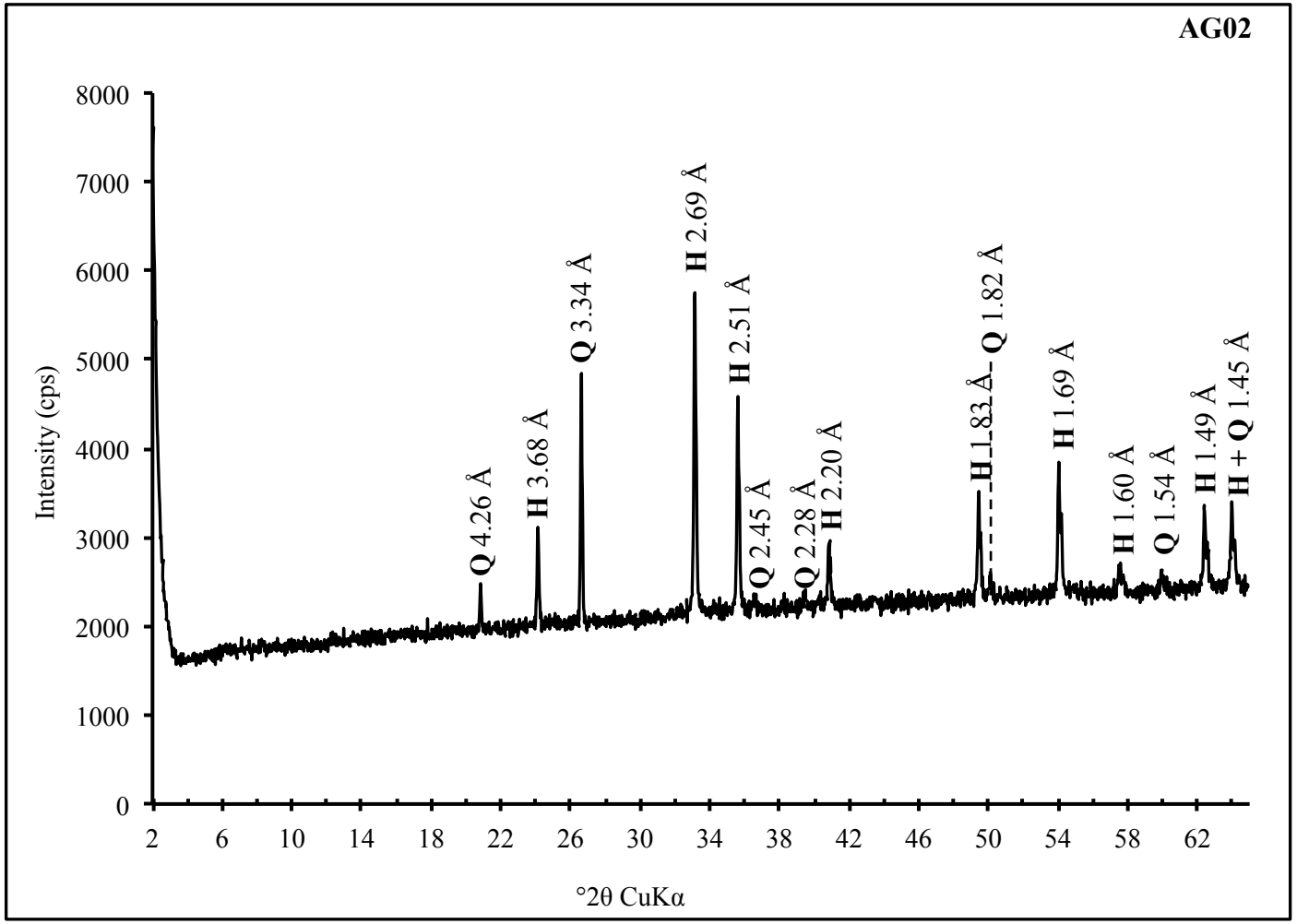

Keys:
Q = quartz
H = hematite

Appendix H. XRD mineralogical signal for sample AG02 from the Wanimzi ironstone

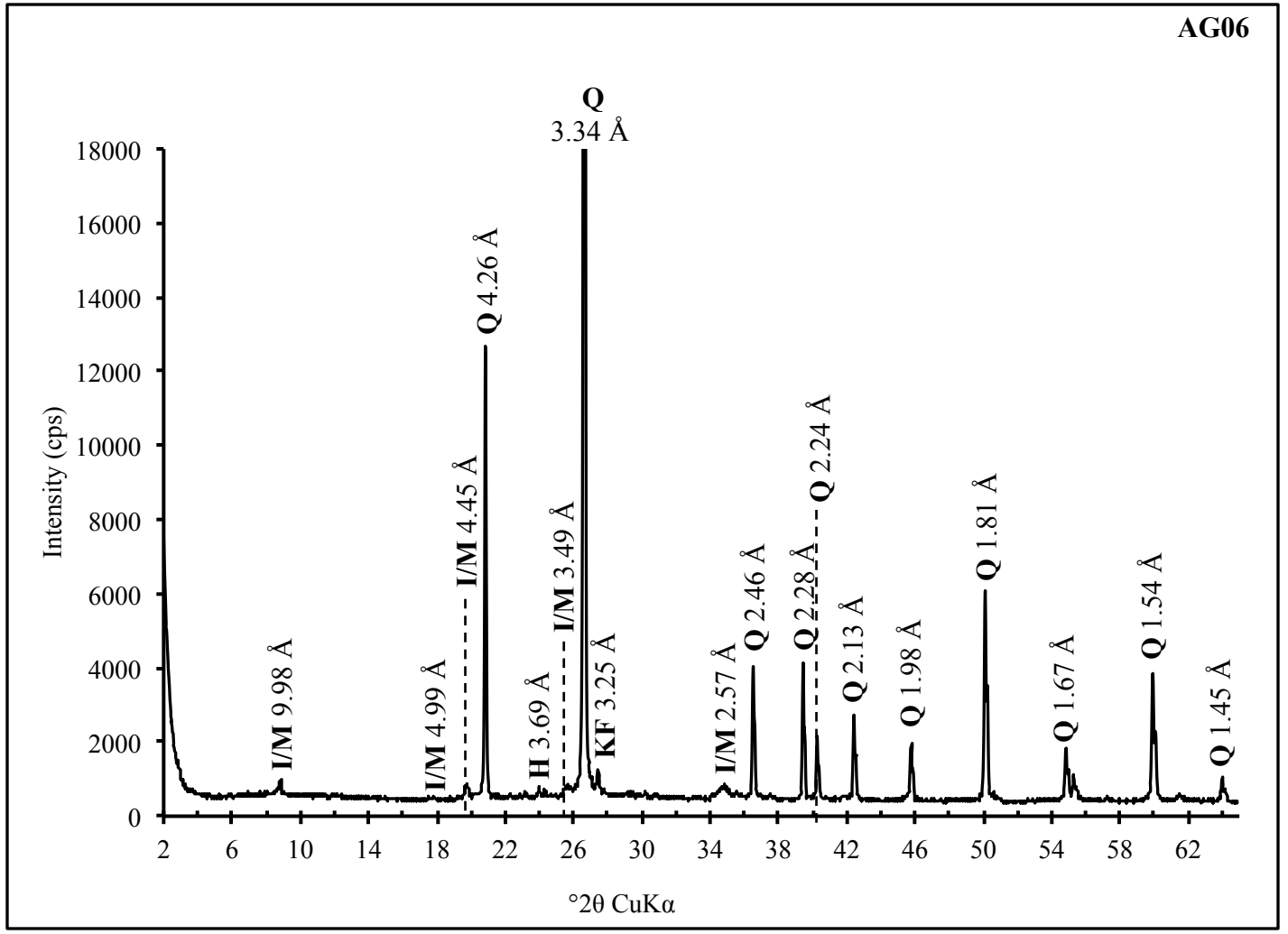

Keys:
Q = quartz
H = hematite
I/M = illite/mica
KF = K-feldspar

Appendix I. XRD mineralogical signal for sample AG06 from the Wanimzi ironstone

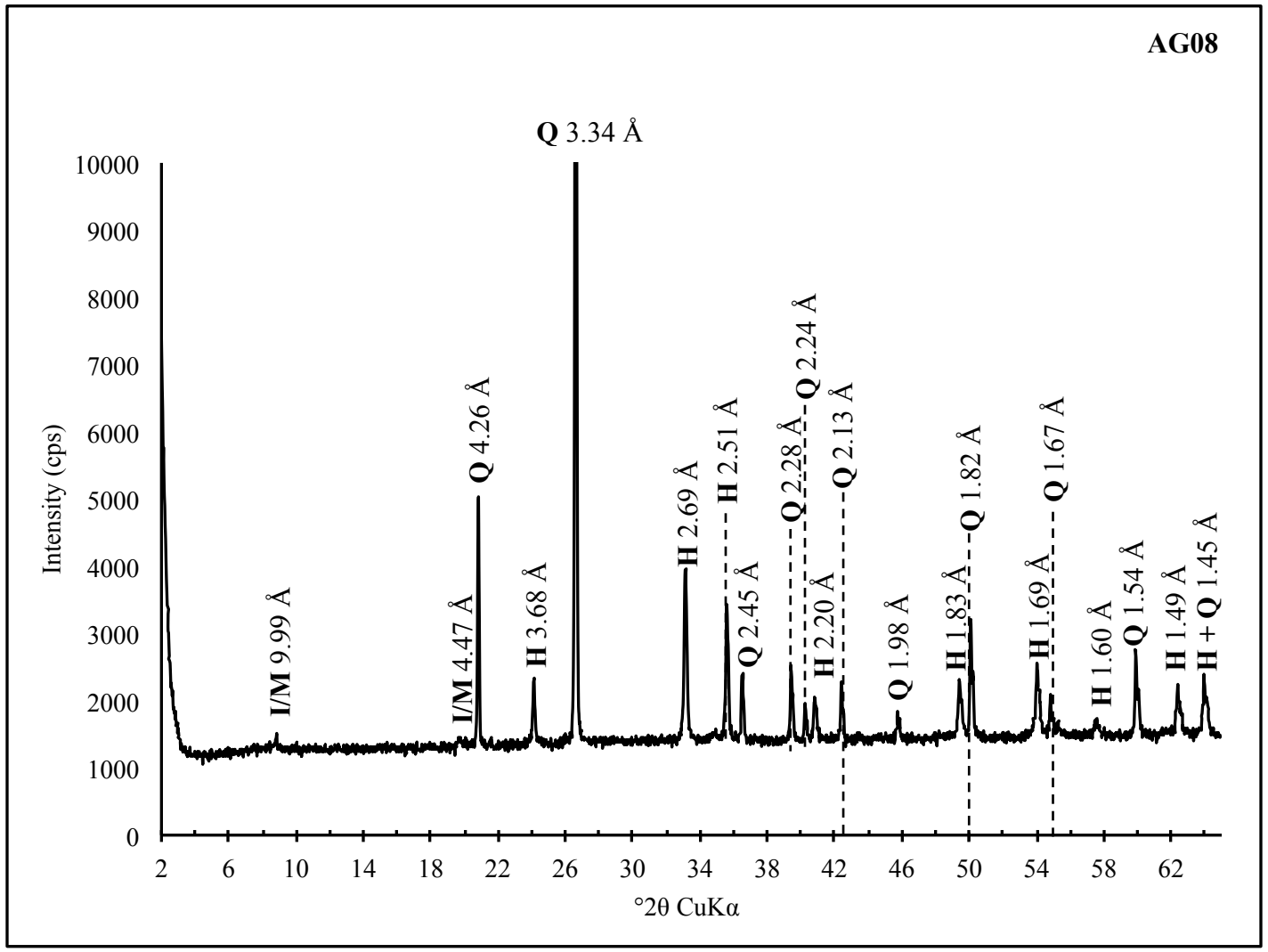

Keys:
Q = quartz
H = hematite
I/M = illite/mica

Appendix J. XRD mineralogical signal for sample AG08 from the Wanimzi ironstone

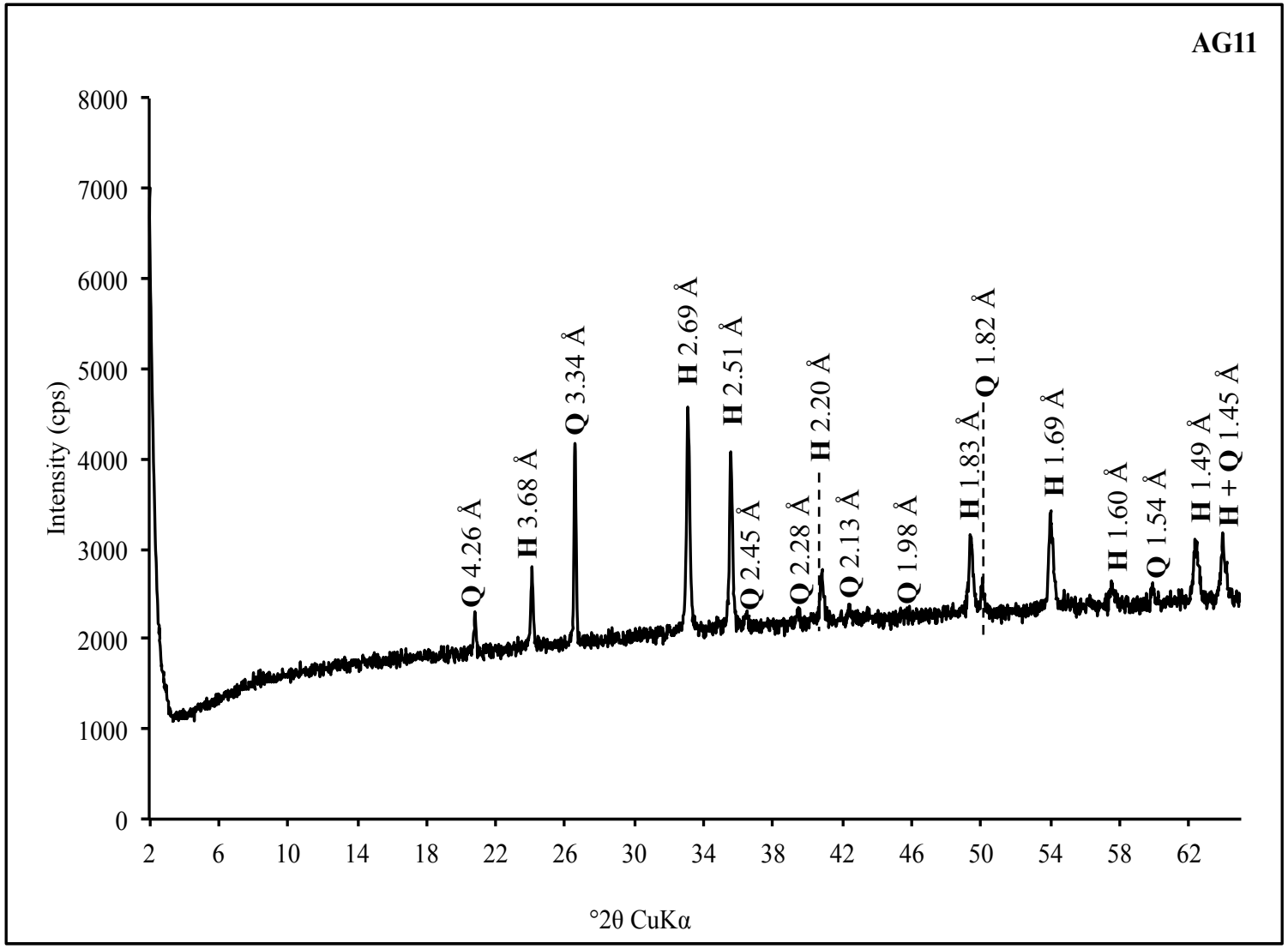

Keys:
Q = quartz
H = hematite

Appendix K. XRD mineralogical signal for sample AG11 from the Wanimzi ironstone

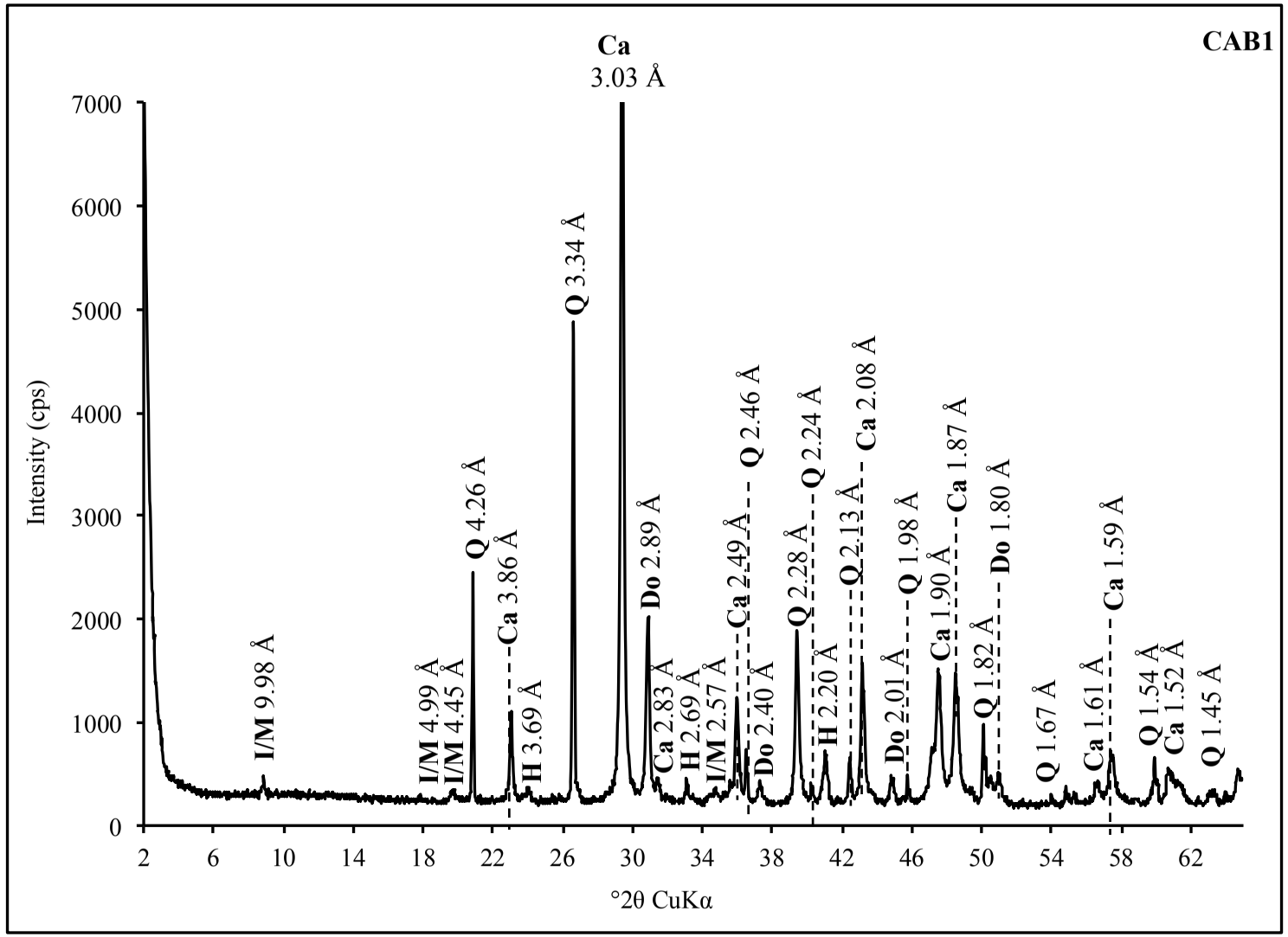

Keys:
Q = quartz
H = hematite
I/M = illite/mica
Ca = calcite
Do = dolomite

Appendix L. XRD mineralogical signal for sample CAB1 from the Taghdout siliclastic carbonates

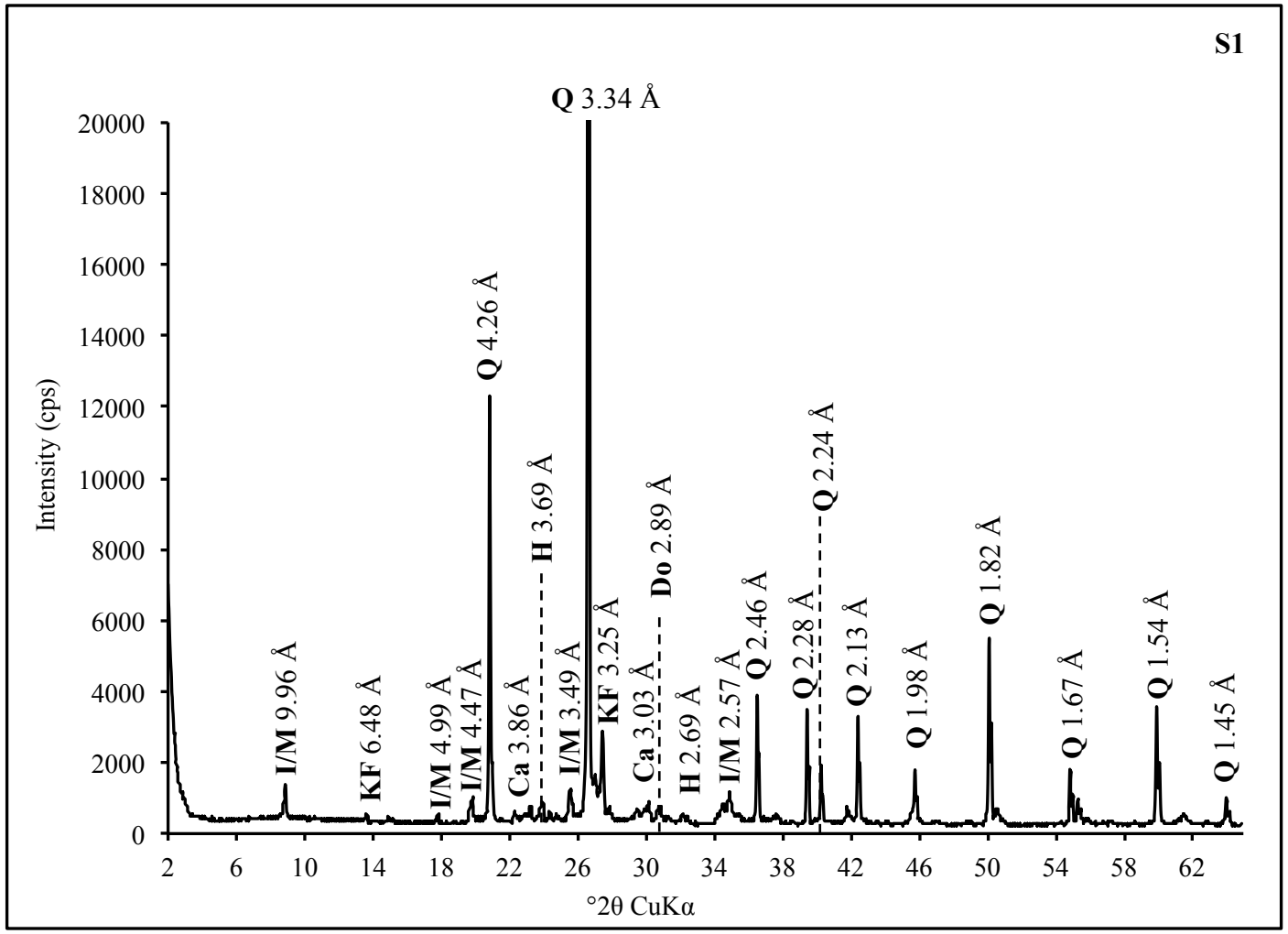

Keys:
Q = quartz
H = hematite
I/M = illite/mica
Ca = calcite
Do = dolomite
KF = K-feldspar

Appendix M. XRD mineralogical signal for sample S1 from the siliciclastic stromatolites

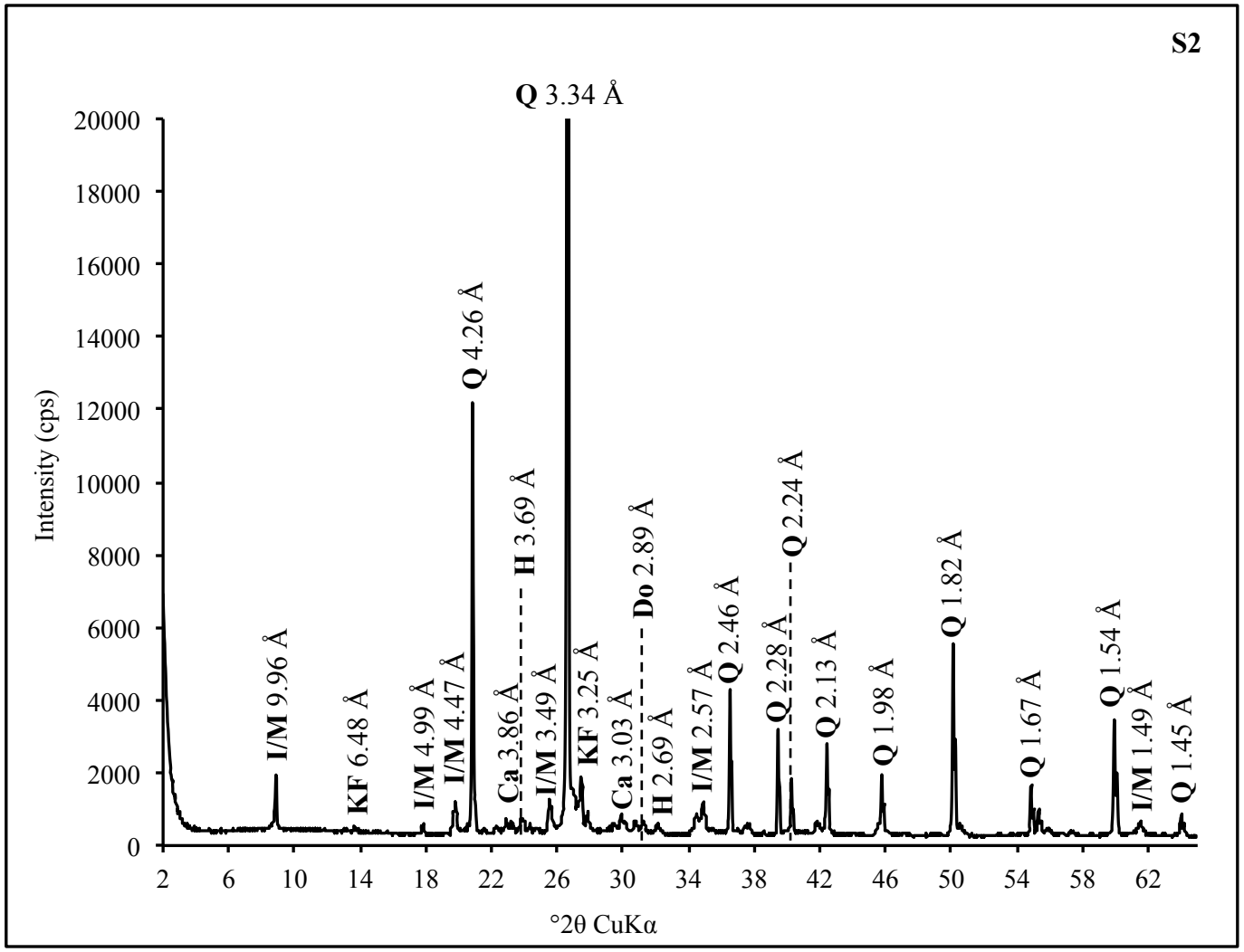

Keys:
Q = quartz
H = hematite
I/M = illite/mica
Ca = calcite
Do = dolomite
KF = K-feldspar

Appendix N. XRD mineralogical signal for sample S2 from the siliciclastic stromatolites

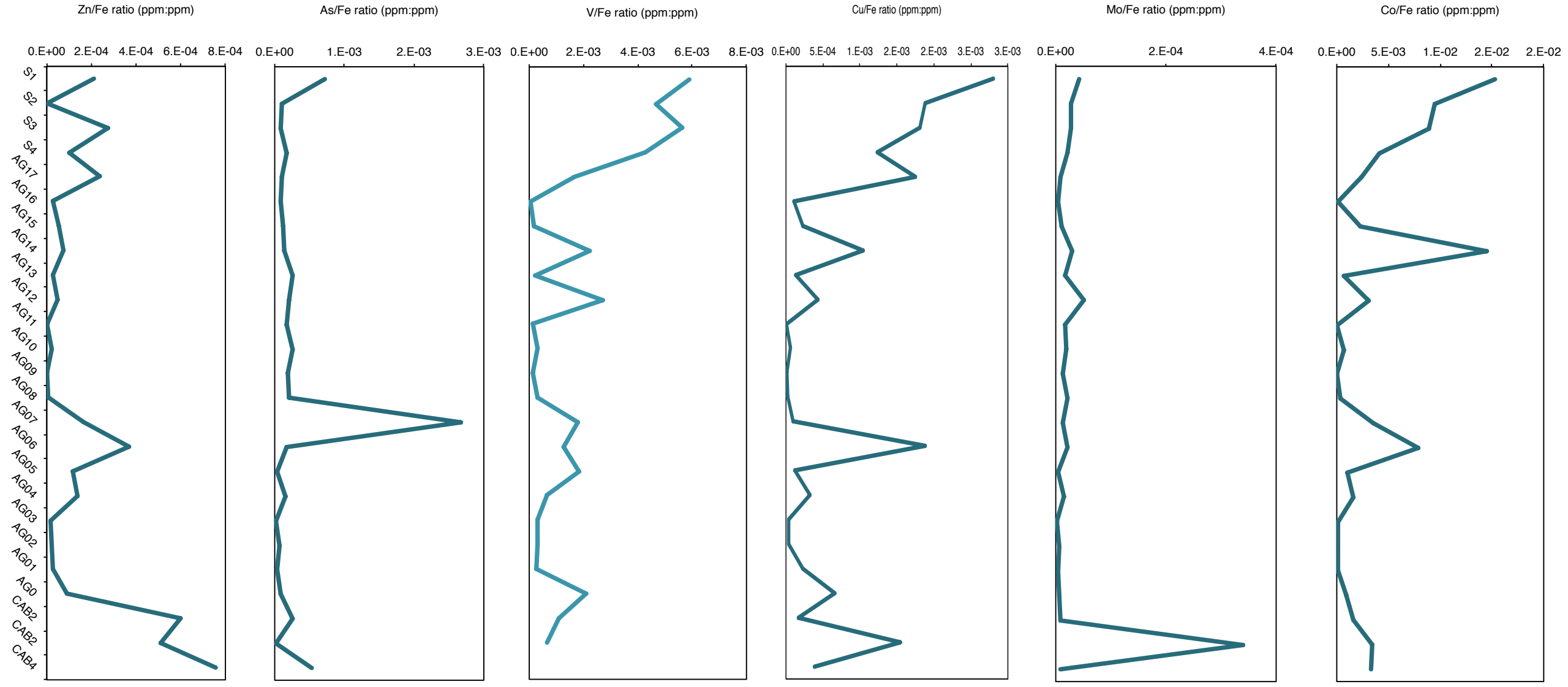

Appendix O. Concentrations of Zn, As, V, Cu, Mo and Cu normalized to Fe concentrations across the sampled succession

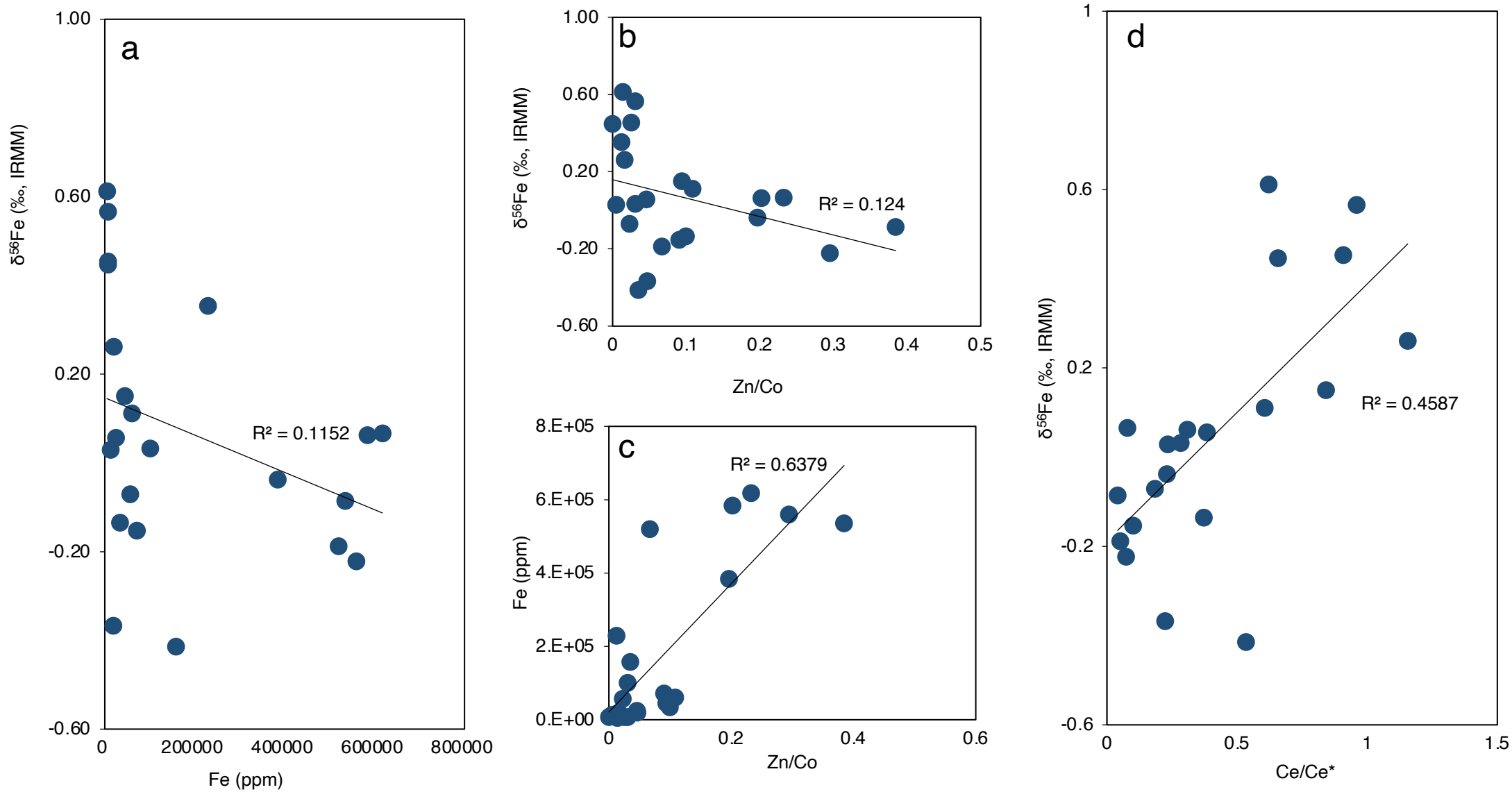

Appendix P. Cross plots between (a) Fe and δ^{56}Fe, (b) δ^{56}Fe and Zn/Co ratios, (c) Fe and Zn/Co and (d) δ^{56}Fe and Ce/Ce'